University of Rochester
Laboratory for Laser Energetics

DOE/SF/19460-468
January 2003

LLE 2002 Annual Report

October 2001 – September 2002

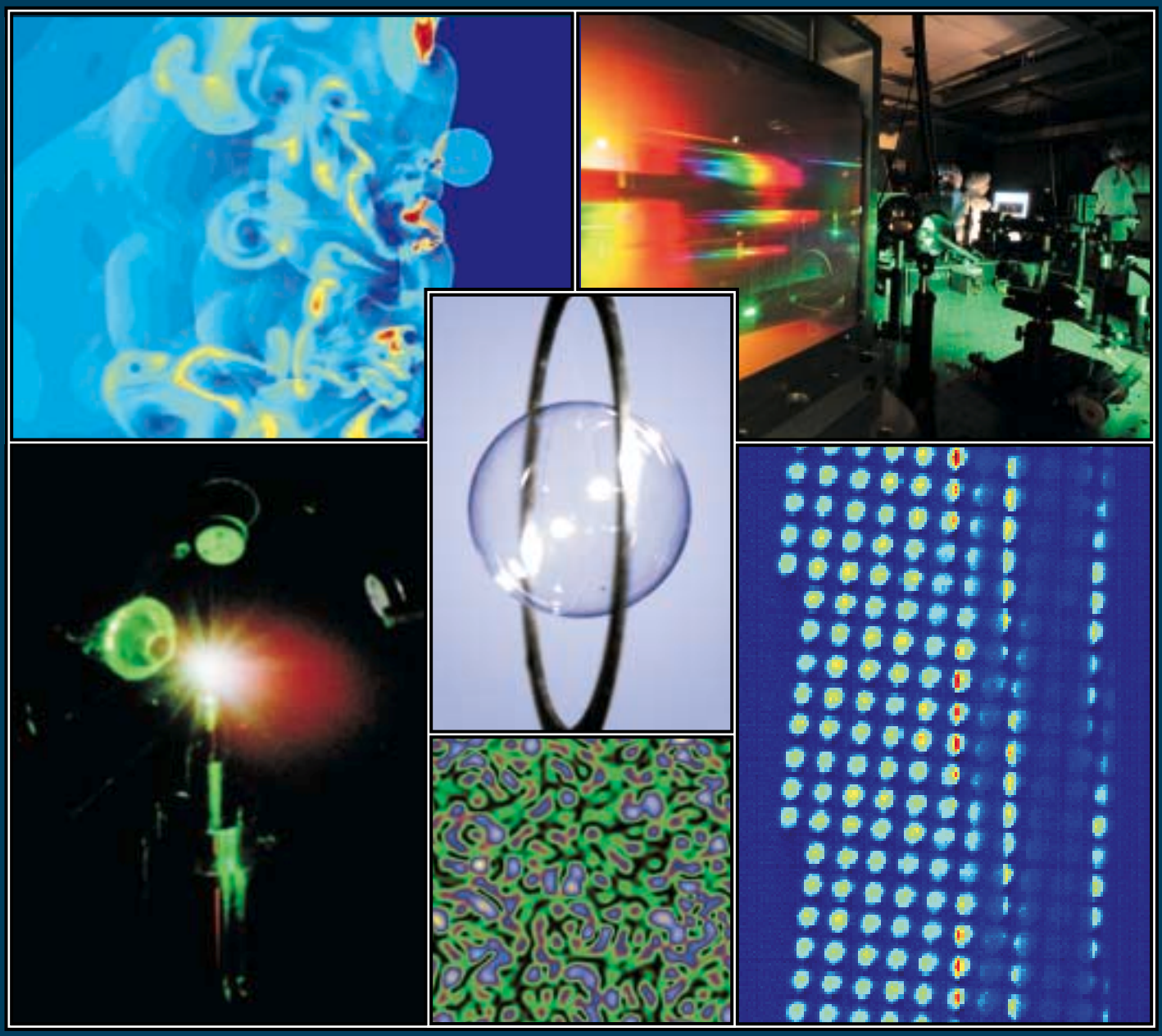

Cover Photos

Upper Left: Foam layers have been the subject of much interest in inertial confinement fusion (ICF) target design. Target designs utilizing foam layers have been proposed for use at LLE on OMEGA, at the National Ignition Facility (NIF), and in reactor-scale ICF fusion facilities. All of these designs make use of laser pulses that launch multiple shocks, which must be well timed. Because a portion of the shock energy is used to homogenize the foam material, the porosity of the foam layer has the potential to change the shock speed and timing. This figure shows a plot of density for a shock propagating through a foam, simulated by the adaptive-mesh refinement code AMRCLAW, in collaboration with Adam Frank and Alexei Poludnenko of the UR's Department of Physics and Astronomy. AMRCLAW is being used to study the effects of porosity on shock timing for wetted-foam layers relevant to OMEGA and NIF target designs.

Lower Left: Thirty-three planar cryogenic target shots were taken on OMEGA in 2002. This photograph was taken on a target shot on which the equation of state (EOS) of liquid deuterium was investigated. These experiments use cryogenic target handling, advanced diagnostics, and the large, uniform laser spots available on OMEGA to provide important data to help clarify previous disagreements between theoretical models and laboratory experiments in this area.

Center: LLE scientists made significant progress in 2002 in developing experimental designs for direct-drive ignition experiments on the NIF. Recent work indicates that it may be possible to carry out high-performance direct-drive implosions on the NIF using the x-ray drive beam configuration. In preparation for future direct-drive experiments on the NIF, a NIF-scale prototype target assembly was demonstrated at LLE and is shown in this photograph. A 3.175-mm-diam spherical target was mounted onto a 125-μm-thick, 7.34-mm-outside-diam Ti ring using four spider silk strands. The target assembly had a resonant frequency of 125 Hz and was compatible with the NIF target chamber geometry.

Lower Center: This image of the on-target laser electric-field intensity was simulated by the parallel, three-dimensional, laser–plasma interaction (LPI) code pF3D. Lawrence Livermore National Laboratory (LLNL) developed the pF3D code primarily for modeling LPI in hohlraum plasmas. LLE scientists are adapting pF3D to simulate direct-drive conditions. The electric-field intensity shown in this figure displays the characteristic speckle pattern produced by distributed phase plates (DPP's). The individual maxima (or "hot spots") can exceed the average incident intensity by several times. Laser-driven parametric scattering instabilities such as stimulated Brillouin scattering (SBS) or decay instabilities like the two-plasmon decay (TPD) are preferentially driven in these hot spots due to the elevated light intensities.

Upper Right: A key element of future ultrahigh-intensity lasers is a stable, high-efficiency laser source capable of generating broad-bandwidth pulses that can be amplified by a high-power amplifier system. Optical parametric chirped-pulse amplification (OPCPA) is a novel laser concept that is well suited for this application. LLE's OPCPA system recently demonstrated one of the highest efficiencies for such systems currently available. The OPCPA concept is based in part on an LLE-invented concept: chirped-pulse amplification (CPA). The CPA idea created a revolution in laser technology by enabling the development of ultrahigh-intensity [i.e., $>10^{15}$ W (petawatt)] lasers. LLE and LLNL are currently collaborating on the development of large diffraction gratings required for petawatt lasers.

Lower Right: This photograph shows an array of capsule core images recorded on an NLUF experiment to study temperature and density gradients in implosion cores of indirect-drive targets. The experiment, carried out by a collaborative team headed by the University of Nevada, Reno, makes use of a new multispectral x-ray imaging diagnostic (MMI-2), which is based on an LLE-developed diagnostic. MMI-2 uses an array of pinholes coupled to a Bragg mirror to record numerous narrowband x-ray images spanning the 3- to 5-keV photon energy range. Each image of the core spans ~75 eV along the spectral axis. Groups of images are combined to produce line-based images. Continuum-based images can also be extracted from the data.

Prepared for
U.S. Department of Energy
San Francisco Operations Office
DOE/SF/19460-468

Distribution Category UC712
October 2001–September 2002

Printed in the United States of America
Available from
National Technical Information Services
U.S. Department of Commerce
5285 Port Royal Road
Springfield, VA 22161

Price codes: Printed Copy A11
Microfiche A01

For questions or comments, contact Laboratory for Laser Energetics, 250 East River Road, Rochester, NY 14623-1299, (585) 275-5286.
Worldwide-Web Home Page: http://www.lle.rochester.edu/

The work described in this volume includes current research at the Laboratory for Laser Energetics, which is supported by New York State Energy Research and Development Authority, the University of Rochester, the U.S. Department of Energy Office of Inertial Confinement Fusion under Cooperative Agreement No. DE-FC03-92SF19460, and other agencies.

University of Rochester
Laboratory for Laser Energetics

DOE/SF/19460-468
January 2003

LLE 2002 Annual Report

October 2001 – September 2002

Inertial Fusion Program and National Laser Users' Facility Program

Contents

Executive Summary

The fiscal year ending September 2002 (FY02) concluded the fifth year of the first renewal of cooperative agreement DE-FC03-92SF19460 with the U.S. Department of Energy (DOE). The cooperative agreement was renewed for an additional five-year period in January 2003. This report—the final one for the first five-year cooperative agreement renewal—summarizes progress and research at the Laboratory for Laser Energetics (LLE), operation of the National Laser Users' Facility (NLUF), and programs concerning the education of high school, undergraduate, and graduate students during the year.

Inertial Confinement Fusion Research

LLE is the lead laboratory for research on direct-drive laser fusion for application and a gain demonstration on the National Ignition Facility (NIF). The NIF is currently under construction at the Lawrence Livermore National Laboratory (LLNL). We have emphasized a number of important areas this past year that should bear directly on the potential success of a direct-drive ignition and burn experiment on the NIF. "First Results from Cryogenic Target Implosions on OMEGA" (p. 49) describes initial results from direct-drive spherical cryogenic target implosions on the 60-beam OMEGA laser system. These experiments are part of the scientific base leading to direct-drive ignition implosions planned for the NIF. Results shown include neutron yield, secondary-neutron and proton yields, the time of peak neutron emission, and both time-integrated and time-resolved x-ray images of the imploded core. The experimental values are compared with 1-D numerical simulations. The target with an ice-layer nonuniformity of $\sigma_{\text{rms}} = 9\ \mu$m showed 30% of the 1-D predicted neutron yield. These initial results are encouraging for future cryogenic implosions on OMEGA and the NIF.

Precision target fabrication is required for a successful ignition demonstration or quality cryogenic experiments on OMEGA. The development of polyimide shells suitable for inertial confinement fusion (ICF) cryogenic experiments on OMEGA is described in an article on target fabrication research beginning on p. 167. We have also determined the associated mechanical properties needed to define the processing conditions for operating the OMEGA Cryogenic Target Handling System (CTHS). Overall, polyimide targets offer a viable alternative to plasma polymer capsules currently in use. The principal advantages of the polyimide material are its high radiation resistance for tritium application and its excellent mechanical properties, which lessen the demanding specifications for the equipment needed to provide cryogenic targets. The single biggest limitation to using polyimide, based on PMDA-ODA chemistry, is the low permeability of the material at room temperature. Methods to increase the permeability are described.

The effects of textures on hydrogen diffusion in nickel was investigated (p. 125). Deuterium and tritium—isotopes of hydrogen—are the primary fuels for ICF, so determining and controlling their rate of diffusion through containment materials are important to the design of ICF facilities. When polycrystalline metals have texture, the preferential orientation of the metals affects hydrogen absorption and diffusion. Hydrogen permeation results show that there are significant differences among the three main textures of nickel membranes. Plating current density has a strong influence on texture development of nickel deposits. The texture of deposits can be easily manipulated by controlling plating conditions. In the experiments performed, textured Ni membranes were prepared using electrodeposition, and the effects of fabrication on their diffusion rates were determined.

In preparation for cryogenic experiments with tritium, we describe LLE's Tritium Recovery System, which is used to clean up the various exhaust streams and to control tritium activity in the gloveboxes (p. 25). This system is optimized for minimum environmental impact and maximum personnel safety. It uses the best-available technologies to extract tritium from inert gas streams in the elemental form. The rationale for the selection of various technologies is discussed in detail. This approach reduces the volumes of effluent that require treatment to the extent practical and also avoids the need to oxidize HT to HTO with its higher radiotoxicity, thereby contributing to safety.

Laser–plasma interactions (LPI) are potentially damaging sources of loss, conversion, and scattering of laser light on a target. We discuss results from pF3D—a parallel, three-dimensional LPI code developed at LLNL for modeling indirect-drive plasmas, which was recently modified for use under direct-drive conditions (p. 93). Unlike indirect drive, modeling direct drive requires simulation of inhomogeneous supersonic flows and density profiles that include a critical surface. The treatment of the critical surface is particularly problematic in codes employing the paraxial approximation for the light waves. The first results of the modified code included realistic simulations motivated by long-scale-length exploding-foil experiments conducted on LLE's 30-kJ, 351-nm, 60-beam OMEGA laser system and intended to represent future NIF direct-drive conditions.

Other LPI research (p. 181) included a linear model of anomalous stimulated Raman scattering from electron-acoustic waves in laser-produced plasmas. Stimulated Raman scattering (SRS) from heavily Landau-damped plasma waves and from electron-acoustic (EA) waves has recently been attributed to nonlinear Bernstein–Green–Kruskal (BGK) wave modes. These phenomena find a simpler, more comprehensive explanation in terms of linear waves in a locally flattened distribution function. The flattening arises from Landau damping of SRS plasma waves (in the case of anomalous SRS) or from perturbations at the EA phase velocity that are then maintained by SRS. Local flattening allows undamped linear EA waves to propagate, as in the original description of these waves by Stix.

"Time-Integrated Light Images of OMEGA Implosions" (p. 1) describes visible-light photographs of imploding OMEGA targets. These beautiful images are used to communicate LLE's mission to the general public. A closer examination of the images revealed a one-to-one correspondence between he bright spots in the image and each of the 60 laser beams. The intensity of the bright spots has been related to refraction and absorption in the plasma surrounding the imploding target. These photographs are now proving to be the basis of a new laser–plasma interaction diagnostic.

Theoretical work (p. 6) presents an analytical model of the nonlinear bubble evolution of single-mode, classical Rayleigh–Taylor (RT) instability at arbitrary Atwood numbers. The model follows the continuous evolution of bubbles from the early exponential growth to the nonlinear regime when the bubble velocity saturates.

The time dependence of electron thermal flux inhibition in direct-drive laser implosions is described beginning on p. 73. The article reports calculations of the nonlocal electron thermal conduction in direct-drive CH target implosions with square pulses by a one-dimensional Fokker–Planck solver combined with a hydrodynamic code. The results show that the electron thermal flux inhibition at the critical surface is time dependent, confirming that a larger flux limiter must be used for shorter-duration pulses. Also, the growth of the Rayleigh–Taylor instability for short-wavelength perturbations is shown to be smaller due to the longer density scale length.

Drive lasers, with known, single-mode modulations, produce nonuniform shocks that propagate into CH targets. The article beginning on p. 68 describes the perturbation of a target by nonuniformities in the drive laser. An optical probe beam is used to measure the arrival of these modulated shocks at various surfaces in the target. Experiments at moderate laser intensities ($\lesssim 10^{13}$ W/cm^2) exhibit behavior that is predicted by hydrocodes and simple scaling laws. This technique may be used to observe various dynamic effects in laser-produced plasmas and shock-wave propagation.

Experiments that control all aspects of nonuniformities in target manufacture, irradiation, and precision drive conditions are required to prepare for a direct-drive ignition experiment on the NIF. A recent experiment (p. 108) has tested the ability of a direct-drive ICF laser pulse shape to vary the adiabat within a target shell. A picket pulse was added to a pulse shape designed to implode a cryogenic shell of D_2 with a ratio α of internal pressure to Fermi-degenerate pressure of 5. The effect of a picket is to strengthen the shock in the outer portion of the shell so that the ablation interface has a large α and the fuel maintains its $\alpha = 5$, resulting in increased stability and improved capsule performance.

Implosion experiments with enhanced beam balance (p. 116) have implemented a new technique that determines the beam peak intensities at target chamber center on a full-power target shot by simultaneously measuring the x-ray flux produced by all 60 beams seen separated on a 4-mm-diam, Au-coated spherical target. Up to nine x-ray pinhole camera images are electronically recorded per shot from which beam-to-beam variations in peak intensity are determined, taking into account view angle and x-ray conversion efficiency. The observed variations are then used to correct the beam energies to produce a more-uniform irradiation. The authors present the results of implosion experiments with enhanced beam balance and comparisons to experiments with standard beam balance.

An investigation of the radial structure of shell modulations near peak compression of spherical implosions (p. 151) required the measurement of the structure of shell modulations at peak compression of implosions using absorption of titanium-doped layers placed at various distances from the inner surface of 20-μm-thick plastic shells filled with D^3He gas. The results show that the peak-compression, time-integrated areal-density modulations are higher at the inner shell surface, which is unstable during the acceleration phase of an implosion, than in the central part of the shell. The outer surface of the shell, which is unstable during the acceleration phase of an implosion, has a modulation level comparable to that of the inner shell surface.

Measurements of the neutron emission from ICF implosions provide important information about target performance that can be compared directly with numerical models. For room-temperature target experiments on OMEGA, the neutron temporal diagnostic (NTD), originally developed at LLNL, is used to measure the neutron burn history with high resolution and good timing accuracy. Since the NTD is mechanically incompatible with cryogenic target experiments because of the standoff required to remain clear of the Cryogenic Target Handling System, a new cryogenic-compatible neutron temporal diagnostic (cryoNTD) has been designed for LLE's standard ten-inch-manipulator (TIM) diagnostic inserters (p. 156). The instrument provides high-resolution neutron emission measurements for cryogenic implosions. The first experimental results of the performance of cryoNTD are presented and are compared to NTD measurements of room-temperature direct-drive implosions.

We have inferred the growth of target areal density near peak compression in direct-drive spherical target implosions with 14.7-MeV deuterium–helium^3 (D^3He) proton spectroscopy on the OMEGA laser system (p. 133). The target areal density grows by a factor of ~8 during the time of neutron production (~400 ps) before reaching 123±16 mg cm^{-2} at peak compression in an implosion of a 20-μm-thick plastic CH target filled with 4 atm of D^3He fuel.

The use of carbon activation as a diagnostic for tertiary neutron measurements is reported beginning on p. 161. The yield of tertiary neutrons with energies greater than 20 MeV has been proposed as a method to determine the areal mass density of ICF targets. Carbon activation is a suitable measurement technique because of its high reaction threshold and the availability of high-purity samples. The isotope ^{11}C decays with a half-life of 20.3 min and emits a positron, resulting in the production of two back-to-back, 511-keV gamma rays upon annihilation. The present copper activation gamma-detection system can be used to detect tertiary-produced carbon activation because the positron decay of ^{11}C is nearly identical to the copper decay used in the activation measurements of 14.1-MeV primary deuterium–tritium (DT) yields. Because the tertiary neutron yield is more than six orders of magnitude lower than primary neutron yield, the carbon activation diagnostic requires ultrapure carbon samples, free from any positron-emitting contamination. Carbon purification, packaging, and handling procedures developed in recent years that reduce the contamination signal to a level low enough for OMEGA are presented. Potential implementation of a carbon activation system for the NIF is also discussed.

Experiments have been performed on OMEGA as part of the Stockpile Stewardship Program to investigate the equation of state of carbonized resorcinol foam, a porous material. A theory that models equation-of-state measurements of porous materials is presented beginning on p. 57. Using the impedance-matching method, the foam Hugoniot was calculated from the well-known equation of state of aluminum and from measured shock speeds over the range of 100 kbar to 2 Mbar.

Laser and Optical Materials Research

A reduced-autocorrelation phase plate design for OMEGA and the NIF has been demonstrated (p. 11). Direct-drive ICF for the NIF requires that the time-averaged rms laser nonuniformity be below the 1% level. The lower spatial frequencies of laser nonuniformity are dangerous to the hydrodynamic stability of the ICF target. A reduced autocorrelation phase design shifts the speckle energy up into the higher spatial frequencies where smoothing by spectral dispersion (SSD) and thermal smoothing in the target corona are most efficient. A novel design method for calculating a reduced correlation phase plate is presented, and the smoothing performance results are compared to a standard phase plate.

We have demonstrated precision spectral sculpting of broadband FM pulses amplified in a narrowband medium (p. 79). Amplification of broadband frequency-modulated (FM) pulses in high-efficiency materials such as Yb^{+3}:SFAP results in significant gain narrowing, leading to reduced on-target bandwidths for beam smoothing and to FM-to-AM conversion. Applying precision spectral sculpting, with both amplitude and phase shaping, before amplifying the broadband FM pulses in narrowband gain media compensated for these effects. The spectral sculpting, for center-line small-signal gains of 10^4, produced amplified pulses that have

both sufficient bandwidths for on-target beam smoothing and temporal profiles that have no potentially damaging amplitude modulation.

A new highly stable, diode-pumped, cavity-dumped, compact Nd:YLF regenerative amplifier (regen) of continuously shaped nanosecond pulses with a gain of ~10^9 for the front-end laser system of OMEGA is discussed beginning on p. 103. High output energy, long-term energy and temporal pulse shape stability, and high-quality beam profile have been demonstrated. Reliability, simplicity, modular design, and compactness are key features of this new diode-pumped regenerative amplifier.

To study the connection between the pulsed-laser energy absorption process and film damage morphology we used a SiO_2-thin-film system with absorbing gold nanoparticles (p. 30). We show that, at low laser fluences (below the threshold where damage can be detected optically), the probability of crater formation and the amount of the material vaporized are almost independent of the particle size. Inhomogeneities in the particle environment are responsible for variances in the observed particle/damage crater correlation behavior. In the proposed damage mechanism, the initial absorption is confined to the nanoscale defect. Energy absorbed by the defect quickly heats the surrounding matrix, changing it from a transparent to an absorbing medium, which creates a positive-feedback mechanism that leads to crater formation.

Advanced Technology

A series of thin, hydrogenated amorphous carbon films have been deposited using the saddle-field deposition configuration (p. 44). These films are a precursor to depositing tritiated films. Smooth, low-porosity films up to 15 μm thick and with densities up to 2 g/cm^3 have been grown. The internal structure of the films is featureless. Operating pressure plays an important role in modulating the film quality, growth rate, and density. Eliminating the substrate bias reduces negative ion incorporation in the films to help increase film density and improve film quality.

A theoretical investigation of a semiconductor quantum dot interacting with a strongly localized optical field, as encountered in high-resolution, near-field optical microscopy, is reported (p. 139). The strong gradients of these localized fields suggest that higher-order multipolar interactions will affect the standard electric dipole transition rates and selection rules. For a semiconductor quantum dot in the strong confinement limit, Zurita-Sanchez and Novotny have calculated the interband electric quadrupole absorption rate and the associated selection rules, finding that the electric quadrupole absorption rate is comparable with the absorption rate calculated in the electric dipole approximation.

The femtosecond response of a freestanding LT-GaAs photoconductive switch is discussed beginning on p. 88. A novel, freestanding LT-GaAs photoconductive switch has a femtosecond response time. The switch was formed by patterning a 1-mm-thick layer of a single-crystal LT-GaAs into a 5-μm by 15-μm bar. The bar was separated from its GaAs substrate and placed across a gold coplanar transmission line deposited on a Si wafer. The switch was excited with 110-fs-wide optical pulses, and its photoresponse was measured with an electro-optic sampling system. Using 810-nm optical radiation, 470-fs-wide electrical transients (640-GHz bandwidth) were recorded.

An investigation of the electric-field-induced motion of polymer cholesteric liquid crystal flakes in a conductive fluid is described beginning on p. 83. Polymer cholesteric liquid crystal flakes suspended in a fluid with non-negligible conductivity can exhibit motion in the presence of an ac electric field. The platelets have a strong selective reflection, which is diminished or extinguished as the flakes move. Flake motion was seen within a specific frequency bandwidth in an electric field as low as 5 mV_{rms}/mm.

New results on the time-resolved dynamics of the superconducting-to-resistive transition in dc-biased epitaxial $YBa_2Cu_3O_{7-x}$ (YBCO) microbridges, excited by nanosecond-long current pulses, are reported beginning on p. 40. The resistive switching was induced by the collaborative effect of both the Cooper-pair bias current and the quasiparticle pulse excitation, which together always exceeded the bridge critical current, forming the supercritical perturbation. The experimental dynamics was analyzed using the Geier and Schön (GS) theory, which was modified to include the dc bias. The resistive state was established after a delay time t_d, in agreement with the GS model, which depended in a nonlinear way on both the excitation pulse magnitude and the bridge dc bias.

A great deal of interest has been generated by the discovery of superconductivity in hexagonal magnesium borides because of not only MgB_2's high critical temperature and current density but also its lower anisotropy, larger coherence length, and higher transparency of grain boundaries to current flow.

We have for the first time fabricated MgB_2 superconducting films on flexible substrates (p. 130). Our process to deposit these films on large-area foils (up to 400 cm^2) and, after processing, cut them into any shapes (e.g., stripes) with scissors or bend them multiple times showed that the films suffer no observed degradation of their superconducting properties.

We describe measurements of the time delay of the resistive-state formation in superconducting NbN stripes illuminated by single optical photons (p. 186). A 65(±5)-ps time delay in the onset of a resistive-state formation in 10-nm-thick, 200-nm-wide NbN superconducting stripes exposed to single photons was measured. This delay in the photoresponse decreased down to zero when the stripe was irradiated by multiphoton (classical) optical pulses. The NbN structures were kept at 4.2 K, well below the material's critical temperature, and were illuminated by 100-fs-wide optical pulses. The time-delay phenomenon is explained within the framework of a model based on photon-induced generation of a hotspot in the superconducting stripe and subsequent, supercurrent-assisted resistive-state formation across the entire stripe cross section. The measured time delays in both the single-photon and two-photon detection regimes agree well with the Tinkham model's theoretical predictions of the resistive-state dynamics in narrow, ultrathin superconducting stripes.

OMEGA System Performance

Increased user demand was met in FY02 by expanding the available shot time during select weeks. Ten weeks were extended to four shot days by shooting one 8-h day, two 12-h days, and one 16-h day. This adjustment raised the total executed shots by 11%—from 1289 in FY01 to 1428 in FY02 (see Table 92.V, p. 193). Shaped-pulse cryogenic implosions highlighted the ongoing development of direct-drive cryogenic capability. A total of 21 spherical cryogenic D_2 targets were shot on OMEGA. Some of the cryogenic target shot time was devoted to characterization and system reliability improvements. Planar cryogenic target capability was also activated, and many shots were executed under LLE's Stockpile Stewardship Program (SSP) campaign. Highlights of other achievements and active projects as of the end of FY02 include the following:

- An IR streak camera with pulse-shape analysis software became a key operational tool to optimize pulse-shape performance. Combined with some changes to the control system for pulse-shape setup and upgrades to the regenerative oscillator hardware, the changes have resulted in dramatic improvements to delivered-pulse-shape performance.
- Infrared amplification occurs across a large variety of gain stages. By far, the highest gain stage is the regenerative (regen) amplifier, with 1×10^5 gain. One of the flash-lamp-pumped laser regens for OMEGA was replaced by a diode-pumped version that operates consistently without feedback stabilization. This diode-pumped laser improves pulse-shape performance. The remaining regens on OMEGA will be changed over to the new design in FY03.
- The distributed polarization rotator (DPR)—one of the key optics for beam smoothing on target—was modified for remote removal and reinstallation. The cassette-style removal system retracts the optic from the UV beamline into a protective housing. Having the capability to insert or remove these components improves flexibility for reconfiguring to indirect-drive setups. The full 60-beam complement of actuators will be completed early in FY03.
- The OMEGA laser is designed to provide a high degree of uniformity and flexibility in target illumination. The ability to impose a controlled asymmetric on-target irradiation pattern was developed and used extensively. This capability is used to benchmark multidimensional hydrodynamic simulations by imposing known nonuniform compression conditions on spherical targets. It is also used to modify laser-irradiation conditions for beam-to-beam x-ray yield balance.
- Modifications to the stage-A alignment sensors on OMEGA have streamlined an item of flexibility frequently exploited by LLE principal investigators. The backlighter driver alignment handoff to the OMEGA beamlines was re-engineered to expedite configuration setups that require the use of this source.
- Scientists and engineers from Lawrence Livermore National Laboratory along with LLE collaborators successfully implemented a green (second harmonic, 527 nm) target irradiation capability on one of the 60 OMEGA beams. This capability utilizes the existing OMEGA frequency-conversion crystals with the tripler detuned so that maximum 527-nm conversion is achieved.
- A revised set of direct-drive phase plates was designed and is being fabricated to further optimize irradiation uniformity for spherical implosions. These optics are going to be available in mid-FY03 and are expected to have improved smoothing characteristics in the mid-spatial-frequency range.

National Laser Users' Facility and External Users' Programs

FY02 was a record year for external user activity on OMEGA. As reported in the section beginning on p. 194, a total of 698 target shots were taken on OMEGA for external users' experiments in FY02. This is the highest number of target shots ever taken by external users on OMEGA in a single year and represents a 16% increase in external user shots over FY01. The external user shots accounted for 49% of the total OMEGA target shots in FY02. External users' experiments were carried out by eight collaborative teams under the National Laser Users' Facility (NLUF) Program as well as collaborations led by scientists from Lawrence Livermore National Laboratory (LLNL), Los Alamos National Laboratory (LANL), Sandia National Laboratory (SNL), the Nuclear Weapons Effects Testing (NWET) Program, and the Commissariat à l'Énergie Atomique (CEA) of France.

1. NLUF Programs

FY02 was the second of a two-year period of performance for the eight NLUF programs approved for FY01–FY02 experiments. The eight NLUF campaigns received a total of 118 target shots on OMEGA in FY02.

The Department of Energy (DOE) issued solicitations in mid-FY02 for NLUF proposals to be carried out in FY03–FY04. DOE raised the NLUF funding allocation to $800,000 for FY03 and is expected to increase it to $1,000,000 for FY04 to accommodate the high level of interest shown in the use of OMEGA to carry out experiments of relevance to the National Nuclear Security Agency (NNSA) Stockpile Stewardship Program.

A total of 13 NLUF proposals were submitted to DOE for consideration for FY03–FY04 support and OMEGA shot allocation. An independent DOE Technical Evaluation Panel reviewed the proposals and recommended that up to nine of the proposals be approved for partial funding and shot allocation during FY03–FY04. Table 92.VI (p. 195) lists the successful proposals.

2. FY02 NLUF Experiments

The eight NLUF programs carried out in FY02 included

- *Atomic Physics of Hot, Ultradense Plasmas*
- *Determination of Temperatures and Density Gradients in Implosion Cores of OMEGA Targets*
- *Studies of the Fundamental Properties of High-Energy-Density Plasmas*
- *High-Spatial-Resolution Neutron Imaging of Inertial Fusion Target Plasmas Using Bubble Neutron Detectors*
- *Examination of the "Cone-in-Shell" Target Compression Concept for Asymmetric Fast Ignition*
- *Supernova Hydrodynamics on the OMEGA Laser*
- *Studies of the Dynamic Properties of Shock-Compressed FCC Crystals by* In-Situ *Dynamic X-Ray Diffraction*
- *Optical Mixing of Controlled Stimulated Scattering Instabilities (OMC SSI) on OMEGA*

3. FY02 LLNL OMEGA Experimental Program

The LLNL program on OMEGA in FY02 totaled 406 target shots for target ignition physics, high-energy-density science, and NWET (Nuclear Weapons Effects Testing). This represents a 30% increase over the target shots taken by LLNL on OMEGA in FY01. Highlights of these experiments include laser–plasma interactions, cocktail hohlraums, x-ray Thomson scattering, albedo experiments, hot hohlraums, gas-filled radiation sources, dynamic hohlraums, nonideal implosions, double-shell implosion experiments, charged-particle spectrometry in indirect-drive implosions, and IDrive.

4. FY02 LANL OMEGA Experimental Program

The LANL program on OMEGA in FY02 comprised a total of 132 target shots in support of cylindrical mix (CYLMIX) experiments; the Stockpile Stewardship Program; asymmetric direct-drive implosions; double-shell implosions; hydrodynamic jet experiments in collaboration with AWE, LLNL, and LLE; shock-breakout measurements in collaboration with SNL; and development of phase-2 nuclear diagnostics for the NIF.

5. FY02 SNL OMEGA Programs

SNL carried out a total of 24 target shots on the OMEGA laser in FY02 and also participated in several of the campaigns led by other laboratories. The SNL-led campaigns included indirect-drive ablator shock coalescence; indirect-drive ablator shock velocity at 50 Mbar; indirect-drive ablator x-ray burnthrough measurements; and time- and spatially resolved measurements of x-ray burnthrough and re-emission in Au and Au:Dy:Nd foils.

6. CEA

CEA had four half-day dedicated shot opportunities on OMEGA during FY02. A total of 19 target shots were provided for experiments including tests of the LMJ three-ring symmetry and other aspects of indirect-drive targets. In addition, CEA participated in collaborative experiments on imaging the neutron core emission using the CEA-provided neutron-imaging system (NIS).

Education at LLE

As the only major university participant in the National ICF Program, education continues to be an important mission for the Laboratory. Graduate students are using the world's most powerful ultraviolet laser for fusion research on OMEGA, making significant contributions to LLE's research activities. Twenty-four faculty from five departments collaborate with LLE's scientists and engineers. Presently 57 graduate students are pursuing graduate degrees at the Laboratory, and LLE is directly funding 38 University of Rochester Ph.D. students through the Frank J. Horton Fellowship Program. The re-search includes theoretical and experimental plasma physics, high-energy-density plasma physics, x-ray and atomic physics, nuclear fusion, ultrafast optoelectronics, high-power-laser development and applications, nonlinear optics, optical materials and optical fabrications technology, and target fabrication. Technological developments from ongoing Ph.D. research will continue to play an important role on OMEGA.

One hundred fifty-four University of Rochester students have earned Ph.D. degrees at LLE since its founding. An additional 81 graduate students and 23 postdoctoral positions from other universities were funded by NLUF grants. The most-recent University of Rochester Ph.D. graduates and their thesis titles are

Thomas Gardiner	*Astrophysics Stellar Evolution*
Andrei Kanaev	*Propagation of Laser Beams Smoothed by Spectral Dispersion in Long-Scale-Length Plasmas*
Feng-Yu Tsai	*Engineering Vapor-Deposited Polyimides*

Approximately 46 University of Rochester undergraduate students participated in work or research projects at LLE this past year. Student projects include operational maintenance of the OMEGA laser system; work in laser development, materials, and optical-thin-film coating laboratories; programming; image processing; and diagnostic development. This is a unique opportunity for students, many of whom will go on to pursue a higher degree in the area in which they gained experience at the Laboratory.

In addition, LLE directly funds research programs within the MIT Plasma Science and Fusion Center, the State University of New York (SUNY) at Geneseo, and the University of Wisconsin. These programs involve a total of approximately 18 graduate and 23 undergraduate students from other universities.

For the past 12 years LLE has run a Summer High School Student Research Program (p. 190) in which this year 15 high school juniors spent eight weeks performing individual research projects. Each student is individually supervised by a staff scientist or an engineer. At the conclusion of the program, the students make final oral and written presentations on their work. The reports are published as an LLE report.

In 2002, LLE presented its sixth William D. Ryan Inspirational Teacher Award to Mr. James Keefer, a physics and chemistry teacher at Brockport High School. Alumni of our Summer High School Student Research Program were asked to nominate teachers who had a major role in sparking their interest in science, mathematics, and/or technology. This award, which includes a $1000 cash prize, was presented at the High School Student Summer Research Symposium. Mr. Keefer was nominated by Ms. Priya Rajasethupathy, a 2000 participant in the program.

Robert L. McCrory
Director

Time-Integrated Light Images of OMEGA Implosions

Introduction

Beginning in the spring of 2001, a series of remarkable photographs were taken that clearly show spherical target implosions as they might appear to the naked eye. Not surprisingly, the spherical target itself is not visible. The dominant feature in the photographs is the reflection of the laser beams hitting the target. These reflections appear as bright spots of light, organized in a very symmetric pattern.

These first experimental photographs, taken with aesthetics in mind more than quantitative measurement, were part of a series of visually appealing photographs of the inside of the target chamber. They represent a time-integrated picture of the target shot, from beginning to end (Fig. 89.1).

Upon closer scrutiny these photographs are found to contain useful and interesting information about the interaction of the laser beams with the plasma. The location and brightness of the spots as well as the number that are visible raised some questions, and the explanations were not intuitively obvious.

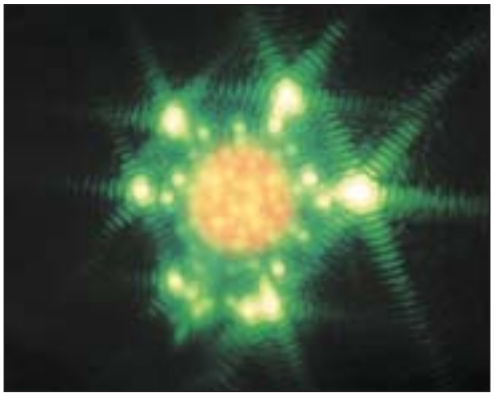

E11509

Figure 89.1
A time-integrated photograph showing a spherical target implosion. Beam reflections dominate the image and provide useful information about laser–plasma interactions. The concentric rings and spokes around each spot are camera artifacts. Note that almost 60 spots are visible, despite this being a picture of only one side of the target.

In light of this, an effort was made to make the photographs more quantitative. A UV transmission filter was added to the camera, and the film was switched from color to monochromatic, which allows a quantitative evaluation of the images. The filter passed 351-nm light, corresponding to the incident laser wavelength (Fig. 89.2).

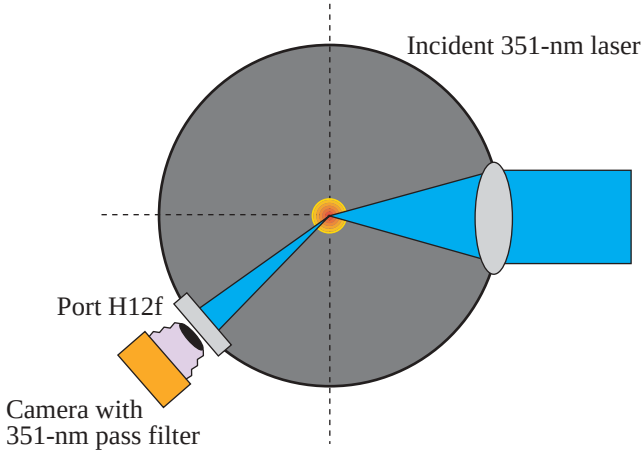

E11510

Figure 89.2
A rough layout of the experiment. Laser beams enter the target chamber and strike the spherical target. Reflections from the beams are seen and recorded by the camera in port H12f.

At the same time, in an effort to simulate the images, a program was written that performs ray tracing and absorption on the simulated laser beams. This program is designed to show whether the usual physical assumptions about laser–plasma interactions can explain the main features of the photographs. The simulation also adds time resolution to the images, explaining the photographs in a new light.

Experiment

The first photographs (Fig. 89.1) were taken on color film by a camera mounted on a port outside of the target chamber. This port is slightly off center from a symmetry axis and contributes to a small asymmetry in the photographs. The

camera is operated in an unconventional way by adding a number of magnifying objective lenses in series. This makes it difficult to know precisely what the actual *f* number and focal length are, particularly since the objectives were not designed for 351-nm light.

Several qualitative features, however, are apparent immediately, the most important being that each spot is very distinct and corresponds to one particular laser beam. The outer spots appear to be larger and brighter than the inner spots, and the target itself is washed out. The origin of the soft circular glow in Fig. 89.1 cannot be easily identified, but it does not accurately portray the size of the target. When color film is used, the area appears red. This may be light scattered from the quarter-critical surface due to either Raman scattering or the two-plasmon-decay instability.

Perhaps the most-interesting feature is that all 60 beam spots are visible, which, considering that the photograph shows only one side of the target, was not expected. It means that the beams behind the target are visible as well as the beams incident on the front of the target. This is especially striking considering that the target turns opaque long before the laser pulse reaches its maximum.

The addition of the UV filter and monochromatic film changed the look of the photographs (Fig. 89.3). The spots are much smaller and well defined, and several features are now visible that had been obscured. Most notable is the streaking of the outer spots, indicating that, over the course of the shot, these spots move appreciatively from their original position in the radial direction. These outer spots also overexposed the film, showing that they contain much more energy than the inner spots, which are barely visible in places.

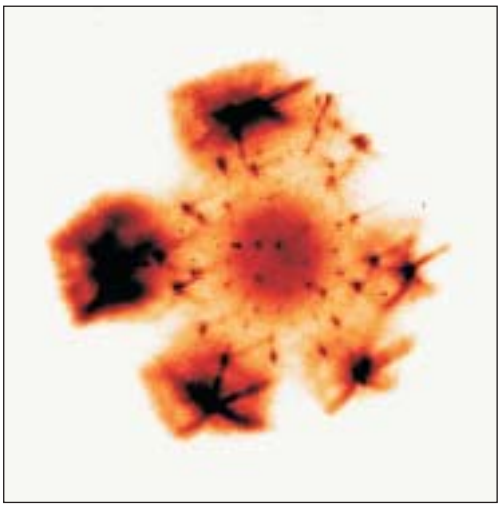

E11511

Figure 89.3
A UV photograph of the target implosion. This picture shows precise, small, clearly defined beam reflection spots. The outer spots suffer from overexposure and camera artifacts, masking some important details.

These monochromatic photographs were digitized for direct comparison to the output of the simulation.

Theory and Simulation

The index of refraction[1] of a plasma depends on the electron density, as shown in Eq. (1):

$$\mu = \sqrt{1 - n_e / n_c}\,, \tag{1}$$

where μ is the index of refraction, n_e is the electron density, and n_c is the critical density where the local plasma frequency equals the incident light frequency. A beam of light entering a region where $n_e > n_c$ will be reflected and/or absorbed at the critical-density surface. A ray of light passing through a plasma of density $n_e < n_c$ can be bent by refraction. Refraction depends on the direction of the ray and the direction and magnitude of the plasma density gradient.

This introduces the possibility that the laser beams striking the back of the target are refracted through the plasma into the camera lens. This is particularly likely since each laser spot is focused to be slightly bigger than the spherical target, with about 5% of the incident laser energy passing around the original target sphere. The beams striking the front of the target may be refracted and reflected as they approach the critical surface, again having their path bent into the camera lens. In this way, all 60 beams can become visible in the photograph.

The path of a ray through a medium of varying index of refraction is given by[2]

$$\frac{d}{ds}\left(\mu \frac{d\mathbf{x}}{ds}\right) = \nabla\mu \quad (\text{Snell's law}), \tag{2}$$

where s is the path taken by the ray and $\mathbf{x}$ is the position vector along the path.

This equation can be rewritten in a form suitable for numerical simulation:

$$\mathbf{x}_{i+1} = \mathbf{x}_i + \frac{d\mathbf{x}_i}{ds} ds, \tag{3}$$

$$\mu_{i+1} \frac{d\mathbf{x}_{i+1}}{ds} = \mu_i \frac{d\mathbf{x}_i}{ds} + \nabla\mu(\mathbf{x}) ds. \tag{4}$$

Given the plasma density as a function of position, Eqs. (1), (3), and (4) are sufficient to trace the path of a ray through a plasma.

The simulation takes as input a *LILAC,* 1-D plasma density profile, which gives density as a function of radius. One density profile is given for each time step of 100 ps. The plasma is assumed to be stationary while the light passes through it. Once the density is read in, the index of refraction and its gradient are calculated as a function of radius.

Rays are then traced through this plasma by incrementing *ds* in small steps. Each laser beam is assumed to be focused in such a way that it is slightly wider than the target and composed of many parallel rays. Because the beams are slightly wider than the target, some rays strike the target center and are reflected straight back, some miss and go straight by, and the rest are scattered through the 180° between those two extremes.

Rather than tracing every possible path, the program iteratively throws away all the rays that do not land on the camera lens. After identification of the exact region of the laser that strikes the lens, this region is traced with many rays, yielding higher resolution.

The ray tracing can be done in two dimensions since any single ray remains in its plane of incidence. This plane is then rotated to trace out the full shape of the spot in the image. This process is then repeated for each laser beam. The position of the camera and the position of each beam are read in from a text file, making it easy to switch the parameters for different target shots.

The result of this ray tracing is translated into image space by taking into account the angle at which each ray strikes the camera lens. By rotating each beam and taking into account the geometry of the tank, the full 2-D photograph is reconstructed (Fig. 89.4).

This process is repeated in 100-ps steps until 1200 ps = 1.2 ns have passed. By this point the laser beam has switched off and no longer contributes to the image. The separate time-resolved images are saved and compiled into one time-integrated image to compare with the experimental data.

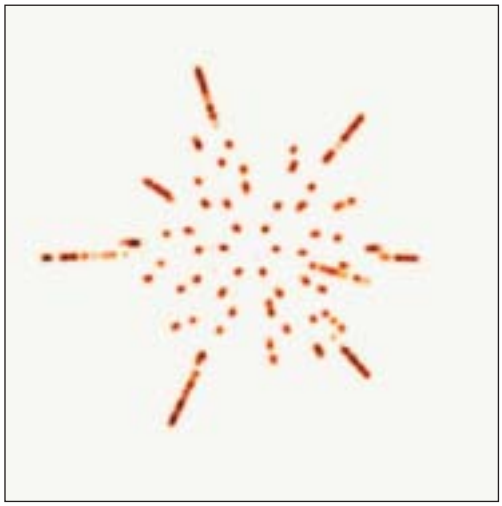

E11512

Figure 89.4
A simulated time-integrated image of an imploding target in the light of the 60 OMEGA beams driving it. This image shows the apparent locations of each beam reflection as seen from port H12f.

The simulations also allow for laser light absorption, via inverse bremsstrahlung in the plasmas:

$$\frac{dI}{ds} = -kI, \tag{5}$$

where the absorption coefficient[3]

$$k = \frac{16\pi Z^2 n_e n_i e^6 \ln\Lambda(\upsilon)}{3c\upsilon^2 \left(2\pi m_e k_b T\right)^{3/2} \left(1 - \upsilon_p^2/\upsilon^2\right)^{1/2}}. \tag{6}$$

The radial intensity distribution of the beam is approximated with a gaussian, yielding data about the beam power as it strikes the camera lens.

Results

The simulations are in good agreement with the experimental photograph (Fig. 89.5). The spots appear in the same symetrical pattern and show roughly the same relative levels of brightness.

The time resolution of the simulated images explains many of the features seen in the photograph. It is now apparent that most of the image is formed in the first 300 ps as a reflection from the solid sphere, with only a very thin plasma corona around it. As the plasma expands and fully forms, absorption takes over and the reflected intensity drops significantly. The outer beam spots seen in Figs. 89.1–89.4 are due to beams behind the target and their spill-over past the target. They suffer the least absorption as they are refracted into the camera. They are still clearly visible even at the end of the laser pulse, which explains the overexposure these spots produced on the film, as well as the outward radial displacement with time (Fig. 89.6).

Conclusion and Discussion

The simulation appears to explain most of the main features of the experimental photographs. The time resolution yields further information that was not available from the time-integrated photographs.

A careful comparison of the simulated images with the experimental photographs is limited by the setup of the camera. The camera has several objective lenses, making it difficult to know the exact path of the light through them. Port H12f of the target chamber is also not completely centered within the six beams surrounding it, leading to asymmetry in the photographs, which is duplicated in the simulation.

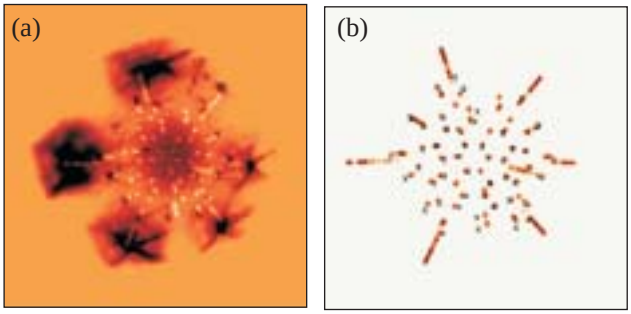

E11513

Figure 89.5
The remarkable agreement between simulated and actual photographs is apparent in the overlay of the simulations on the experimental image. Small disagreements in position and intensity are expected since the simulation is based on a 1-D plasma profile. In (b) small x's have been drawn on the simulated image corresponding to experimental spot position. Several predicted spots seem to be obscured on the experimental photograph. It is expected that with better camera equipment and filtering, these spots will be visible.

More importantly, however, an overall scaling problem was found with the camera. The exact scale of the experimental photographs is not completely certain. The photographs, taken on film, must be digitized in order to compare them with computer simulation.

In light of this, work has begun on a new camera designed to take quantitative digital photographs. This camera will be constructed of reflective optics, and the exact path of the light through it will be known. The simulation will be improved as well. When higher-quality images become available, it will be useful to add effects like plasma velocity and Doppler shifting to the code.

Further development of these ideas will likely address the potential of the new apparatus as a diagnostic for cryogenic target shots. The centering of the target, pointing of the beams, and early power-balance nonuniformities can all potentially be examined using this diagnostic. Further work will be devoted to determining the limits of the simulation and the experimental photographs.

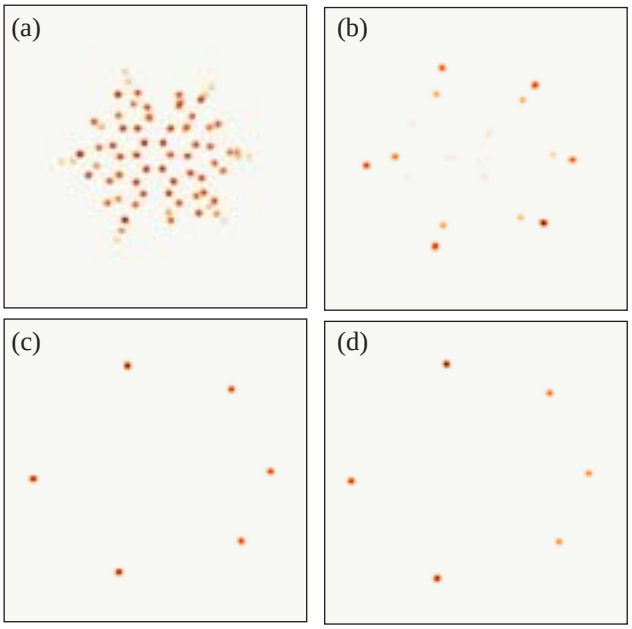

E11514

Figure 89.6
A series of simulated photographs showing the image seen by the camera at (a) 100 ps, (b) 400 ps, (c) 800 ps, and (d) 1100 ps. Reflection dominates until ~300 ps, when absorption in the plasma grows to almost 100%. From this point on, beams that refract from behind the target form most of the image.

ACKNOWLEDGMENT

This work was supported by the U.S. Department of Energy Office of Inertial Confinement Fusion under Cooperative Agreement No. DE-FC03-92SF19460, the University of Rochester, and the New York State Energy Research and Development Authority. The support of DOE does not constitute an endorsement by DOE of the views expressed in this article.

REFERENCES

1. F. F. Chen, *Introduction to Plasma Physics and Controlled Fusion*, 2nd ed., Vol. 1 (Plenum Press, New York, 1984).
2. M. Born and E. Wolf, in *Principles of Optics: Electromagnetic Theory of Propagation, Interference and Diffraction of Light*, 4th ed. (Pergamon Press, New York, 1970), pp. 121–123.
3. T. W. Johnston and J. M. Dawson, Phys. Fluids **16**, 722 (1973).

Analytical Model of Nonlinear, Single-Mode, Classical Rayleigh–Taylor Instability at Arbitrary Atwood Numbers

An interface between two fluids subject to an external force pointing from the heavier to the lighter fluid is hydrodynamically unstable[1] [Rayleigh–Taylor (RT) instability]. This instability plays an important role in astrophysics and inertial confinement fusion.[2] In the limit of small perturbation amplitudes ($k\eta << 1$, where k is the perturbation wave number), the perturbations grow exponentially[1] $\eta \sim \eta_0 e^{\gamma t}$ with the growth rate $\gamma = \sqrt{A_T k g}$, where $A_T = (\rho_h - \rho_l)/(\rho_h + \rho_l)$ is the Atwood number, ρ_h and ρ_l are the densities of heavier and lighter fluids, respectively, g is the interface acceleration, and η_0 is the initial amplitude. As the amplitude becomes large enough ($k\eta \sim 1$), the interface can be divided into the spikes of the heavier fluid penetrating into the lighter fluid and bubbles of the lighter fluid rising into the heavier fluid. The exponential growth of the bubble amplitude changes to the linear-in-time growth[3–8] $\eta \sim U_b t$, where U_b is the bubble velocity. Such a transition is commonly referred to as a "nonlinear saturation," although, strictly speaking, only the bubble velocity saturates, not the amplitude. To describe the evolution of the perturbation after the saturation, two analytical approaches have been proposed in the past.[3–8] The weakly nonlinear theories[5] (up to the third-order accuracy in $k\eta$) capture only the initial slowing down of the exponential growth. The other approach uses an expansion of the perturbation amplitudes and conservation equations near the tip of the bubble[3,4,7,8] (or spike[8]) up to the second or higher order in the transverse coordinate. In the past, the second approach has been applied only to the fluid–vacuum interfaces ($A_T = 1$)[3,4,6–8] and has been shown to be in good agreement with numerical simulations and experimental data. In this article, the Layzer's theory will be extended to include finite density of the lighter fluid ($A_T \le 1$). We also report an exact solution of conservation equations (valid at the tip of the bubble) in the form of a convergent Fourier series.

First, we consider two irrotational, incompressible, inviscid fluids in two-dimensional (2-D) geometry. The fluids are subject to an external acceleration g pointing from the heavier to the lighter fluid. The y axis is chosen in the direction of the density gradient. The velocity potential ϕ in the absence of viscosity and thermal conduction obeys the Laplace equation

$$\Delta\phi = \partial_x^2\phi + \partial_y^2\phi = 0. \tag{1}$$

In addition, the function ϕ must satisfy the following jump conditions at the fluid interface $y = \eta(x,t)$:

$$\partial_t \eta + v_x^h \partial_x \eta = v_y^h, \tag{2}$$

$$\left[\left[v_y - v_x \partial_x \eta\right]\right] = 0, \tag{3}$$

$$\left[\left[\rho\left(\partial_t\phi + \frac{1}{2}v^2 + g\eta\right)\right]\right] = f(t), \tag{4}$$

where $[[Q]] = Q^h = Q^l$ (superscripts h and l denote the heavy- and light-fluid variables, respectively) and $f(t)$ is an arbitrary function of time. Equations (2) and (3) are derived from the mass-conservation equation and continuity condition for the velocity component normal to the fluid interface, and Eq. (4) is the Bernoulli's equation. Following Ref. 4, we expand Eqs. (2)–(4) and the interface amplitude η near the tip of the bubble [localized at the point $\{x,y\} = \{0, \eta(0,t)\}$] to the second order in x, $\eta = \eta_0(t) + \eta_2(t)x^2$. The function $\eta_2(t)$ is related to the bubble curvature R as $R = -1/(2\eta_2)$. To satisfy boundary conditions (2)–(4) (six equations), we need six unknowns. Thus, in addition to the functions $\eta_0(t)$, $\eta_2(t)$, and $f(t)$, the velocity potential must contain three unknowns. We write the velocity potential near the bubble tip in the following form:

$$\phi^h = a_1(t)\cos(kx)e^{-k(y-\eta_0)}, \tag{5}$$

$$\phi^l = b_1(t)\cos(kx)e^{k(y-\eta_0)} + b_2(t)y. \tag{6}$$

The form of the light-fluid potential [Eq. (6)] will be verified later using the results of numerical simulations. Substituting Eqs. (5) and (6) into the boundary conditions (2)–(4) and

expanding the latter near the bubble tip gives

$$\dot{\eta}_2 = -\dot{\eta}_0 \frac{k}{2}\left(k + 6\eta_2\right), \tag{7}$$

$$\ddot{\eta}_0 \frac{k^2 - 4A_T k\eta_2 - 12A_T\eta_2^2}{2\left(k - 6\eta_2\right)}$$

$$+ \dot{\eta}_0^2 k^2 \frac{\left(4A_T - 3\right)k^2 + 6\left(3A_T - 5\right)k\eta_2 + 36A_T\eta_2^2}{2\left(k - 6\eta_2\right)^2}$$

$$+ A_T g\eta_2 = 0. \tag{8}$$

Equation (7) can be integrated directly. The result, assuming initial sinusoidal perturbation with amplitude $\eta_0(0)$, takes the form

$$\eta_2 = -\frac{k}{6} + \left[\frac{k}{6} - \eta_0(0)\frac{k^2}{2}\right]e^{-3k\left[\eta_0 - \eta_0(0)\right]}. \tag{9}$$

Furthermore, substituting Eq. (9) into Eq. (8), the latter can be integrated to give an analytic expression for the bubble velocity. This expression is very lengthy, however, and will be reported elsewhere. In practice, one can easily calculate the bubble amplitude by solving the system (7)–(8) using, for example, the *Mathematica* software package.[9] Next, we obtained an asymptotic solution for the bubble velocity by taking the limit of $t \to \infty$ in Eqs. (9) and (8). This gives

$$\eta_2 \to -\frac{k}{6}, \quad U_b \to \sqrt{\frac{2A_T}{1 + A_T}\frac{g}{3k}}. \tag{10}$$

The last equation agrees with the prediction of the drag–buoyancy model.[6] Solution of Eq. (8) provides a continuous bubble evolution from the linear to the nonlinear regime, while the drag–buoyancy model calculates only the asymptotic behavior.

Next, we verify the choice of the velocity potential in the light fluid [Eq. (6)] by comparing the velocity profiles obtained from Eq. (6) and full numerical simulation. For such purpose, we first calculate the coefficients b_1 and b_2 as functions of time:

$$b_1 = \dot{\eta}_0 \frac{6\eta_2 + k}{k\left(k - 6\eta_2\right)}, \quad b_2 = \frac{12\dot{\eta}_0\eta_2}{6\eta_2 - k}. \tag{11}$$

Since $\eta_2\left(t \to \infty\right) = -k/6$, then $b_1 \to 0$ and $b_2 \to \dot{\eta}_0$. Then, substituting Eq. (11) into the definition of the light-fluid velocity,

$$v_x^l = -b_1 k \sin(kx) e^{k(y - \eta_0)}$$

and

$$v_y^l = b_1 k \cos(kx) e^{k(y - \eta_0)} + b_2,$$

we find that asymptotically, the light-fluid velocity component parallel to the acceleration becomes flat near the tip of the bubble (no x or y dependence), and the transverse velocity component in that region goes to zero. To confirm this result, we performed a 2-D simulation using an incompressible, inviscid Eulerian code. Figure 89.7 shows the velocity profiles (v_x and v_y) at two different times, calculated using results of simulations for the fluid interface with $A_T = 0.4$ and the initial amplitude of velocity perturbation $v_0 = 0.01\sqrt{g\lambda}$, where λ is the perturbation wavelength. The vertical lines show the interface between the heavier and lighter fluids (the heavier fluid is on the right side of the lines). Velocity v_y is plotted at the position of the bubble center ($x = 0$), and the transverse velocity v_x is plotted at $x = 0.02\ \lambda$ [$v_x\ (x = 0) = 0$ at all times]. When the

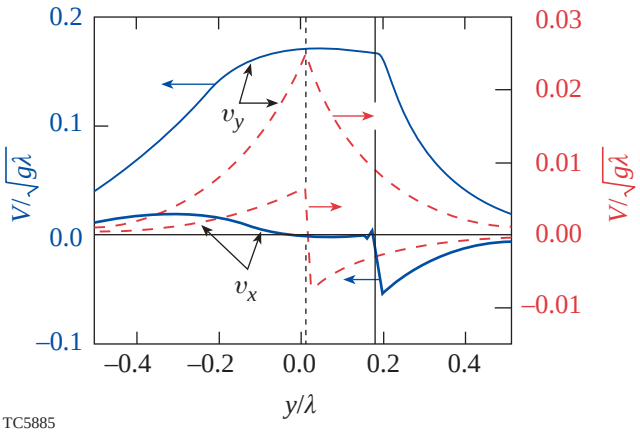

Figure 89.7
Velocity profiles at two different times calculated using results of a 2-D simulation. Dashed lines represent profiles in the linear regime, and solid lines correspond to velocities in the nonlinear regime.

perturbations are in the linear regime ($k\eta_0 << 1$), the velocity decays exponentially from the interface toward the lighter and heavier fluids (dashed lines). As the bubble amplitude becomes nonlinear ($k\eta_0 > 1$), the longitudinal velocity v_y in the light fluid flattens out near the bubble tip and the transverse velocity goes to zero (solid lines), in agreement with the results of Eq. (11).

Applying the model to the Richtmyer–Meshkov (RM) instability, we take the limit of $g \to 0$ in Eq. (8). The asymptotic bubble velocity in this case becomes

$$U_{\mathrm{RM}} \to \frac{3+A_T}{3(1+A_T)}\frac{1}{kt}. \tag{12}$$

In his original paper,[4] Layzer takes only the first harmonic as a solution of the Laplace equation (1). Later, several attempts have been made to construct an exact solution for the case of $A_T = 1$ near the tip of the bubble, writing the solution of Eq. (1) as a Fourier series:[3]

$$\phi = \sum_{l=1}^{\infty} a_l e^{ilkx - lky}. \tag{13}$$

It can be shown,[3] however, that keeping the first two terms in the expansion and applying the boundary conditions up to the fourth order in x leads to an imaginary component in the solution for the asymptotic bubble velocity. To overcome this difficulty, Refs. 3 have suggested keeping the bubble curvature R as a free parameter of the problem, limiting the values of R by the convergence condition of series (13). We propose a different approach to construct an exact solution that is valid near the bubble tip. It can be shown that writing the velocity potential in the form

$$\phi^h = \sum_{l=0}^{\infty} a_{2l+1}\cos\left[(2l+1)kx\right]e^{-(2l+1)k(y-\eta_0)}, \tag{14}$$

$$\phi^l = \sum_{l=0}^{\infty} b_{2l+1}\cos\left[(2l+1)kx\right]e^{(2l+1)k(y-\eta_0)} + b_2 y \tag{15}$$

leads to a real value of bubble velocity in all approximation orders. Such an expansion requires no additional free parameters to provide convergence for the solution. Figure 89.8 shows plots of the first four coefficients a_{1-7} as functions of time for the case of $A_T = 1$. Observe that coefficients a_l decay exponentially with l, satisfying the convergence condition. Next, we calculate asymptotic values of η_2 and U_b using solution (14)–(15). The result is

$$\eta_2(t\to\infty) = -\frac{k}{4.88},\quad U_b(\infty) = 1.025\sqrt{\frac{2A_T}{1+A_T}\frac{g}{3k}}. \tag{16}$$

The convergence of solution (14)–(15) is very fast. Keeping only two terms in each sum in ϕ^h and ϕ^l gives the solution for η_2 and U_b within 99.5% accuracy. Remarkably, the values given in Eq. (16) are in agreement with the results of Ref. 3 (for $A_T = 1$), where the authors introduced a free parameter R. This parameter was chosen at the edge point of the region where the Fourier series (13) converges.

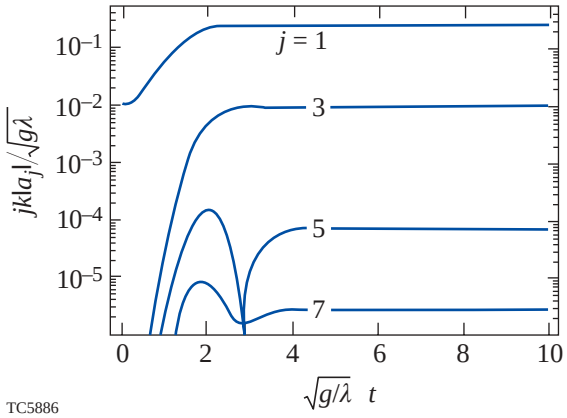

Figure 89.8
Coefficients a_1–a_7 of the Fourier series (14) for $A_T = 1$.

To validate the analysis described above, we compare the results of the model with numerical simulations. Figure 89.9 shows the bubble evolution for the case of $A_T = 0.1$ and $A_T = 0.4$. We start the simulation by imposing a velocity perturbation with amplitude $v_0 = 0.01\sqrt{g\lambda}$. Solid lines represent the solution of Eq. (8); solid dots ($A_T = 0.4$) and solid squares ($A_T = 0.1$) correspond to the results of simulations. Good agreement between theory and simulations confirms the accuracy of the model. Next, we comment on a possibility of applying the Layzer-type analysis to study evolution of the spikes. Reference 8 has shown that such an analysis gives quite a reasonable agreement with simulations for the case of $A_T = 1$. The appropriate velocity potential for the spikes at $A_T < 1$ in the Layzer-type model has the form

$$\phi^h = a_1 \cos(kx) e^{-k(y-\eta_0)} + a_2 y,$$

$$\phi^l = b_1 \cos(kx) e^{k(y-\eta_0)}.$$

Substituting the above expressions into Eqs. (2)–(4) and expanding the latter until the second order in x gives the evolution equations that can be obtained from Eqs. (7) and (8) by substituting $\eta \to -\eta$, $A_T \to -A_T$, and $g \to -g$. Taking the limit of $t \to \infty$, the asymptotic spike velocity becomes

$$U_s = \sqrt{2A_T/(1-A_T)(g/3k)}.$$

The last formula agrees with the prediction of the drag–buoyancy model.[6] Simulations, however, show that the spike velocity for the interfaces with $A_T > 0.1$ does not saturate to a constant value. Figure 89.9 shows the spike amplitudes calculated using the simulation (open circles for $A_T = 0.4$ and open squares for $A_T = 0.1$) and the results of the model (dashed lines). As seen from the results of the simulations, the spike velocity for $A_T > 0.1$ keeps growing linearly in time, even after perturbations become nonlinear. This is caused by the formation of vortices in the proximity of the spike tip. If the Atwood number is not too small, vortices move with the spike, modifying its velocity field and accelerating the spike into the light fluid. Thus, to describe the spike in the nonlinear regime, the velocity potential must be modified to include evolution of the vortices. This is a subject of current research.

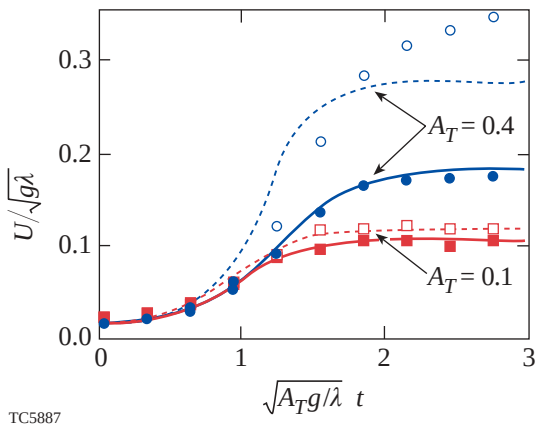

Figure 89.9
Bubble (solid lines, solid circles and squares) and spike (dashed lines, open circles and squares) velocities calculated using the potential model (lines) and numerical simulation (circles and squares).

The procedure described above for the 2-D flow can be applied to analyze the bubble evolution in 3-D geometry. Taking the z axis in the direction of the density gradient and assuming cylindrical symmetry of the bubble, the velocity potential in the heavy and light fluids takes the form $\phi^h = a(t) J_0(kr) e^{-kz}$, $\phi^l = b_1(t) J_0(kr) e^{kz} + b_2(t) z$, where $J_0(x)$ is the Bessel function of zero order. Expanding the velocity potential and the jump conditions across the fluid interface up to the second order in r yields the following system:

$$\eta_2 = -\frac{k}{8} + \left[\frac{k}{8} + \eta_2(0)\right] e^{-2k[\eta_0 - \eta_0(0)]}, \tag{17}$$

$$\ddot{\eta}_0 \frac{k^2 - 4A_T k\eta_2 - 32A_T\eta_2^2}{4(k-8\eta_2)}$$

$$+ \dot{\eta}_0^2 k^2 \frac{(5A_T - 4)k^2 + 16(2A_T - 3)k\eta_2 + 64A_T\eta_2^2}{8(k-8\eta_2)^2}$$

$$+ A_T g \eta_2 = 0. \tag{18}$$

The asymptotic bubble velocity and η_2 derived from the system (17)–(18) take the form

$$\eta_2(t \to \infty) = -k/8,$$

$$U_b^{3\text{-D}}(\infty) = \sqrt{2A_T/(1+A_T)(g/k)}.$$

For the RM case (g = 0), the asymptotic bubble velocity becomes $U_{\text{RM}}^{3\text{-D}} = 2/(1+A_T)/(kt)$. Repeating calculations by keeping higher harmonics in the expansion

$$\phi^h = \sum_{l=0}^{\infty} a_{2l+1} J_0[(2l+1)kr] e^{-(2l+1)kz},$$

$$\phi^l = \sum_{l=0}^{\infty} b_{2l+1} J_0[(2l+1)kr] e^{(2l+1)kz} + b_2 z,$$

the asymptotic bubble velocity converges to

$$U_b^{3\text{-D}} \sim 1.02\sqrt{\frac{2A_T}{1+A_T}\frac{g}{k}}, \quad \eta_2 \to -\frac{k}{6.7}. \tag{19}$$

For A_T = 1, these values are close to the results of Ref. 3, where authors have found the following values: $U_b = 0.99\sqrt{g/k}$ and $\eta_2 = -k/6.4$.

In summary, the nonlinear analytical model of the classical single-mode RT instability at arbitrary Atwood numbers was developed. The model gives a continuous bubble evolution from the exponential growth to the nonlinear regime, where the bubble velocity saturates at

$$U_b^{2\text{-D}} = \sqrt{2A_T/(1+A_T)(g/3k)}$$

and

$$U_b^{3\text{-D}} = \sqrt{2A_T/(1+A_T)(g/k)}.$$

The results of the model agree very well with the numerical simulations and predictions of the drag–buoyancy model.[6]

ACKNOWLEDGMENT

The author thanks Prof. Dov Shvarts and his group, Prof. R. Betti, Prof. J. Sanz, and Dr. C. Cherfils-Clérouin for many helpful discussions. This work was supported by the U.S. Department of Energy Office of Inertial Confinement Fusion under Cooperative Agreement No. DE-FC03-92SF19460, the University of Rochester, and the New York State Energy Research and Development Authority. The support of DOE does not constitute an endorsement by DOE of the views expressed in this article.

REFERENCES

1. Lord Rayleigh, in *Scientific Papers* (Cambridge University Press, Cambridge, England, 1900), Vol. II.
2. B. A. Remington *et al.*, Phys. Plasmas **7**, 1641 (2000); J. D. Lindl, *Inertial Confinement Fusion: The Quest for Ignition and Energy Gain Using Indirect Drive* (Springer-Verlag, New York, 1998).
3. N. A. Inogamov and S. I. Abarzhi, Physica D **87**, 339 (1995); S. I. Abarzhi, Phys. Rev. E **59**, 1729 (1999).
4. D. Layzer, Astrophys. J. **122**, 1 (1955).
5. G. B. Whitham, *Linear and Nonlinear Waves*, Pure and Applied Mathematics (Wiley, New York, 1974), p. 473; J. W. Jacobs and I. Catton, J. Fluid Mech. **187**, 329 (1988); M. J. Dunning and S. W. Haan, Phys. Plasmas **2**, 1669 (1995).
6. D. Oron *et al.*, Phys. Plasmas **8**, 2883 (2001); U. Alon *et al.*, Phys. Rev. Lett. **74**, 534 (1995); G. Dimonte, Phys. Plasmas **7**, 2255 (2000); G. Dimonte and M. Schneider, Phys. Fluids **12**, 304 (2000).
7. K. O. Mikaelian, Phys. Rev. Lett. **80**, 508 (1998).
8. Q. Zhang, Phys. Rev. Lett. **81**, 3391 (1998).
9. S. Wolfram, *The Mathematica Book*, 3rd ed. (Wolfram Media/Cambridge University Press, 1996).

A High-Pass Phase Plate Design for OMEGA and the NIF

Introduction

The direct-drive configuration utilized in inertial confinement fusion (ICF)[1,2] driven by high-powered lasers requires target illumination with a high degree of uniformity, especially in the lower spatial-frequency modes. Nonuniformity in laser irradiation seeds the Rayleigh–Taylor hydrodynamic instability, which consequently degrades target performance.[3–9] Various techniques, such as two-dimensional (2-D) smoothing by spectral dispersion (SSD),[10–13] distributed phase plates (DPP's),[14,15] polarization smoothing (PS),[16–22] and multiple beam overlap, are employed on the OMEGA laser[16,23,24] and will be employed on the National Ignition Facility (NIF) to improve the on-target irradiation uniformity and reduce the laser imprint. The nonuniformity in the lower frequencies (or spherical-harmonic ℓ modes) is particularly dangerous in ICF implosions due to hydrodynamic instabilities that develop during the longer imprinting periods associated with these modes. In addition, these low-order modes are also the most difficult to smooth with the aforementioned methods.

Reduced-autocorrelation phase plates were proposed to reduce the power spectrum of the low-ℓ modes and were designed with discrete phase elements of fixed spatial aperture.[25] These phase plates were calculated by changing selected phase elements in order to minimize the local autocorrelation function of the near-field phase term; hence the name. The reduced-autocorrelation phase plates, calculated by this method, were able to reduce the nonuniformity in the lower-ℓ modes by only a modest average factor of 2 without any near-field phase aberrations. In addition, due to the discrete nature of the phase plate elements, the envelope of the far-field intensity pattern was not controllable (except by changing the shape/size of the discrete phase elements).

The novel and improved design technique presented in this article calculates continuous versions of these specialized phase plates by directly manipulating the power spectrum of the far-field intensity pattern. These new designs are dubbed "high-pass phase plates" to distinguish them from their predecessors and to emphasize the method of directly manipulating the spectrum. The novel phase plate design technique calculates continuous phase plates that produce well-defined far-field intensity envelopes with a high degree of azimuthal symmetry and a controllable power spectrum. The high-pass phase plates are able to reduce the nonuniformity in the lower-ℓ modes by average factors of 4 to 10 (depending on the type of high-pass filter employed) without any near-field phase aberrations. The novel plate design technique presented can also be applied to standard phase plates because it requires no control of the far-field power spectrum. In addition, this technique is computationally efficient, and the calculation speeds are improved by two orders of magnitude over current methods.

The performance of high-pass phase plates is significantly affected by any near-field phase aberrations present on a high-powered ICF laser beam. If the phase aberration is strong enough, the resultant far-field intensity's power spectrum tends toward that produced by a standard continuous phase plate. Simulations of the far-field intensity pattern with applied phase aberrations (either measured or simulated), using the code *Waasikwa'*,[24] shows that the lower-ℓ-mode range can still benefit from these high-pass phase plates. High-pass phase plate designs for both OMEGA and the NIF can realize a reduction of about a factor of $\sqrt{2}$ to 2 in nonuniformity over the lower-ℓ-band range ($11 \le \ell \le 25$) in the presence of typical laser system phase aberrations.

In the following sections, an overview of the novel phase plate design technique will be presented. Next, standard phase plate designs will be compared to high-pass designs for both OMEGA and the NIF. The affect of near-field phase aberrations will then be discussed followed by the improvement realized in the lower-ℓ-band range in the presence of near-field phase aberrations.

A Novel Phase Plate Design Technique

A novel phase plate design technique was developed to calculate continuous phase plates that produce a well-defined far-field intensity envelope with a high degree of azimuthal symmetry and a controllable power spectrum and is incorpo-

rated in a code called *Zhizhoo'*.[26] *Zhizhoo'* can be configured to calculate a continuous near-field phase plate that produces a speckled far-field spot who's envelope matches almost any well-behaved function and has the ability to control the power spectrum of the far-field intensity in order to produce a speckled pattern with reduced nonuniformity in the low-order modes. A phase plate that reduces the nonuniformity in the low-order modes is referred to as a high-pass phase plate. The technique is computationally efficient and can complete a calculation in 10 to 20 min running on an SGI Origin 2000 machine with eight parallel processors.

The goal of the novel phase plate design technique is to produce a diffractive phase optic that varies slowly across the whole beam aperture and possesses no sharp discontinuities or phase anomalies. Simulated annealing is the current technique used at LLE to calculate continuous phase plates, but it tends to be computationally inefficient and takes tens of hours to complete a calculation.[14,15] The novel phase plate design technique wraps an additional iterative process around a standard phase-retrieval technique that is able to control the spatial and spectral properties of the speckled far-field intensity pattern while calculating a continuous phase plate. Two user-supplied design functions drive the algorithms to produce the required phase plate: the near-field beam intensity $\left|E_0\left(x_{\mathrm{nf}}, y_{\mathrm{nf}}\right)\right|^2$ and the far-field intensity envelope target $I_{\mathrm{ff_{target}}}\left(x_{\mathrm{ff}}, y_{\mathrm{ff}}\right)$, where $\left(x_{\mathrm{nf}}, y_{\mathrm{nf}}\right)$ and $\left(x_{\mathrm{ff}}, y_{\mathrm{ff}}\right)$ are the near-field and far-field coordinate systems, respectively.

1. Standard Phase-Retrieval Technique

The core or central algorithm of the novel phase plate design technique presented here is based on a standard phase-retrieval technique known as the error-reduction scheme; the error is guaranteed to never increase after every iteration.[27,28] The standard phase-retrieval algorithm employs the property of Fourier optics that connects the complex near- and far-field quantities via the Fourier transform,[29] where the far field is at the focal plane of the final lens in the long laser chain in OMEGA and the NIF, viz.,

$$\tilde{E}\left(x_{\mathrm{ff}}, y_{\mathrm{ff}}\right) = \iint E\left(x_{\mathrm{nf}}, y_{\mathrm{nf}}\right) \exp\left\{-i\frac{2\pi}{\lambda_{\mathrm{UV}} f}\left[x_{\mathrm{ff}} x_{\mathrm{nf}} + y_{\mathrm{ff}} y_{\mathrm{nf}}\right]\right\} dx_{\mathrm{nf}}\, dy_{\mathrm{nf}} = \Im\left\{E\left(x_{\mathrm{nf}}, y_{\mathrm{nf}}\right)\right\}, \tag{1}$$

$$E\left(x_{\mathrm{nf}}, y_{\mathrm{nf}}\right) = \frac{1}{\left(\lambda_{\mathrm{UV}} f\right)} \iint \tilde{E}\left(x_{\mathrm{ff}}, y_{\mathrm{ff}}\right) \exp\left\{+i\frac{2\pi}{\lambda_{\mathrm{UV}} f}\left[x_{\mathrm{ff}} x_{\mathrm{nf}} + y_{\mathrm{ff}} y_{\mathrm{nf}}\right]\right\} dx_{\mathrm{ff}}\, dy_{\mathrm{ff}} = \Im^{-1}\left\{\tilde{E}\left(x_{\mathrm{ff}}, y_{\mathrm{ff}}\right)\right\}, \tag{2}$$

where λ_{UV} = 351 nm is the UV laser wavelength, f is the focal length of the final focusing lens (f = 1.8 m for OMEGA and f = 7.7 m for the NIF), and operators $\Im\{.\}$ and $\Im^{-1}\{.\}$ define the 2-D spatial Fourier transform and its inverse, respectively, that map the complex-valued electric field from the near-field coordinates $\left(x_{\mathrm{nf}}, y_{\mathrm{nf}}\right)$ to the far-field coordinates $\left(x_{\mathrm{ff}}, y_{\mathrm{ff}}\right)$ and vice versa. The magnitudes of the near-field or input beam shape

$$E_0\left(x_{\mathrm{nf}}, y_{\mathrm{nf}}\right) = \left|E\left(x_{\mathrm{nf}}, y_{\mathrm{nf}}\right)\right| \tag{3}$$

and the speckled far-field objective pattern

$$\tilde{E}_0\left(x_{\mathrm{ff}}, y_{\mathrm{ff}}\right) = \left|\tilde{E}\left(x_{\mathrm{ff}}, y_{\mathrm{ff}}\right)\right| \tag{4}$$

are known *a priori* before the iterative procedure is initiated. During the iterative procedure, the known input beam shape replaces the calculated amplitude of the near field and the far-field objective pattern replaces the calculated amplitude of the far field, while the calculated phase of both complex fields is retained.[28] A diagram of this iterative procedure is illustrated in Fig. 89.10. This algorithm converges quickly and accurately to almost any desirable far-field envelope; the main restrictions are that the envelope be square integrable and possess no sharp discontinuities, i.e., a well-behaved function.[31] The phase calculated during this standard technique is bounded by $\pm\pi$ due to the inherent range of the *arctangent* function used to calculate the phase based on the real and imaginary parts of the complex field quantities.

Bounding the phase in this manner results in many sharp 2π-phase discontinuities that theoretically will not scatter energy; however, a realistic device will scatter energy out of the desired far-field envelope because this boundary is not exactly reproduced due to limitations in the manufacturing process.[32] The

standard phase-retrieval technique can also produce phase anomalies that have sharp π-phase discontinuities (accurately referred to as phase dislocations[33] or phase vortices and imprecisely called phase poles or spiral phase singularities), which scatter additional light when they are illuminated (because a field value of zero is expected at phase dislocations) and are not due to a manufacturing limitation, although manufacturing limitations can exacerbate the scatter. A π-phase discontinuity occurs independently of the direction that the phase dislocation is traversed,[31] and a total of 2π phase is accumulated on a line integral path encircling a phase dislocation of order 1.[34] Both of these scattering sources limit the usefulness of the standard phase technique.

The sharp 2π-phase discontinuities can be removed by a number of different phase-unwrapping algorithms.[35] The phase anomalies pose a much more insidious problem because not only do they inhibit many phase-unwrapping algorithms, they also are one of the main reasons that the standard phase-retrieval technique stagnates or fails to converge.[36] If one attempts to artificially remove the phase discontinuities, they will simply reappear later in another location during the standard phase retrieval's iteration process.[31] Using the standard phase-retrieval technique alone renders the phase dislocations irremovable.

The number of phase anomalies can be reduced by initializing the standard phase technique with distributions that do not inherently contain phase anomalies[34] (which can frequently occur in random distributions); however, some problems benefit equally as well from a random distribution.[36] Another method attempts to remove pairs of phase dislocations by smoothing over the region containing them and then restricting the degree of freedom in that region during further iterations. This method, however, results in a rather tedious and complicated algorithm that requires searching for and identifying pairs of phase dislocations that may not even reside on the current computational grid.[34]

Phase dislocations are associated with zeros of complex functions.[37–42] If a phase dislocation exists, a complex zero exists (although the opposite is not necessarily true). One source of phase dislocations in the near field is hard clipping or aggressive attenuation of the spatial spectrum (or far field).[31] If a near-field object's spectrum extends beyond the computational domain of the far field or extends into a region where the far-field target is zero, hard clipping can occur. Alternatively, aggressive attenuation of the spatial frequencies can occur during the application of the far-field constraints, i.e., applying a far-field target function that falls rapidly toward zero in regions where the near-field object's spectrum has significant values. Both of these mechanisms can occur when the near-field phase possesses large gradients, which will introduce complex zeros into the near field during the phase-retrieval procedure. It can also be shown, however, that if a near-field object has a spectrum with compact or finite support (i.e., a band-limited function), a near-field phase without phase dislocations can be found.[31]

2. Initial Guess and Construction of the Far-Field Objective

Both the standard phase retrieval and novel phase plate design techniques require an initial guess of the near-field phase. Through a judicious choice, the algorithms can be given a jump-start on convergence that helps prevent stagnation (as mentioned in the previous section). A random initial guess whose values take on any phase in the interval $0 \le \phi \le 2\pi$ can be a useful generic starting point for many applications where phase dislocations are not that much of a concern. This random pattern, however, is not a prudent starting point for continuous phase plate designs.

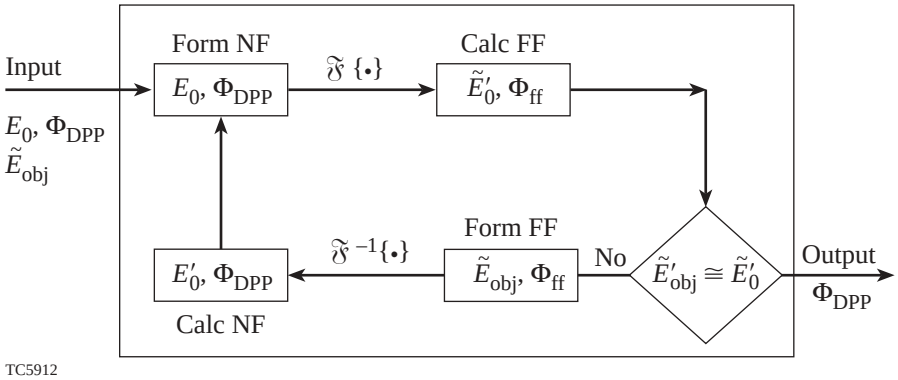

Figure 89.10
A flow diagram depicting the iterative process employed in the standard phase-retrieval technique. The idea behind this technique has a long history dating back to Wolf[30] in 1962. Gerchberg, Saxton, and Fienup extended this idea to two dimensions, and the basic error-reduction scheme is shown in this figure.[27,28] This iterative technique is at the core of the novel phase plate design technique.

The best choice for a continuous phase plate design is one whose phase is already continuous and produces a far-field pattern that adequately covers the targeted region. A scaled, colored-noise (see Carslon,[41] pp. 153–154) phase pattern is suitable for this purpose and is given by a Fourier filter operation:

$$\hat{\Phi}_{\mathrm{DPP}}(x_{\mathrm{nf}},y_{\mathrm{nf}}) = a\cdot\Re\left\{\Im^{-1}\left\{\Im\left\{\zeta(x_{\mathrm{nf}},y_{\mathrm{nf}})\right\}\right.\right.$$

$$\left.\left.\exp\left[-\ln(2)\cdot\left(\frac{k_{\mathrm{nf}}}{k_{0_{\mathrm{DPP}}}}\right)^{20}\right]\right\}\right\}, \qquad (5)$$

where a is the scaling constant, $\zeta(x_{\mathrm{nf}},y_{\mathrm{nf}})\in[-1,1]$ is a random number field, $k_{\mathrm{nf}}\equiv\left(k_{x_{\mathrm{nf}}}^2+k_{y_{\mathrm{nf}}}^2\right)^{1/2}$ is the radial wave number of the near-field coordinate system, $k_{0_{\mathrm{DPP}}}=360$ rad/m is the FWHM filter point, and $\Re\{\cdot\}$ is the real operator. When the color-noise phase pattern, given by Eq. (5), is used, the resultant far-field speckle pattern possesses a simple Gaussian envelope. The scaling constant a is used to effectively spread out the resultant far-field speckle pattern to cover the targeted area (the value used in this article is a = 50 rad for both OMEGA and the NIF). It is important for the constant a to be large enough to encompass the targeted area of the far field but not so large that it extends beyond the computational region of the far field (otherwise, aliasing effects can play havoc on the algorithm).

Once the initial phase $\hat{\Phi}_{\mathrm{DPP}}(x_{\mathrm{nf}},y_{\mathrm{nf}})$ is chosen, manipulating the initial speckled far-field pattern produced by the initial phase generates the first far-field objective pattern. The initial speckled far-field pattern is given by

$$\hat{\tilde{E}}_0(x_{\mathrm{ff}},y_{\mathrm{ff}}) = \left|\Im\left\{E_0(x_{\mathrm{nf}},y_{\mathrm{nf}})\cdot\exp\left\{i\hat{\Phi}_{\mathrm{DPP}}(x_{\mathrm{nf}},y_{\mathrm{nf}})\right\}\right\}\right|. \qquad (6)$$

First, the envelope of the initial speckled far-field intensity pattern is found by using an optimal filter technique (described in detail in the following section):

$$I_{\mathrm{ff}_{\mathrm{env}}}(x_{\mathrm{ff}},y_{\mathrm{ff}}) = \Re\left\{\Im^{-1}\left\{\tilde{\Psi}_{\mathrm{opt}}(k_{x_{\mathrm{ff}}},k_{y_{\mathrm{ff}}})\right.\right.$$

$$\left.\left.\Im\left\{\left|\hat{\tilde{E}}_0(x_{\mathrm{ff}},y_{\mathrm{ff}})\right|^2\right\}\right\}\right\}, \qquad (7)$$

where $\tilde{\Psi}_{\mathrm{opt}}(k_{x_{\mathrm{ff}}},k_{y_{\mathrm{ff}}})$ is the optimal filter. Next a transformation function $\Lambda(x_{\mathrm{ff}},y_{\mathrm{ff}})$ is defined as

$$\Lambda(x_{\mathrm{ff}},y_{\mathrm{ff}}) \equiv \begin{cases} \left[\dfrac{I_{\mathrm{ff}_{\mathrm{target}}}(x_{\mathrm{ff}},y_{\mathrm{ff}})}{I_{\mathrm{ff}_{\mathrm{env}}}(x_{\mathrm{ff}},y_{\mathrm{ff}})}\right]^{1/2} & ;\quad I_{\mathrm{ff}_{\mathrm{env}}}(x_{\mathrm{ff}},y_{\mathrm{ff}})\neq 0 \\ 0 & ;\quad \text{otherwise} \end{cases}, \qquad (8)$$

where $I_{\mathrm{ff}_{\mathrm{target}}}(x_{\mathrm{ff}},y_{\mathrm{ff}})$ is the far-field target intensity envelope. The function $\Lambda(x_{\mathrm{ff}},y_{\mathrm{ff}})$ transforms the initial far-field pattern as

$$\tilde{E}_{\mathrm{obj}}(x_{\mathrm{ff}},y_{\mathrm{ff}}) = \Lambda(x_{\mathrm{ff}},y_{\mathrm{ff}})\cdot\hat{\tilde{E}}_0(x_{\mathrm{ff}},y_{\mathrm{ff}}), \qquad (9)$$

where $\tilde{E}_{\mathrm{obj}}(x_{\mathrm{ff}},y_{\mathrm{ff}})$ yields the first speckled far-field objective based on the initial far-field pattern $\hat{\tilde{E}}_0(x_{\mathrm{ff}},y_{\mathrm{ff}})$. The importance of Eq. (9) is both subtle and critical to the convergence to a continuous phase plate; the initial phase $\hat{\Phi}_{\mathrm{DPP}}(x_{\mathrm{nf}},y_{\mathrm{nf}})$ is correlated to the generated speckle pattern. If this correlation is not maintained, convergence can be lost and the resultant phase pattern tends to produce a speckled far field with a Gaussian-shaped envelope and, under extreme cases, a high central peak develops. The transformation function $\Lambda(x_{\mathrm{ff}},y_{\mathrm{ff}})$ may contain anomalously high values where $I_{\mathrm{ff}_{\mathrm{env}}}(x_{\mathrm{ff}},y_{\mathrm{ff}})\sim 0$. These values are eventually suppressed during the enhancement procedure described in the next section.

3. Wrapper Algorithm: Phase Continuity and Convergence Enhancement

The continuity of the calculated phase is controlled using a two-step process: a 2-D phase-unwrapping procedure is applied to the phase map, calculated using the standard phase-retrieval method, followed by a low-pass filter that removes any residual high frequencies. The 2-D phase-unwrapping problem can be expressed in the form of Poisson's equation. The 2-D phase-unwrapping algorithm implemented in *Zhizhoo'* directly solves Poisson's equation on the whole computational grid using cosine transforms and does not need to painstakingly iterate around the grid as in other methods.[35] The cosine transform technique acts globally on the phase function and therefore is relatively immune to any local phase anomalies in that it tends to smooth over discontinuities, which is a highly desirable feature in the design of continuous phase plates.

Initially, when there are a number of phase anomalies, some residual high-frequency artifacts that remain after the 2-D phase-unwrapping operation need to be additionally smoothed. A simple, smooth, low-pass filter is used to remove the high-frequency artifacts, where the filter is a super-Gaussian:

$$\tilde{\Psi}_{\Phi}\left(k_{x_{\mathrm{nf}}},k_{y_{\mathrm{nf}}}\right)=\exp\left\{-\ln(2)\left(\frac{k_{\mathrm{nf}}}{k_{0_{\mathrm{DPP}}}}\right)^{20}\right\}, \tag{10}$$

where $k_{0_{\mathrm{DPP}}}=1270\ \mathrm{rad/m}$ is the FWHM filter point. Note that the filtering function used here is the same as that implemented in the initial guess of the phase except that the quantity $k_{0_{\mathrm{DPP}}}$ is larger. The filtering is implemented as

$$\Phi_{\mathrm{DPP}}\left(x_{\mathrm{nf}},y_{\mathrm{nf}}\right)=\Re\left\{\Im^{-1}\left\{\tilde{\Psi}_{\Phi}\left(k_{x_{\mathrm{nf}}},k_{y_{\mathrm{nf}}}\right)\Im\left\{\Phi'_{\mathrm{DPP}}\left(x_{\mathrm{nf}},y_{\mathrm{nf}}\right)\right\}\right\}\right\}, \tag{11}$$

where $\Phi'_{\mathrm{DPP}}\left(x_{\mathrm{nf}},y_{\mathrm{nf}}\right)$ is the unwrapped phase, $\Re\{\cdot\}$ is the real operator, and the coordinate transformations $k_{x_{\mathrm{nf}}}=2\pi x_{\mathrm{ff}}/\left(\lambda_{\mathrm{UV}}f\right)$ and $k_{y_{\mathrm{nf}}}=2\pi y_{\mathrm{ff}}/\left(\lambda_{\mathrm{UV}}f\right)$ are required to use the definitions in Eqs. (1) and (2).

The speckled far field must be recalculated to account for any changes that occur due to the updated phase plate $\Phi_{\mathrm{DPP}}\left(x_{\mathrm{nf}},y_{\mathrm{nf}}\right)$ after continuity is corrected by the unwrapping and filtering process. This speckled far field becomes the current speckled far-field objective and is represented as $\tilde{E}'_{\mathrm{obj}}\left(x_{\mathrm{ff}},y_{\mathrm{ff}}\right)$. At first, the resultant unwrapped and filtered phase mapping does not produce a speckled far-field pattern whose envelope matches the target envelope. The whole procedure is then repeated until the continuous phase mapping converges and produces the targeted far-field envelope or reaches a fixed number of iterations. A flow diagram of the complete *Zhizhoo'* design process including the standard phase-retrieval technique is illustrated in Fig. 89.11.

An additional feature is also implemented to encourage fast and accurate convergence before the whole wrapper algorithm is repeated; the far-field target objective is "enhanced" or "emphasized" to compensate for any shortcomings of the current phase mapping, i.e., any azimuthal asymmetries or spurious peaks and valleys in the current far-field intensity envelope are corrected by modifying the 2-D far-field objective to dampen the peak-to-valley variation. This idea is similar to the input/output algorithm described by Fienup.[28] The emphasis is a critical step in the algorithm because it maintains the correlation between the current phase plate and the speckle pattern that it generates. Without this step the algorithm would diverge.

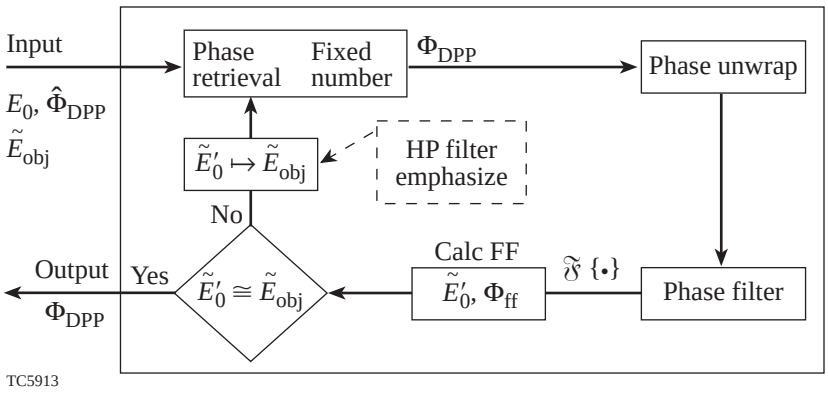

Figure 89.11
A flow diagram depicting the iterative process employed in the novel phase plate design technique and used in the code *Zhizhoo'*. Initialized near-field phase and far-field objective functions are fed into the iterative process. The standard phase-retrieval block (see Fig. 89.10) is executed first, followed by the 2-D phase unwrap and phase filter. Next, the speckled far field $\tilde{E}'_{\mathrm{obj}}\left(x_{\mathrm{ff}},y_{\mathrm{ff}}\right)$ is recalculated based on the latest unwrapped and filtered phase plate. Finally, the updated far field $\tilde{E}'_{\mathrm{obj}}\left(x_{\mathrm{ff}},y_{\mathrm{ff}}\right)$ is compared to the far-field objective $\tilde{E}_{\mathrm{obj}}\left(x_{\mathrm{ff}},y_{\mathrm{ff}}\right)$ to test for convergence and maximum number of iterations reached to determine whether or not to proceed. If proceeding, then the far-field objective functions are modified to maintain correlation with the latest iteration of the near-field phase. The modifications include a convergence enhancement, which is applied to the far-field objective. The second optional modification alters the far-field objective's power spectrum by high-pass filtering before continuing back into the standard phase-retrieval block. The dashed box denotes optional blocks.

The emphasis function requires the envelope of the far-field intensity to make these corrections. The far-field envelope is calculated using either a low-pass or an optimal filter technique.[42] The low-pass method uses a super-Gaussian filter

$$\tilde{\Psi}_{\mathrm{ff}}\left(k_{x_{\mathrm{ff}}},k_{y_{\mathrm{ff}}}\right)=\exp\left\{-\ln(2)\left(\frac{k_{\mathrm{ff}}}{2k_{\mathrm{env}}}\right)^{10}\right\}, \qquad (12)$$

where $k_{\mathrm{ff}}\equiv\left(k_{x_{\mathrm{ff}}}^2+k_{y_{\mathrm{ff}}}^2\right)^{1/2}$ is the radial wave number of the far-field coordinate system and k_{env} defines the approximate frequency where the envelope power spectrum and the speckle spectrum intersect ($k_{\mathrm{env}}=43.2\times10^3$ rad/m for OMEGA and $k_{\mathrm{env}}=5.88\times10^3$ rad/m for the NIF). The optimal filter uses the far-field power spectrum and a model of the power spectrum of the speckle:

$$\tilde{\Psi}_{\mathrm{opt}}\left(k_{x_{\mathrm{ff}}},k_{y_{\mathrm{ff}}}\right)=\frac{\left|\tilde{I}_{\mathrm{ff}}\left(k_{x_{\mathrm{ff}}},k_{y_{\mathrm{ff}}}\right)\right|^2-\Xi\left(k_{x_{\mathrm{ff}}},k_{y_{\mathrm{ff}}}\right)}{\left|\tilde{I}_{\mathrm{ff}}\left(k_{x_{\mathrm{ff}}},k_{y_{\mathrm{ff}}}\right)\right|^2}, \qquad (13)$$

where $\left|\tilde{I}_{\mathrm{ff}}\left(k_{x_{\mathrm{ff}}},k_{y_{\mathrm{ff}}}\right)\right|^2$ defines the power spectrum of the far-field intensity and $\Xi\left(k_{x_{\mathrm{ff}}},k_{y_{\mathrm{ff}}}\right)$ represents the power spectrum of the speckle intensity, which is given by the autocorrelation of the near-field intensity.[43] The optimal filter is the best method of obtaining the envelope; however, it is not compatible with the design of the high-pass phase plate because a model for the far-field power spectrum is not known for this case *a priori*. The far-field intensity envelope $I_{\mathrm{ff_{env}}}\left(x_{\mathrm{ff}},y_{\mathrm{ff}}\right)$ is calculated by applying a Fourier-filtering technique similar to Eq. (7) to the far-field intensity $I_{\mathrm{ff}}\left(x_{\mathrm{ff}},y_{\mathrm{ff}}\right)$ while using one of the filters in Eq. (12) or (13). The emphasis function may now be calculated as

$$\Lambda_{\mathrm{emp}}\left(x_{\mathrm{ff}},y_{\mathrm{ff}}\right)=\alpha\cdot\Lambda\left(x_{\mathrm{ff}},y_{\mathrm{ff}}\right), \qquad (14)$$

where $\Lambda\left(x_{\mathrm{ff}},y_{\mathrm{ff}}\right)$ is defined in Eq. (8) and α is an enhancement factor that can be used to hasten convergence by overcompensating for the distortions in the envelope function and is defined as

$$\alpha=\begin{cases}\alpha_{>1}; & \Lambda\left(x_{\mathrm{ff}},y_{\mathrm{ff}}\right)>1\\ 1\ ; & \Lambda\left(x_{\mathrm{ff}},y_{\mathrm{ff}}\right)=1\\ \alpha_{<1}; & \Lambda\left(x_{\mathrm{ff}},y_{\mathrm{ff}}\right)<1\end{cases}. \qquad (15)$$

Care must be taken in selecting the constants $\alpha_{>1}$ and $\alpha_{<1}$ because amplifying oscillations may occur that lead to loss of control and convergence failure. The values found to yield adequate convergence that avoids oscillations are $\alpha_{>1}=1.1$ and $\alpha_{<1}=0.9$. The emphasis function $\Lambda_{\mathrm{emp}}\left(x_{\mathrm{ff}},y_{\mathrm{ff}}\right)$ modifies the current far-field objective before the next trial of the standard phase-retrieval technique as

$$\tilde{E}_{\mathrm{obj}}\left(x_{\mathrm{ff}},y_{\mathrm{ff}}\right)=\Lambda_{\mathrm{emp}}\left(x_{\mathrm{ff}},y_{\mathrm{ff}}\right)\cdot\tilde{E}'_{\mathrm{obj}}\left(x_{\mathrm{ff}},y_{\mathrm{ff}}\right), \qquad (16)$$

where $\tilde{E}'_{\mathrm{obj}}\left(x_{\mathrm{ff}},y_{\mathrm{ff}}\right)$ represents the current objective and $\tilde{E}_{\mathrm{obj}}\left(x_{\mathrm{ff}},y_{\mathrm{ff}}\right)$ represents the new trial. Eventually the emphasis function decays toward unity as the continuous phase mapping converges; therefore the emphasis function is similar to a merit function. The emphasis function is 2-D, which enables *Zhizhoo'* to compensate for any azimuthal asymmetries or other distortions in the far-field intensity envelope.

The number of iterations or sets of the wrapper algorithm that are executed in *Zhizhoo'* may end when either a convergence criterion is reached or a maximum number of sets has occurred. The convergence criterion used in *Zhizhoo'* is a simple rms error of the calculated far field relative to the design specification, viz.

$$\sigma_{\mathrm{ff}}=\left\{\frac{\iint\limits_{\forall\mathrm{space}}\left[\tilde{E}'_{\mathrm{obj}}\left(x_{\mathrm{ff}},y_{\mathrm{ff}}\right)-\tilde{E}_{\mathrm{obj}}\left(x_{\mathrm{ff}},y_{\mathrm{ff}}\right)\right]^2dx_{\mathrm{ff}}dy_{\mathrm{ff}}}{\iint\limits_{\forall\mathrm{space}}\left[\tilde{E}_{\mathrm{obj}}\left(x_{\mathrm{ff}},y_{\mathrm{ff}}\right)\right]^2dx_{\mathrm{ff}}dy_{\mathrm{ff}}}\right\}^{1/2}, \qquad (17)$$

where $\tilde{E}'_{\mathrm{obj}}\left(x_{\mathrm{ff}},y_{\mathrm{ff}}\right)$ represents the objective produced by the current realization of the phase plate and $\tilde{E}_{\mathrm{obj}}\left(x_{\mathrm{ff}},y_{\mathrm{ff}}\right)$ represents the objective prior to the emphasis function modifications. At the completion of all the sets, the calculated continuous phase plate produces a speckled far-field intensity pattern whose envelope matches the objective function extremely well without any azimuthal asymmetries or distortions. In addition, the phase discontinuities or complex zeros of the near field are removed.

4. High-Pass Phase Plate

The ability to control the far-field intensity's power spectrum and produce a high-pass phase plate is merely an extension to the novel phase plate design technique; a step, which is

added to the algorithm, revises the power spectrum of the far-field objective during the iterative process. This step becomes part of the wrapper algorithm, as indicated in Fig. 89.11, and modifies the far-field objective by high-pass filtering its power spectrum. The high-pass filtering must be done as part of the wrapper algorithm because it is necessary to maintain the correlation between the speckle pattern produced by the current phase plate (i.e., after the 2-D phase unwrapping and filtering process) just as in the application of the emphasis function. The current implementation applies the high-pass filtering before the emphasis function modifications. As the continuous-phase mapping converges, it will produce a far-field intensity envelope that matches the targeted objective as well as produce speckle with dramatically reduced power in the lower-ℓ modes. The amount of power that can be removed depends on the type of filter used. A sharp-cutoff, wideband filter can achieve about a factor-of-10 reduction in the power spectrum across the whole requested band, whereas a slowly varying filter envelope can realize as much as a factor-of-100 reduction in the lowest-ℓ modes.

After 2-D phase unwrapping and filtering, the current phase-plate realization yields an intensity speckle field $\left|E'_{\text{obj}}(x_{\text{ff}}, y_{\text{ff}})\right|^2$ comprised of a unity-mean, uniformly random speckle field, which is modulated by the far-field envelope. The far-field envelope must be removed so that the high-pass filter does not affect the targeted envelope but primarily so that the high-pass filter operates directly on the random speckle field. Separating the unity mean from the uniformly random speckle field and modulating its sum by the envelope function, constructs a model for this speckle field:

$$\left|E'_{\text{obj}}(x_{\text{ff}}, y_{\text{ff}})\right|^2 = I_{\text{ff}_{\text{env}}}(x_{\text{ff}}, y_{\text{ff}})\left[1 + \text{spec}'(x_{\text{ff}}, y_{\text{ff}})\right], \quad (18)$$

where $I_{\text{ff}_{\text{env}}}(x_{\text{ff}}, y_{\text{ff}})$ is the slowly varying envelope function obtained by low-pass filtering the speckle field and $\text{spec}'(x_{\text{ff}}, y_{\text{ff}})$ is a zero-mean speckle field. The low-pass filter used to calculate $I_{\text{ff}_{\text{env}}}(x_{\text{ff}}, y_{\text{ff}})$, for this case, is given by Eq. (12) except with a super-Gaussian of order 5. The high-pass filter operates on the zero-mean speckle field $\text{spec}'(x_{\text{ff}}, y_{\text{ff}})$.

Let $E'_{\text{obj}}(x_{\text{ff}}, y_{\text{ff}})$ be the far-field objective function produced by the current realization of the phase plate after 2-D phase unwrapping and filtering, which is fed into the speckle model to yield the current zero-mean speckle field $\text{spec}'(x_{\text{ff}}, y_{\text{ff}})$. The high-pass-filtered speckle is then given by

$$\text{spec}(x_{\text{ff}}, y_{\text{ff}}) = \Re\left\{\Im^{-1}\left\{\Psi_{\text{HP}}(k_{x_{\text{ff}}}, k_{y_{\text{ff}}}) \cdot \Im\left\{\text{spec}'(x_{\text{ff}}, y_{\text{ff}})\right\}\right\}\right\}, \quad (19)$$

where $\Psi_{\text{HP}}(k_{x_{\text{ff}}}, k_{y_{\text{ff}}})$ represents any type of high-pass filter. In this article, the sharp-cutoff filter is given by

$$\Psi_{\text{HP}}(k_{x_{\text{ff}}}, k_{y_{\text{ff}}}) = \begin{cases} 1; & k_{\text{ff}} > 200/r_{\text{fuel}} \\ 0; & k_{\text{ff}} \le 200/r_{\text{fuel}} \end{cases}, \quad (20)$$

or the slowly varying filter is given by

$$\Psi_{\text{HP}}(k_{x_{\text{ff}}}, k_{y_{\text{ff}}}) = \exp\left\{-\ln(2)\left(\frac{r_{\text{fuel}} k_{\text{ff}}}{200}\right)^{2.25}\right\}, \quad (21)$$

where r_{fuel} = 500 μm is the fuel pellet radius for OMEGA. After high-pass filtering, the zero-mean speckle field is then substituted back into the speckle model to form the new far-field objective $E_{\text{obj}}(x_{\text{ff}}, y_{\text{ff}})$, viz.,

$$E_{\text{obj}}(x_{\text{ff}}, y_{\text{ff}}) = \left\{I_{\text{ff}_{\text{env}}}(x_{\text{ff}}, y_{\text{ff}})\left[1 + \text{spec}(x_{\text{ff}}, y_{\text{ff}})\right]\right\}^{0.5}. \quad (22)$$

The new far-field objective $E_{\text{obj}}(x_{\text{ff}}, y_{\text{ff}})$ would then be modified further by the emphasis function as described in the previous section.

Phase Plate Design Results

Two types of continuous phase plates were designed using *Zhizhoo'* for each laser: OMEGA and the NIF. The first type of phase plate is referred to as a standard phase plate to distinguish it from the second type, a high-pass phase plate. The standard phase plate is used as the basis of comparison to measure the ability of the high-pass phase plate to reduce the power in the lower-ℓ modes.

1. OMEGA Phase Plate Designs

The targeted far-field intensity envelope for the first OMEGA phase plate design is a super-Gaussian of order 8 (sg = 8) and an intensity-full-width-at-half-maximum (IFWHM) radius of r_0 = 432 μm:

$$I_{\mathrm{ff_{target}}}\left(x_{\mathrm{ff}}, y_{\mathrm{ff}}\right) = \exp\left\{-\ln(2)\left(\frac{r_{\mathrm{ff}}}{r_0}\right)^{\mathrm{sg}}\right\}, \quad (23)$$

where $r_{\mathrm{ff}} \equiv \left(x_{\mathrm{ff}}^2 + y_{\mathrm{ff}}^2\right)^{1/2}$ is the radius in the far-field coordinate system. This far-field intensity envelope target defines a 95% enclosed energy contour with a diameter of D_{95} = 925 μm and was chosen to demonstrate the ability of *Zhizhoo'* to produce a far-field envelope of high super-Gaussian order. The near-field clear aperture is round and has a diameter of 27.5 cm. The simulation space for the near field was a 1024 × 1024 grid spanning 55.0 cm, and the corresponding far field covered 1.18 mm on a 1024 × 1024 grid.

Zhizhoo' was run with these design parameters to calculate a continuous standard phase plate with a continuous random initial guess for the phase, which was filtered with a super-Gaussian filter of order 20 and filter cutoff parameter $k_{0_{\mathrm{DPP}}} = 360$ rad/m. The internal standard phase-retrieval code was set to run five iterations, the wrapper algorithm was set at a fixed number of 50 iterations, and emphasis was enabled. *Zhizhoo'* ran in parallel on eight processors on the SGI Origin 2000 for 15 min, which ended with a rms far-field error of σ_{ff} = 5.8%. A plot of the azimuthally averaged far-field intensity is compared to the far-field target envelope in Fig. 89.12. The agreement between the resultant far field and the target far-field envelope is excellent even for this high-order super-Gaussian. This level of agreement is achieved mainly due to the combined capabilities of the emphasis function and continuity control to keep the standard phase-retrieval method from stagnating; the error-reduction algorithm is guaranteed to never increase the error upon every iteration, and, if stagnation can be controlled, the calculated phase will converge to the correct answer with no complex zeros in the near field, i.e., no phase dislocations. These results should be compared to the relatively poor results achieved in Refs. 15, 32, and 44. The novel phase plate design technique is also able to control any azimuthal asymmetries of the far field through the application of a 2-D emphasis function. This is illustrated in Fig. 89.13 by plotting the far-field intensity contours that result from applying 1-THz, 2-D SSD and PS in the asymptotic limit.[23,24]

Zhizhoo' was then run to design both a continuous standard and high-pass phase plate with a super-Gaussian far-field target of order 3 (sg = 3) and an IFWHM radius of r_0 = 325 μm, which defines a 95% enclosed energy contour with a diameter of D_{95} = 970 μm. This super-Gaussian envelope is chosen since it produces ample uniformity on the spherical OMEGA target. The high-pass function used was a wideband, sharp filter that attempted to attenuate all modes $0 < \ell \leq 200$ and pass all others. *Zhizhoo'* completed the high-pass design in parallel in 20 min

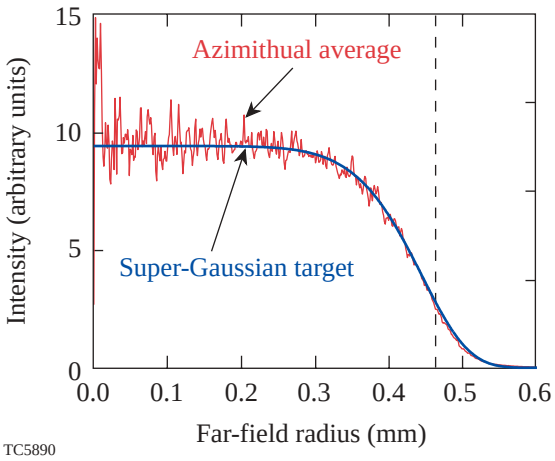

Figure 89.12
The azimuthally averaged far-field intensity (red line) is plotted against the far-field target envelope (blue line). The far-field target envelope has design parameters sg = 8 and r_0 = 432 μm. The red line is very noisy near the origin due to the limited number of points that were available to average. The dashed vertical line indicates the 95% enclosed energy contour, which is at r = 463 μm. 2-D SSD, PS, and phase aberrations are not applied.

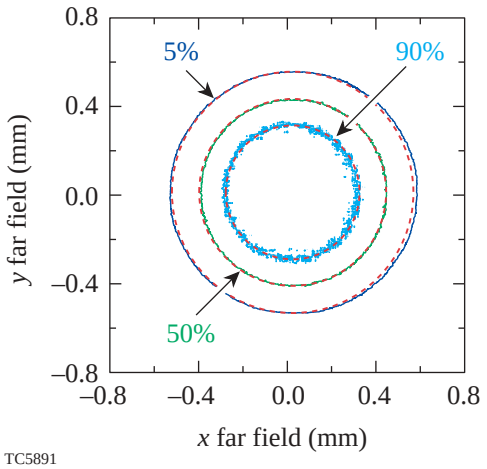

Figure 89.13
The plotted contours correspond to the 5%, 50%, and 90% of the envelope peak of the far-field intensity that result from applying 2-D SSD and PS in the asymptotic limit. The corresponding contours for the target envelope are plotted as dashed lines. The solid contours show excellent agreement to the target with very little azimuthal asymmetry. Phase aberrations have not been applied.

(it takes longer than the standard phase plate because of the additional filtering calculations) using the same fixed number of iterations as before, which ended with a rms far-field error of σ_{ff} = 5.5%; the standard phase plate design completed with σ_{ff} = 2.8%. The resultant far-field envelopes match the target function very well. The larger σ_{ff} parameter for the high-pass phase plate is due to the inability of the phase plate to reproduce the exact filtered speckle, even though the envelope is very close to the target, i.e., the objective function has less power in the low-ℓ modes compared to the resultant.

The high-pass phase plate's ability to attenuate the power spectrum in the low-order modes is illustrated in Fig. 89.14 for a single beam with and without 2-D SSD and PS. The high-pass phase plate is able to attenuate the power spectrum by a factor of ~10 over a range that doesn't include the far-field envelope $10 < \ell \le 200$. When all of the 60 OMEGA laser beams are calculated and projected onto the target sphere, the effect of the far-field envelope is removed and the high-pass phase plate is observed to attenuate the mode amplitudes over the full range $0 < \ell \le 100$ by a factor of $\sim\sqrt{10}$, as illustrated in Fig. 89.15.

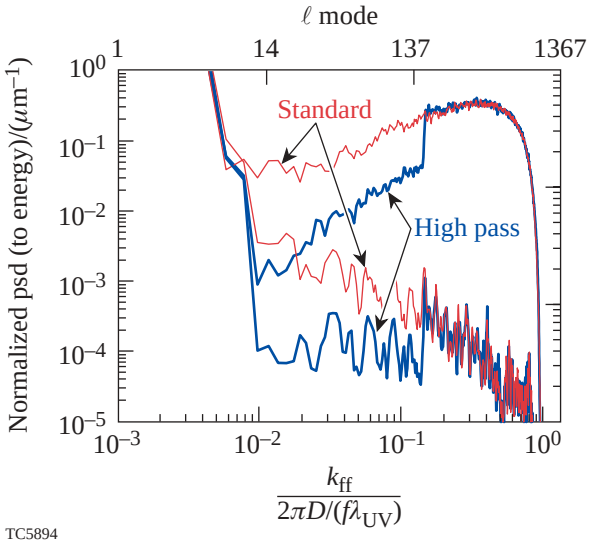

Figure 89.14
The azimuthally integrated, single-beam far-field power spectrum (normalized to the total energy) resulting from the high-pass phase plate (thick lines) for OMEGA is compared to the power spectrum of the standard phase plate (thin lines). The upper lines represent the instantaneous speckled far field without SSD or PS applied, and the lower lines represent the smoothed power spectrum that results from 1-THz, 2-D SSD with PS in the asymptotic limit. Phase aberrations have not been applied.

A second high-pass phase plate, also designed with *Zhizhoo'*, attempted to slowly reduce the far-field power spectrum over the range $0 < \ell \le 200$. The goal here was to make the greatest reduction in the lower-ℓ-mode range of $0 < \ell \le 20$. As illustrated in Fig. 89.16, the power spectrum was, on average, attenuated by nearly a full factor of 100 across the whole band $\ell < 200$ with most of the benefit occurring at the lower-ℓ modes.

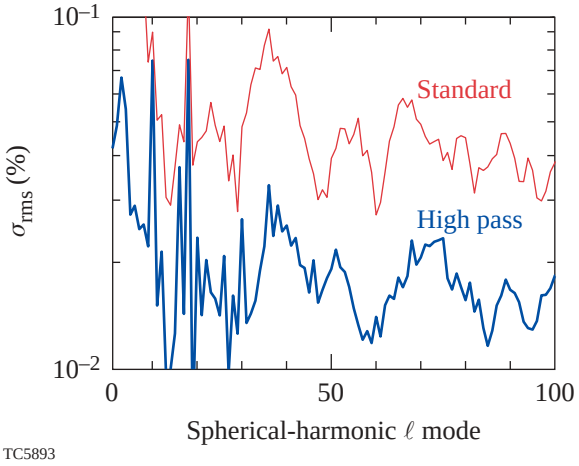

Figure 89.15
The ℓ-mode spectrum of an OMEGA 60-beam projection onto a target sphere resulting from the high-pass phase plate (blue line) is compared to the ℓ-mode spectrum of the standard phase plate (red line). These spectra result from 1-THz, 2-D SSD with PS in the asymptotic limit. The target sphere had a diameter of 950 μm. Note that these data are spectral amplitudes. The strong spectral peaks in the low-ℓ-mode range are due to the combined effect of the envelope shape and the target sphere radius, e.g., ℓ = 10.

2. NIF Phase Plate Designs

The design process for the NIF is very similar to that of OMEGA except that the near field is square and the dimensions are different. The targeted far-field intensity envelope for both NIF phase plate designs is a round super-Gaussian of order 8 (sg = 8) and an IFWHM radius of r_0 = 1.26 mm. This far-field intensity envelope target defines a 95% enclosed energy contour with a diameter of D_{95} = 2.7 mm. The higher super-Gaussian order was chosen in this case for the NIF because the faster roll-off fits better in the simulation space; a lower order would require a larger grid to provide adequate sampling of the far field (which will be done for production-quality designs). This sg = 8 still provides insight into the high-pass designs, even though it does not provide the best

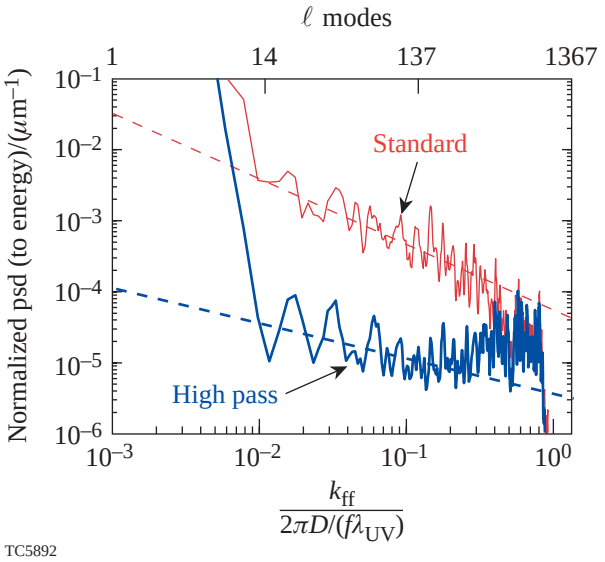

Figure 89.16
The azimuthally integrated, single-beam far-field power spectrum (normalized to the total energy) resulting from the second high-pass phase plate (blue line) is compared to the ℓ-mode spectrum of the standard phase plate (red line). These spectra result from 1-THz, 2-D SSD with PS in the asymptotic limit. The slower filter used reduced the power in the ℓ modes in the range of $0 < \ell \le 200$ by nearly a factor of 100 with most of the reduction occurring in the lower-ℓ modes. The two dashed lines represent the approximate average level of the power spectra and are intended as a guide.

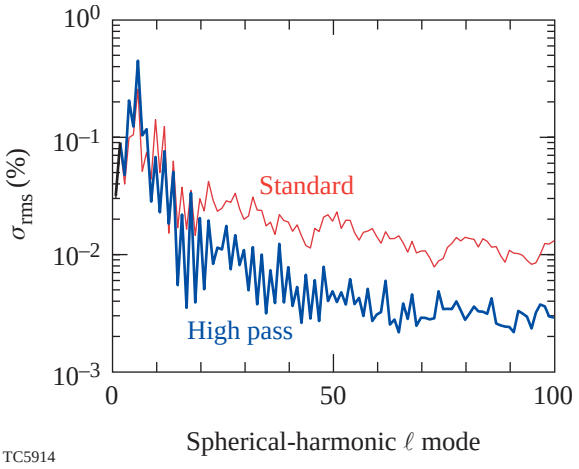

Figure 89.17
The ℓ-mode spectrum of a NIF 192-beam projection onto a target sphere resulting from the high-pass phase plate (blue line) is compared to the ℓ-mode spectrum of the standard phase plate (red line). These spectra result from 1-THz, 2-D SSD with PS in the asymptotic limit. The target sphere had a diameter of 3 mm. Note that these data are spectral amplitudes. A sharp-cutoff, wideband high-pass filter was used to attenuate the ℓ modes in the range of $0 < \ell \le 200$ and was able to reduce them by a factor of $\sim\sqrt{10}$ over this range.

spherical-target illumination. The near-field clear aperture is square and has a width of 35.1 cm in each direction. The simulation space for the near field was a 1024×1024 grid spanning 70.2 cm, and the corresponding far field covered 3.94 mm on a 1024×1024 grid.

Zhizhoo' was then run to design both a continuous standard and a high-pass phase plate to match this super-Gaussian far-field target. The high-pass function used was a wideband, sharp filter, which attempted to attenuate all modes $0 < \ell \le 200$ and pass all others. *Zhizhoo'* completed the high-pass design using the same fixed number of iterations as before, which ended with a rms near-field error of $\sigma_{ff} = 6.5\%$; the standard phase plate design completed with $\sigma_{ff} = 3.1\%$. As with the OMEGA designs, the resultant far-field envelopes match the target function very well.

Figure 89.17 illustrates the performance of the high-pass phase plate relative to the standard phase plate when all of the 192 NIF laser beams are calculated and then projected onto the target sphere. The high-pass phase plate is able to reduce the amplitudes by a factor of $\sim\sqrt{10}$ for modes over the range $0 < \ell \le 200$.

Effects of Near-Field Phase Aberrations

A near-field phase aberration can have a profound effect on the performance of the high-pass phase plates. The phase of the aberration modifies the way in which near-field elements interfere in the far field to produce the speckle pattern. The complex near field has a specific autocorrelation due to the phase pattern of the high-pass phase plate; viz., the Fourier transform of the far-field intensity is equivalent to the autocorrelation of the complex near field, i.e., the autocorrelation theorem (see Ref. 29). An aberration affects the autocorrelation of the near field and disrupts the specific relationship that was developed during the iteration process. If the aberration is strong enough, it acts like a randomizer, and the resultant far-field power spectrum tends toward that of the standard phase plate; i.e., speckle statistics that behave like those due to a phase plate with circular Gaussian statistics are simply the autocorrelation of the near-field intensity (plus a delta function at the origin).[43] If the phase aberration is not too strong, the resultant power spectrum is a hybrid of the two and lies somewhere in between.

The spatial frequency of the phase aberration affects different spatial frequencies of the far-field intensity. For example, a high-spatial-frequency phase aberration will affect the long-wavelength features in the far-field intensity and vice versa.

Since typical phase aberrations have a spatial spectrum whose spectrum follows a basic inverse power law in order that the high spatial frequencies will have less power than the lower spatial frequencies, one would expect short-wavelength features of the far-field intensity to be affected first.

The near-field phase aberration, which was measured on OMEGA, corresponds to a beam that is 12× diffraction limited. This phase aberration is used in two ways: (1) as an amplitude spectrum that is calculated and fit to an inverse power law to model phase aberrations of varying strength; and (2) as a fixed phase aberration used in *Waasikwa'* far-field simulations. The azimuthally averaged amplitude spectrum of the measured phase aberration is shown in Fig. 89.18 along with the inverse power law model, which is fit to the data. The model used to fit the azimuthally averaged amplitude spectrum of the measured near-field phase aberration is

$$\tilde{\Phi}\left(k_{\mathrm{nf}}\right) = 2\pi a\left(\frac{k_{\mathrm{nf}}}{2\pi}\right)^{b}, \tag{24}$$

where a defines the magnitude and b defines the power. For the measured near-field phase aberration, $a = 2.45$ and $b = -2.22$. It is assumed that the power law can be scaled by varying the magnitude parameter a while keeping the power b constant. In this way, different far-field simulations can be run with a varying degree of phase aberration. A measure of the strength of the phase aberration is given by the ratio

$$\beta = \frac{D_{95}}{D_{\mathrm{DL}}}, \tag{25}$$

where D_{95} is the diameter of the 95% enclosed energy contour of the far-field spot due to a phase-aberrated beam relative to the 95% enclosed energy contour for a diffraction-limited beam D_{DL}. For OMEGA the diffraction-limited far-field spot diameter is $D_{\mathrm{DL}} = 6.25\ \mu$m and, for the NIF, $D_{\mathrm{DL}} = 23.1\ \mu$m. When the parameters for the model of the power spectrum given in Eq. (24) are $a = 2.45$ and $b = -2.22$, this yields $\beta = 12$, i.e., 12× diffraction limited using the definition of Eq. (25). The phase-aberration amplitude spectrum model given in Eq. (24) can be used to generate a random phase perturbation that matches the power spectrum model, i.e., colored noise (see Ref. 41, pp. 153–154):

$$\Phi_{\mathrm{aber}}\left(x_{\mathrm{nf}}, y_{\mathrm{nf}}\right) = \Re\left\{\tilde{\mathcal{F}}^{-1}\left\{\tilde{\Phi}\left(k_{\mathrm{nf}}\right)\exp\left[i\zeta\left(k_{x_{\mathrm{nf}}}, k_{y_{\mathrm{nf}}}\right)\right]\right\}\right\}, \tag{26}$$

where $\zeta\left(k_{x_{\mathrm{nf}}}, k_{y_{\mathrm{nf}}}\right) \in [0, 2\pi]$ is a random number field and defined at Eq. (11). A random phase aberration of varying strength β can be generated using the model given by Eq. (26) by holding the power $b = -1.23$ constant and changing the value of the amplitude a.

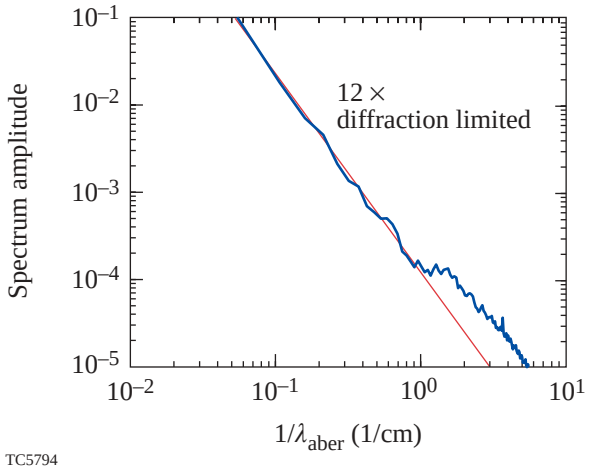

Figure 89.18
The azimuthally averaged power spectrum of a near-field phase aberration measured on OMEGA. An inverse power law model is shown as a fit to this data; fit parameters are $a = 2.4$ and $b = -2.22$ for the model in Eq. (24).

The effect that the phase-aberration strength has on the ℓ-mode spectrum of the far-field intensity for multiple-beam projections is shown in Fig. 89.19. The strength parameter β is increased, and the amplitude spectrum begins to change the shorter-wavelength features initially. This is due to the nature of the power spectrum of the phase aberration; the longer wavelengths have more power than the shorter wavelengths. The longer wavelengths of the phase aberration affect the shorter wavelengths of the far-field intensity, i.e., the autocorrelation of the complex near field is disrupted. When the strength parameter β is large enough, e.g., $\beta > 12$, it is difficult to tell the difference between the aberrated far field and the far-field intensity power spectrum due to the standard phase plate.

A benefit from the high-pass phase plates can still be realized in the lower-ℓ modes in the presence of typical near-field phase aberrations. The multiple-beam projection of the far-field intensity onto the target sphere becomes necessary to

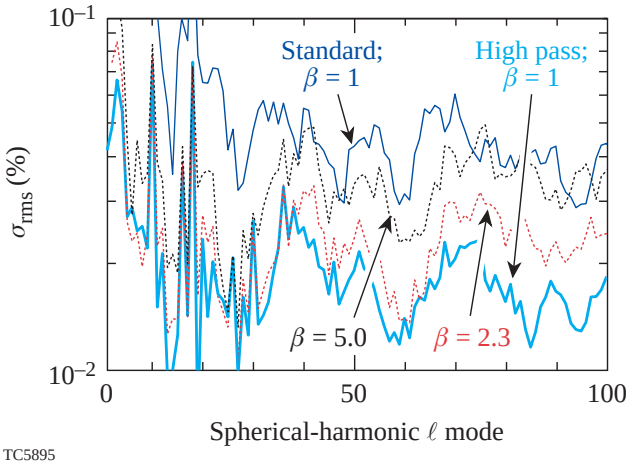

Figure 89.19
The ℓ-mode spectrum of an OMEGA 60-beam projection onto a target sphere due to the standard (upper thin line) and the high-pass (lower thick line) phase plate without phase aberrations is plotted for reference; these are the same traces that correspond to the single-beam spectra in Fig. 89.14. The ℓ-mode spectra of the far-field intensity due to the high-pass phase plate with varying degrees of phase aberration (β = 2.3 and β = 5.0) using the models in Eqs. (24) and (26) are shown (dashed lines). As the strength parameter β increases, the power spectrum tends toward that produced by the standard phase plate beginning with the shorter wavelengths. The shorter wavelengths of the far field are disrupted by the longer wavelengths of the phase aberration where the aberration has the strongest spectral amplitude (see Fig. 89.18).

gather this information because the envelope power overwhelms the power spectrum for the single beam for modes $\ell < 20$. A measure of the benefit gained from the high-pass phase plate is given by the ratio of the nonuniformity due to the high-pass phase relative to the standard phase plate summed over the desired ℓ-mode range, viz.,

$$\Gamma = \left[\frac{\sum_{\ell=\ell_{min}}^{\ell_{max}} \gamma_\ell^2}{\sum_{\ell=\ell_{min}}^{\ell_{max}} \hat{\gamma}_\ell^2} \right]^{1/2}, \qquad (27)$$

where γ_ℓ and $\hat{\gamma}_\ell$ are the amplitudes of the spherical ℓ-mode decomposition for the high-pass and standard phase plates, respectively. The amount of benefit that can be realized becomes a function of the ℓ-mode range covered because of (1) the aforementioned effect of the shape of the phase aberration power spectrum and (2) the stationary modes on the target sphere that develop from the shape of the far-field envelope.

The high-pass benefit function Γ (for the high-pass phase plate designed with the wideband sharp filter) is plotted in Fig. 89.20 for the OMEGA laser as a function of the phase-aberration strength β for four different ℓ-mode ranges. The lower-ℓ-mode range $11 \le \ell \le 25$ realizes the largest benefit (Γ = 1.6 for typical system aberration of β = 12) because the shortest-wavelength features of the phase aberration are not strong enough to totally disrupt the high-pass phase plate. The high-pass phase plate that was designed with the slower filter also achieves an $\Gamma \sim \sqrt{2}$ even though the non-aberrated performance is much higher than that of the first high-pass phase plate. The results for the NIF high-pass phase plate are very similar and are shown in Fig. 89.21. A scaled model of the near-field phase aberration is used for the NIF calculations since the actual aberration is not currently known.

As a final look at the performance of the high-pass phase plates on OMEGA, two *Waasikwa'* far-field simulations were run for a square pulse shape with 1-THz, 2-D SSD and PS: one with the standard phase plate and one with the high-pass phase plate. *Waasikwa'* has the ability to perform multiple-beam projections onto a target sphere: 60 beams are projected onto a target sphere with a diameter of 950 μm. The nonuniformity, covering the ℓ modes $12 \le \ell \le 25$, of far-field intensity due to the standard phase plate is plotted in Fig. 89.22 against that due to the high-pass phase plate. The full benefit of the high-pass phase plate is not realized until after 300 ps. This occurs

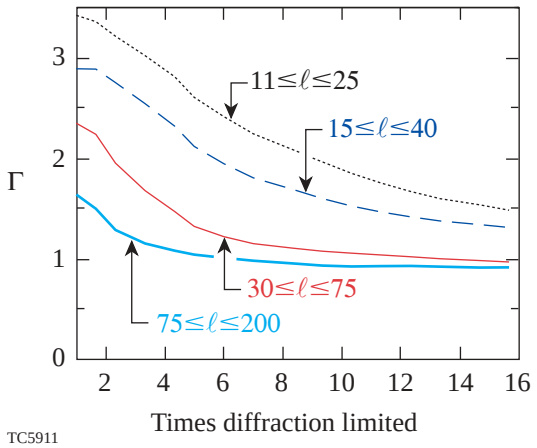

Figure 89.20
The benefit realized by the high-pass phase plate [given by Eq. (27)] is plotted as a function of the phase-aberration strength β for the OMEGA laser. The smoothing applied is 1-THz, 2-D SSD in the asymptotic limit with PS. Four different ℓ-mode ranges are covered (as labeled on the plot): $11 \le \ell \le 25$, $15 \le \ell \le 40$, $30 \le \ell \le 75$, and $75 \le \ell \le 200$.

because early in time the phase imparted by the 2-D SSD system disrupts the specific autocorrelation of the complex near field in the same way that a phase aberration does. In contrast to the static phase aberration, the phase due to 2-D SSD moves across the near field at a constant rate.[45] This movement over time effectively averages the phase due to 2-D SSD after the duration of the slowest phase modulator. In the case of the current 1-THz, 2-D SSD system, the slowest modulator is 3.3 GHz, which yields a cycle time of ~300 ps.

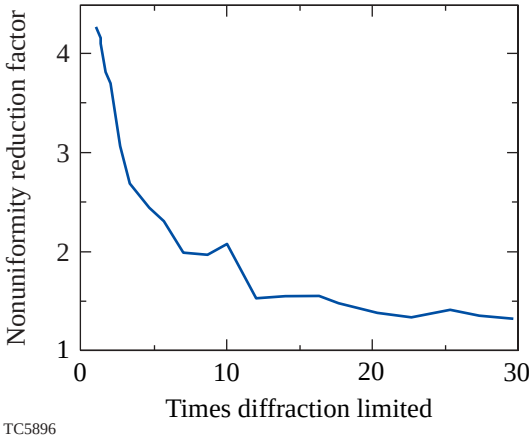

Figure 89.21
The benefit realized by the high-pass phase plate [given by Eq. (27)] is plotted as a function of the phase-aberration strength β for the NIF laser. The smoothing applied is 1-THz, 2-D SSD in the asymptotic limit with PS. A single ℓ-mode range is covered: $20 \le \ell \le 60$.

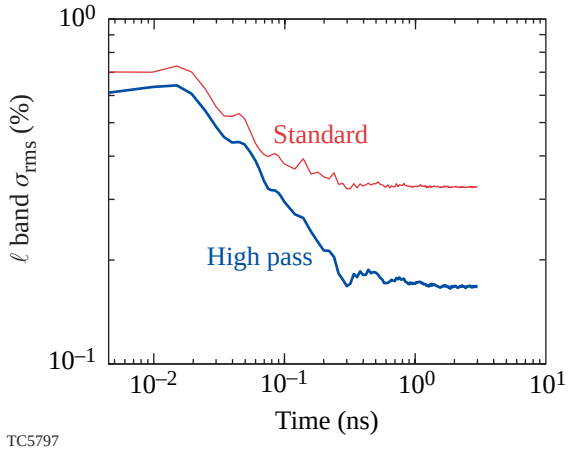

Figure 89.22
The nonuniformity of the far-field intensity over the ℓ-mode range of $12 \le \ell \le 25$ due to the standard phase plate is plotted against that due to the high-pass phase plate for the OMEGA laser. The data represent the results of *Waasikwa'* far-field simulations for a square pulse shape and 1-THz, 2-D SSD with PS. The measured near-field phase aberration was applied to both cases. The full benefit of the high-pass phase plate is not achieved until after 300 ps, when the slowest modulator (ν_m = 3.3 GHz) has completed one full cycle.

Conclusion

A novel phase plate design technique, based on the standard phase-retrieval algorithm, has been introduced and is able to generate continuous phase plates with outstanding control of the far-field intensity envelope, azimuthal asymmetries, and the far-field power spectrum. This new technique is able to overcome many of the difficulties associated with the standard phase-retrieval algorithm (namely, stagnation) and is able to capitalize on the computational efficiency of this method.

The novel phase plate design technique was incorporated into a code called *Zhizhoo'*, which is used to calculate a number of continuous phase plates for both OMEGA and the NIF. A standard phase plate was designed and employed as a reference to the high-pass phase plates in order to measure the performance when the power in the low ℓ-mode range is reduced. Without near-field phase aberrations, large benefit factors of $\Gamma \sim \sqrt{10}$ or even $\Gamma \sim 10$ are obtained, depending on the manner in which the far-field power spectrum is filtered during the iterative calculations carried out in *Zhizhoo'*. Near-field phase aberrations were shown to have a deleterious affect on the performance of the high-pass phase plates. It was found that a reasonable benefit is still realized, $\Gamma \sim 2$ for the ℓ-mode range $12 \le \ell \le 25$, even in the presence of typical near-field phase aberrations. A benefit for both OMEGA and the NIF in the lower and more-dangerous ℓ modes is anticipated by using the high-pass phase plates for direct-drive ICF experiments.

ACKNOWLEDGMENT

The author would like to thank Dr. Stan Skupsky for suggesting this project and Dr. Reuben Epstein for informative discussions. In addition, this work was partially supported by the U.S. Department of Energy Office of Inertial Confinement Fusion under Cooperative Agreement No. DE-FC03-92SF19460, the University of Rochester, and the New York State Energy Research and Development Authority. The support of DOE does not constitute an endorsement by DOE of the views expressed in this article.

REFERENCES

1. C. P. Verdon, Bull. Am. Phys. Soc. **38**, 2010 (1993).

2. S. E. Bodner, D. G. Colombant, J. H. Gardner, R. H. Lehmberg, S. P. Obenschain, L. Phillips, A. J. Schmitt, J. D. Sethian, R. L. McCrory, W. Seka, C. P. Verdon, J. P. Knauer, B. B. Afeyan, and H. T. Powell, Phys. Plasmas **5**, 1901 (1998).

3. D. K. Bradley, J. A. Delettrez, and C. P. Verdon, Phys. Rev. Lett. **68**, 2774 (1992).

4. J. Delettrez, D. K. Bradley, and C. P. Verdon, Phys. Plasmas **1**, 2342 (1994).

5. J. D. Kilkenny, S. G. Glendinning, S. W. Haan, B. A. Hammel, J. D. Lindl, D. Munro, B. A. Remington, S. V. Weber, J. P. Knauer, and C. P. Verdon, Phys. Plasmas **1**, 1379 (1994).

6. R. Epstein, J. Appl. Phys. **82**, 2123 (1997).

7. V. A. Smalyuk, T. R. Boehly, D. K. Bradley, V. N. Goncharov, J. A. Delettrez, J. P. Knauer, D. D. Meyerhofer, D. Oron, and D. Shvarts, Phys. Rev. Lett. **81**, 5342 (1998).

8. F. J. Marshall and G. R. Bennett, Rev. Sci. Instrum. **70**, 617 (1999).

9. F. J. Marshall, J. A. Delettrez, V. Yu. Glebov, R. P. J. Town, B. Yaakobi, R. L. Kremens, and M. Cable, Phys. Plasmas **7**, 1006 (2000).

10. S. Skupsky, R. W. Short, T. Kessler, R. S. Craxton, S. Letzring, and J. M. Soures, J. Appl. Phys. **66**, 3456 (1989).

11. Laboratory for Laser Energetics LLE Review **69**, 1, NTIS document No. DOE/SF/19460-152 (1996). Copies may be obtained from the National Technical Information Service, Springfield, VA 22161.

12. S. Skupsky and R. S. Craxton, Phys. Plasmas **6**, 2157 (1999).

13. J. E. Rothenberg, J. Opt. Soc. Am. B **14**, 1664 (1997).

14. T. J. Kessler, Y. Lin, J. J. Armstrong, and B. Velazquez, in *Laser Coherence Control: Technology and Applications*, edited by H. T. Powell and T. J. Kessler (SPIE, Bellingham, WA, 1993), Vol. 1870, pp. 95–104.

15. Y. Lin, T. J. Kessler, and G. N. Lawrence, Opt. Lett. **21**, 1703 (1996).

16. T. R. Boehly, D. L. Brown, R. S. Craxton, R. L. Keck, J. P. Knauer, J. H. Kelly, T. J. Kessler, S. A. Kumpan, S. J. Loucks, S. A. Letzring, F. J. Marshall, R. L. McCrory, S. F. B. Morse, W. Seka, J. M. Soures, and C. P. Verdon, Opt. Commun. **133**, 495 (1997).

17. Y. Kato, unpublished notes from work at LLE, 1984.

18. K. Tsubakimoto *et al.*, Opt. Commun. **91**, 9 (1992).

19. K. Tsubakimoto *et al.*, Opt. Commun. **103**, 185 (1993).

20. Laboratory for Laser Energetics LLE Review **45**, 1, NTIS document No. DOE/DP40200-149 (1990). Copies may be obtained from the National Technical Information Service, Springfield, VA 22161.

21. T. E. Gunderman, J.-C. Lee, T. J. Kessler, S. D. Jacobs, D. J. Smith, and S. Skupsky, in *Conference on Lasers and Electro-Optics*, Vol. 7, 1990 OSA Technical Digest Series (Optical Society of America, Washington, DC, 1990), p. 354.

22. J. E. Rothenberg, J. Appl. Phys. **87**, 3654 (2000).

23. S. P. Regan, J. A. Marozas, J. H. Kelly, T. R. Boehly, W. R. Donaldson, P. A. Jaanimagi, R. L. Keck, T. J. Kessler, D. D. Meyerhofer, W. Seka, S. Skupsky, and V. A. Smalyuk, J. Opt. Soc. Am. B **17**, 1483 (2000).

24. J. A. Marozas, S. P. Regan, J. H. Kelly, D. D. Meyerhofer, W. Seka, and S. Skupsky, J. Opt. Soc. Am. B **19**, 7 (2002).

25. R. Epstein and S. Skupsky, J. Appl. Phys. **68**, 924 (1990).

26. Inspired by Anishinaabe words *zhizhoo'* meaning "spreads someone using something" and *zhizhoo'an* "spreads something using something" just as the phase plate spreads out the diffraction-limited, far-field spot to match the far-field objective. Resource: J. D. Nichols and E. Nyholm, *A Concise Dictionary of Minnesota Ojibwe* (University of Minnesota Press, Minneapolis, 1995).

27. R. W. Gerchberg and W. O. Saxton, Optik **35**, 237 (1972).

28. J. R. Fienup, Appl. Opt. **21**, 2758 (1982).

29. J. W. Goodman, *Introduction to Fourier Optics* (McGraw-Hill, New York, 1988).

30. E. Wolf, Proc. Phys. Soc. **80**, 1269 (1962).

31. F. Wyrowski and O. Bryngdahl, J. Opt. Soc. Am. A **5**, 1058 (1988).

32. Y. Lin, T. J. Kessler, and G. N. Lawrence, Opt. Lett. **20**, 764 (1995).

33. B. Ya. Zel'dovich, N. F. Pilipetsky, and V. V. Shkunov, in *Principles of Phase Conjugation*, edited by J. M. Enoch *et al.*, Springer Series in Optical Sciences (Springer-Verlag, Berlin, 1985), Sec. 3.5, Vol. 42, pp. 79–84.

34. H. Aagedal *et al.*, J. Mod. Opt. **43**, 1409 (1996).

35. D. C. Ghiglia and M. D. Pritt, *Two-Dimensional Phase Unwrapping: Theory, Algorithms, and Software* (Wiley, New York, 1998).

36. J. R. Fienup and C. C. Wackerman, J. Opt. Soc. Am. A **3**, 1897 (1986).

37. E. C. Titchmarsh, Proc. London Math. Soc. **25**, 283 (1926).

38. M. S. Scivier and M. A. Fiddy, J. Opt. Soc. Am. A **2**, 693 (1985).

39. M. S. Scivier, T. J. Hall, and M. A. Fiddy, Opt. Acta **31**, 619 (1984).

40. N. B. Baranova and B. Ya. Zel'dovich, Sov. Phys.-JETP **53**, 925 (1981).

41. A. B. Carlson, *Communication Systems: An Introduction to Signals and Noise in Electrical Communication*, McGraw-Hill Electrical and Electronic Engineering Series (McGraw-Hill, New York, 1968), pp. 153–154.

42. W. H. Press, *Numerical Recipes in C: The Art of Scientific Computing* (Cambridge University Press, Cambridge, England, 1988).

43. J. W. Goodman, in *Laser Speckle and Related Phenomena*, edited by J. C. Dainty, Topics in Applied Physics (Springer-Verlag, Berlin, 1984), Chap. 2, Vol. 9, pp. 9–75.

44. Laboratory for Laser Energetics LLE Review **64**, 170, NTIS document No. DOE/SF/19460-99 (1995). Copies may be obtained from the National Technical Information Service, Springfield, VA 22161.

45. Laboratory for Laser Energetics LLE Review **78**, 62, NTIS document No. DOE/SF/19460-295 (1999). Copies may be obtained from the National Technical Information Service, Springfield, VA 22161.

Advanced Tritium Recovery System

Introduction

As part of the U.S. Inertial Confinement Fusion Program, LLE plans to implode deuterium–tritium (DT)–charged microspheres. These microspheres are filled with high-pressure deuterium and tritium gas under cryogenic conditions. The spheres are then stored and transferred as needed to the target chamber (located in an adjacent room) under vacuum and at temperatures near 20 K. LLE is licensed to handle up to 10,000 Ci of tritium, but site release target is less than 1 Ci per year.

LLE is currently upgrading the systems used to produce, transfer, store, and implode these targets. As part of this upgrade, extensive efforts are being made to ensure staff safety and to limit the radioactive effluent that can be released to the environment. Two independent tritium recovery systems (TRS), currently under construction, will capture any tritium that comes from the various sources. One system will serve Room 157, which houses the production, characterization, and storage of targets, and the other system will serve the target chamber, where the targets are imploded. The exhaust emissions from the process streams, from the gloveboxes that house the streams, and from equipment outgassing will have to be collected and treated to remove any tritium present. This article provides an overview of the requirements and describes the technologies that were considered for the decontamination of the process streams and glovebox-cleanup systems for Room 157.

TRS Design Considerations

1. General Constraints and Considerations

To maximize personnel safety and minimize site emission, the following factors were considered as part of the decontamination systems' design:

(a) Critical components and large inventories have secondary or tertiary containment.

(b) No single component failure results in a release of tritium to the room or to the stack.

(c) Systems containing tritium are designed for high integrity, having all stainless components, with either welded connections or leak-tight (VCR) fittings and a minimum of elastomer seals.

(d) Complex operations are typically automated or, if manual, are covered by detailed procedures.

(e) Protective systems that are poised are designed to be tested regularly to ensure their operability.

(f) Active components are designed to allow easy maintenance.

In addition to the design considerations, the operating staff is technically knowledgeable and extensively trained in handling tritium.

While the system has been designed to limit the likelihood of accidental emissions to a very low probability, additional features are included to minimize chronic releases. These can be summarized as follows:

(a) Since the radiotoxicity of HTO is about 10^4 times greater than that of HT, every effort is made to avoid oxidizing any HT present to HTO.

(b) Mixing of exhaust streams having different gases or tritium concentrations is minimized to limit the quantities of effluent to be decontaminated.

(c) All exhaust streams are monitored and controlled.

(d) All accessible areas are well ventilated to avoid potential tritium buildup due to outgassing from contaminated equipment.

2. Room 157 Functional Requirements

To achieve the above objectives, the Room 157 effluent gases are divided into the following four categories:

– DT high-pressure-system (DTHPS) secondary containment (SC) cleanup
– Glovebox (GB) cleanup (low Y, inert)
– Helium vacuum exhaust cleanup [high temperature (high T), inert]
– Air vacuum exhaust cleanup [low temperature (low T), air]

The relationships between the streams and the subsystems that release these streams are provided in Fig. 89.23.

This sorting was done in order to select the best technology for each type of stream and, as a result, achieve the best performance (i.e., lowest emissions) at a reasonable cost.

The DTHPS handles pure DT under high pressure, so it has its own secondary containment, which, in turn, has its own tritium-scavenging system to collect any DT that escapes from the DTHPS. This DTHPS secondary containment and its DT scavenging system are housed inside the DTHPS glovebox. For these reasons, it is impractical to combine its effluent with any of the other systems.

The second category consists of the gloveboxes that have helium atmospheres. Three process trains exist: one for the DTHPS glovebox atmosphere, one for the FTS (fill transfer station) and TFS (tritium fill station) glovebox atmospheres, and one that acts as a backup to either. Each train consists of a circulating pump, a drier, and, finally, an HT removal bed. Interconnections are provided to allow various combinations of pumps, driers, and HT removal beds. The driers serve primarily to remove any moisture that permeates into the gloveboxes in order to avoid excess loading of the tritium scavengers, but the driers will also remove any HTO that may be present.

The rationale for further splitting the glovebox-cleanup function is that the DTHPS has its own internal containment and the DTHPS glovebox represents a tertiary containment. It will normally have no or very low levels of tritium, so it will require essentially no cleanup on an ongoing basis. The FTS and TFS gloveboxes have comparable levels of tritium activity, so mixing these will have no significant effect on cleanup. Another factor is the potential for dilution. Since the effectiveness of cleanup is to some extent driven by the initial concentration of tritium, mixing essentially clean streams with contaminated streams actually decreases the tritium concentration in the contaminated stream, resulting in reduced capture efficiencies in some devices.

The third category consists of the vacuum systems that service the helium processes. Again, a further subdivision of this group separates the “clean” sources, specifically the FTS base, dome and cooling loop, permeation cell seal, stalk

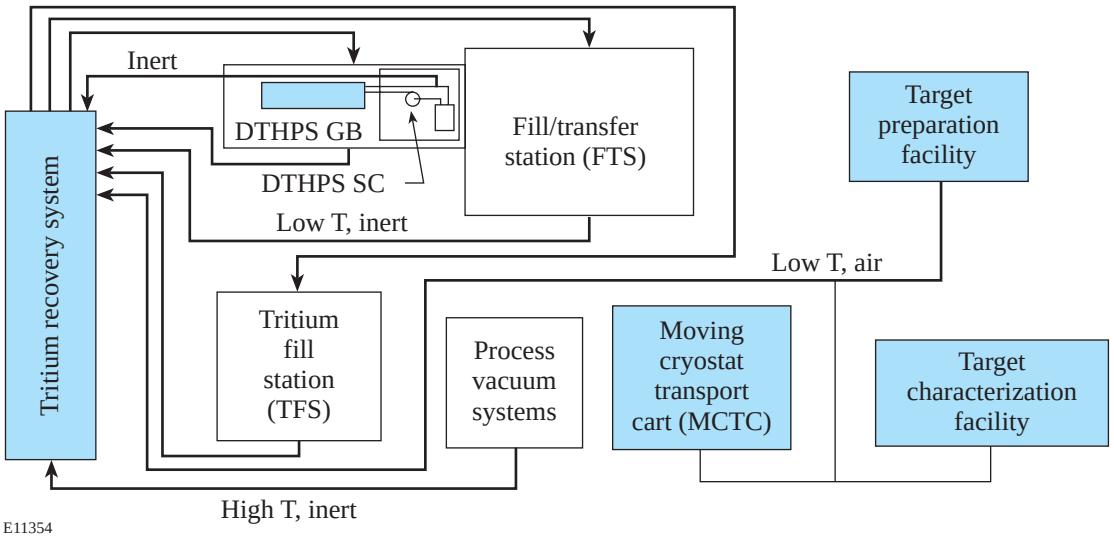

Figure 89.23
The Room 157 Tritium Recovery System must deal with air and inert gas streams from a variety of sources.

aligner, and borescope, from potentially contaminated sources. Using a monitor to confirm the absence of tritium, the exhaust is routed directly to the stack. If tritium activity is detected, the stream is combined with the other helium vacuum exhaust streams for treatment.

All other helium vacuum exhaust steams are combined into a collection tank. A pump circulates the gas through a drier to remove any HTO, a Ni catalyst bed cracks any organically bound tritium, and finally a scavenger bed removes the product HTO. The subsystem pressure is capped by a relief valve that discharges to a second tank, which can also recirculate any effluent through a second scavenger. The gas in this second loop should be essentially tritium free and should be releasable to the environment. Any discharged gas is nevertheless monitored, and, if it requires further decontamination, it can be routed to the air vacuum exhaust for additional processing.

The final category comprises air vacuum exhaust streams. These streams are not subdivided since they are all normally active, so they will require a routine processing. The stream is initially passed through a drier bed to remove any tritium that might be present as HTO. This may be sufficient to allow the exhaust to be released to the stack, so the stream is monitored at this point and, if possible, sent to stack. If the level of tritium activity is still above the release criteria, the stream is routed to a catalytic oxidizer to convert any tritium that may be present as HT or organically bound tritium (OBT) to HTO. This effluent is then passed through a condenser and another drier bed before going to stack. The final effluent is once more monitored for compliance purposes.

The catalytic reactor most suitable for the LLE application is palladium-coated alumina operated at high temperature (~450°C) and sized to give a residence time of about 4 s. The reactor is followed by a chiller to cool the exhaust before it goes into a drier bed. The catalytic reactor, chiller, and drier beds used in this application are designed for high flow and low resistance to minimize the need for additional pumps to move the gas through the detritiation loops.

All the tritium removal beds have provision for *in-situ* regeneration to eliminate the need for routine bed removal. The regeneration of the HT scavenging beds is accomplished by heating the bed and using a helium carrier flow to accumulate the released HT on a cryogenic molecular sieve before it is transferred to a transportable U-bed for eventual removal from the system. Thus, any captured HT will remain in the elemental form throughout the entire tritium cycle.

The drier beds are also heated for regeneration, releasing the HTO, which is carried by an N_2 gas carrier to a chiller followed by a condenser to remove the bulk of the moisture. The gas then flows to a polishing drier bed, is monitored, and finally released to stack. The recovered moisture, including HTO, is collected in liquid form for interim storage, pending final disposal. Regeneration of driers is by reverse flow to counteract HTO tailing in the drier beds. Hot, dry nitrogen gas is used as a carrier to achieve dew points below −100°C. This allows an extended operating cycle while still maintaining the low outlet tritium concentration needed to meet emission targets.

Tritium Removal Technologies

A number of viable options are available for removing HT from inert gas streams, and given the number of helium-based streams at LLE, every effort was made to use this capability to minimize the production of HTO. The following section examines the technologies that were applicable to the LLE Tritium Removal System.

1. Uranium Beds

Uranium reacts exothermically with hydrogen at room temperature, forming UH_3. Uranium has a high storage capacity for hydrogen (up to 300 scc/g U) and uniform reaction kinetics over a very large H/U ratio. The decontamination factor varies depending on flow and tritium concentration, but a practical minimum effluent concentration of $\lesssim 2$ mCi/m^3 is achievable.[1]

The hydriding reaction is reversible, and by heating the hydride to ~400°C, the hydrogen is released, restoring the bed to its original state. Varying the amount of heat applied can control the hydrogen release rate. However, uranium reacts not only with hydrogen, but also reacts strongly with oxygen and somewhat with nitrogen at room temperatures. Both the oxidation and nitriding are exothermic and become more vigorous at elevated temperatures. When purged with air, U-beds will release stored tritium.

For this reason, uranium can be used only for tritium removal from inert gas streams. It will remove large amounts of tritium with high efficiency and will do so for considerable carrier gas flow rates. Its affinity for oxygen and, to some extent, other gases serves to purify the tritium since only the hydrogen isotopes are released when uranium is heated, although at the cost of irreversibly reacting with the uranium. U-beds have been extensively used, and a very large experience base exists to support this application.

Uranium is not recommended for inert glovebox atmosphere cleanup since the practical decontamination level of ~2 mCi/m^3 is higher than desired. It is best used where large quantities of tritium must be removed and where the effluent will not be released to stack.

2. Zirconium-Iron (ZrFe) Beds

The ZrFe alloy known as ST-198 can also scavenge tritium from inert gas streams since it forms a stable tritide that can be reversibly decomposed.[2] It has a rather modest storage capacity for tritium (0.8 scc/g alloy yields a 1-mCi/m^3 vapor present over the alloy) but can decontaminate to μCi/m^3 levels if tritium inventory of the alloy is kept sufficiently low. Although it requires a substantial residence time (>3 s) to achieve good detritiation, it is an excellent tritium scavenger for glovebox decontamination and for polishing exhaust streams before stacking. Since ST-198 reacts very slowly with nitrogen at room temperature, it can be used to scavenge HT from nitrogen streams.[3] It does not react with organics (CH_4), so it will not scavenge tritiated organics from a gas stream unless the stream has been preconditioned with a nickel catalyst to crack the organics to produce HT.[4,5] While ST-198 can be regenerated by heating, it degrades during this process and consequently has a limited lifetime.

Like uranium, ST-198 reacts with oxygen at room temperature and with nitrogen at elevated (≳450°C) temperatures. Both reactions will release stored tritium. ZrFe is best where quantities of hydrogen isotopes are limited, but where the effluent tritium concentration must be suitable for release to the environment.[6,7]

3. Cryogenic Molecular Sieves

Cryogenic molecular sieves can scavenge hydrogen isotopes from a helium carrier by adsorbing the hydrogen molecules. Depending on the partial pressure of hydrogen that is acceptable, molecular sieves operating at liquid nitrogen (LN) temperatures can have a high capacity for hydrogen isotopes. However, the tritium is not firmly bound in the molecular sieve at 77 K, so the tritium residence time in the bed is finite. The residence time is a function of both flow and geometry in that longer beds and lower flows yield a longer time to breakthrough. Warming the molecular sieve slightly above LN temperatures (i.e., to ~100 K) will release the stored hydrogen isotopes. At these temperatures, all other gases will remain firmly adsorbed, thus allowing the recovery of pure-hydrogen isotopes. These gases can, however, be desorbed by heating the molecular sieve to 350°C, regenerating the molecular sieve to its original condition.

These characteristics make cryosorption an excellent technique to scavenge tritium from helium gas streams. Low exhaust levels of tritium activities can be achieved by limiting the amounts of tritium in the molecular sieve and by monitoring for impending breakthrough. When breakthrough becomes evident, the bed needs to be valved out of service so it can be unloaded. The unloading process proceeds rapidly since the bed needs to be warmed to only 100 K for complete HT unloading.

Figure 89.24 illustrates the efficacy of a cryogenic mole sieve bed to remove HT from a helium stream containing up to 800 mCi/m^3. During this test, the activity downstream of the bed remains below 0.3 mCi/m^3 until breakthrough occurs.

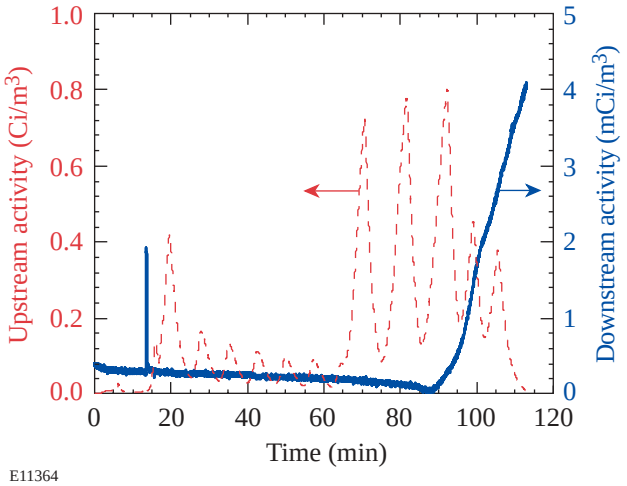

Figure 89.24
Transfer of tritium from 800-g ST198 bed to cryogenic mole sieve bed with a 28 sLPM helium carrier until tritium breakthrough is observed.

The chief disadvantage of cryosorption is that it requires liquid nitrogen temperatures to retain the hydrogen isotopes on the molecular sieve. This means that a loss of cryogenics could result in the inadvertent release of hydrogen. This capture technology is not passively safe. In addition, the complexity of cryogenic handling is costly and requires techniques and skills that are not commonplace. An example is the need for regenerative heat exchangers as part of any cryotrap to obtain high utilization of liquid nitrogen inventories.

System Configuration

A comprehensive tritium removal system (presented schematically in Fig. 89.25) has been designed and is being built so that LLE can perform its research program and still meet tritium emission targets. To ensure that this system can provide the desired detritiation performance and also provide the highest practical degree of staff safety, all relevant technologies were extensively reviewed. Based on this review, ZrFe scavenger beds are used to reduce tritium levels to low values, cryogenic molecular sieves are used to concentrate tritium, and uranium flow-through beds are used to capture large amounts of tritium. Nickel catalysts are used to crack organics, Pd on alumina is used to oxidize any tritium compounds in air systems, and 5A molecular sieve driers were selected to remove HTO. The technologies selected for the final design were those judged most suitable based on demonstrated robustness, effectiveness, and real-life operating experience.

ACKNOWLEDGMENT

This work was supported by the U.S. Department of Energy Office of Inertial Confinement Fusion under Cooperative Agreement No. DE-FC03-92SF19460 and the University of Rochester. The support of DOE does not constitute an endorsement by DOE of the views expressed in this article.

REFERENCES

1. W. T. Shmayda and N. P. Kherani, Fusion Eng. Des. **10**, 359 (1989).
2. W. T. Shmayda, N. P. Kherani, B. Wallace, and F. Mazza, Fusion Technol. **21**, 616 (1992).
3. K. J. Maynard, N. P. Kherani, and W. T. Shmayda, Fusion Technol. **28**, 1546 (1995).
4. N. P. Kherani, W. T. Shmayda, and R. A. Jalbert, Fusion Eng. Proc. **2**, 1239 (1987).
5. A. B. Antoniazzi and W. T. Shmayda, Fusion Technol. **30**, 879 (1996).
6. A. G. Heics and W. T. Shmayda, Fusion Eng. **1**, 65 (1994).
7. A. G. Heics and W. T. Shmayda, Fusion Technol. **28**, 1509 (1995).

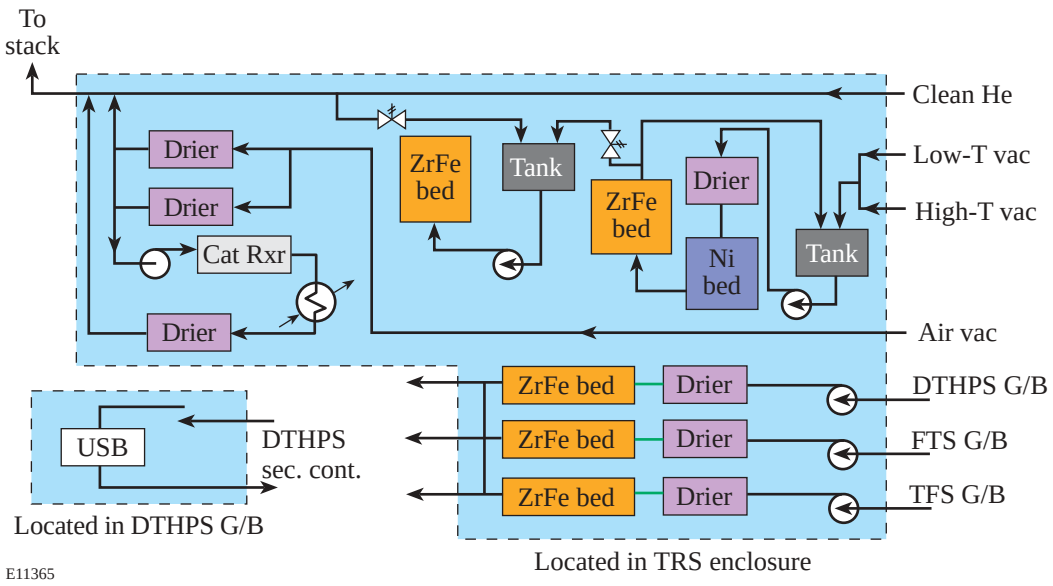

Figure 89.25
Schematic of the Room 157 Tritium Recovery System.

Establishing Links Between Single Gold Nanoparticles Buried Inside SiO_2 Thin Film and 351-nm Pulsed-Laser-Damage Morphology

Introduction

Over the past several years research has indicated that nanoscale defects, dispersed inside thin films with relatively low abundance, are a major laser-damage-initiation source in the UV spectral range.[1–4] The extreme difficulties in characterizing these defects virtually stalled the experimental effort to identify the laser-damage mechanism. This situation led to a proposed model SiO_2-thin-film system[5] with artificially introduced gold nanoparticles serving as well-characterized absorbing defects.

Advantages of such a system include high intrinsic-damage resistance of SiO_2 thin film—which allows artificially-introduced-defect–driven damage to be separated from the intrinsic damage—and the possibility to control the location and size of the nanoparticles. Optical parameters of gold nanoparticles are well documented in scientific literature,[6] and different-sized particles, with narrow size distributions, are available in the form of gold colloids.

Our previous work[5] focused on comparative atomic force microscopy (AFM) investigation of the nanoparticle and 351-nm damage-crater areal density statistic. The results provided the first experimental evidence of the laser energy absorption process spreading from the defect into the thin-film matrix during the laser pulse. The process starts with an absorption in a particle. As the temperature rises, energy transfer from the particle (via UV radiation, thermionic emission, heat conduction, etc.) to the surrounding matrix causes its effective conversion to an absorptive medium and, consequently, damage.

The next step in this work is to establish a direct link between a single nanoparticle buried inside a SiO_2 thin film at a particular location and the film morphology changes caused by pulsed-laser irradiation. The AFM mapping of the film surfaces after particle deposition and laser-irradiation steps opens the possibility of finding, for each detected damage crater, the corresponding nanoparticle, initiating crater formation. As a result, a key question is addressed—How does the damage scale (crater depth and lateral size) correlate with the particle size? Surprisingly, the correlation appears to be very weak, which is explained by the peculiarities of nanoscale defect/host matrix interaction in the inhomogeneous thin-film medium.

The nanoparticle/damage crater correlations also allow direct comparisons of energy deposited in a particle and energy required for crater formation. The results confirm damage mechanism, considering absorption initiation in a particle with subsequent growth of the absorbing volume within the surrounding film matrix on the later laser-pulse stages.

The same correlations reveal crater formation probabilities as a function of the local laser fluence. By extrapolating a probability curve to zero value, one can find the laser fluence at which only limited matrix melting and no crater formation occur, which, later in this article, will be referred to as "nanoscale" damage threshold. Experimental damage thresholds derived this way allow a more-meaningful comparison with theories that consider matrix melting as a damage onset.

Experimental

1. Damage-Test Sample

   Sample preparation involves several steps:

   (a) Fused-silica glass 7980 is cleaved to ~$14 \times 7 \times 6$-mm pieces to provide a virgin unprocessed surface (14×6 mm) for SiO_2 thin-film deposition.

   (b) The sample is taken to the AFM (Nanoscope III, Digital Inst./Veeco) equipped with a nano-indenting diamond tool, which is used to produce small, ~1-μm-lateral-size, 100-nm-deep indentations organized in a square-type pattern with ~20-μm sides. This pattern is later used as a reference to help find the AFM-mapped areas on the sample surface.

(c) The 120-nm-thick SiO_2 coating is prepared by conventional *e*-beam deposition (base pressure 1.3×10^{-6} Torr; deposition rate 26 nm/min).

(d) Gold nanoparticles in the form of gold colloid are diluted in isopropanol (to achieve an average areal density of 0.3 to 3 μm^{-2}) and deposited by a micropipet onto a SiO_2-coated surface. Three particle sizes are used (5.2-nm, 8.4-nm, and 14.3-nm average diameter) but only one size is used for each experiment. The particle-size distributions provided by the supplier (Ted Pella, Inc.) are presented in Fig. 89.26.

(e) After solvent evaporation (special attention is paid here to the solution-drying protocol to prevent *particle agglomeration*), the sample surface is mapped by the AFM at several locations (each map covers ~6×6-μm area) in the vicinity of the indentations. Only a few agglomerated particles, mostly in the form of duplets, can be found at each location. Their portion is less than 10% of the total particle population.

(f) As a final step, the sample is taken a second time to the coating chamber and coated with an additional 60-nm layer of SiO_2.

The SiO_2 thin-film sample resulting from this procedure is 180 nm thick and contains gold nanoparticles at a well-defined depth of 60 nm (Fig. 89.27).

An additional sample, not containing particles, is prepared for each experiment, following the above protocol, to make available an undoped SiO_2 damage-test reference.

2. Damage Testing and Sample Irradiation Conditions

The 351-nm, 0.5-ns pulses from a Nd-doped glass laser are used for 1-on-1 damage-threshold evaluation. Laser-beam spot size (~400 μm) and fluence distribution are obtained from images captured by a CID (charge-injection device) camera in a sample equivalent plane. Damage onset is detected by means of 110×-magnification dark-field microscopy and, since optical tools are used to determine damage threshold, it will be referred to as an "optical" damage threshold. The "nanoscale" damage threshold, associated with the onset of crater formation and derived from the *AFM investigation* of the post-irradiated coating morphology, will be introduced later in this article. The maximum laser fluence level, used to irradiate the AFM-mapped sites, is varied 10% to 70% above the optical damage threshold. Under these conditions, laser-damage

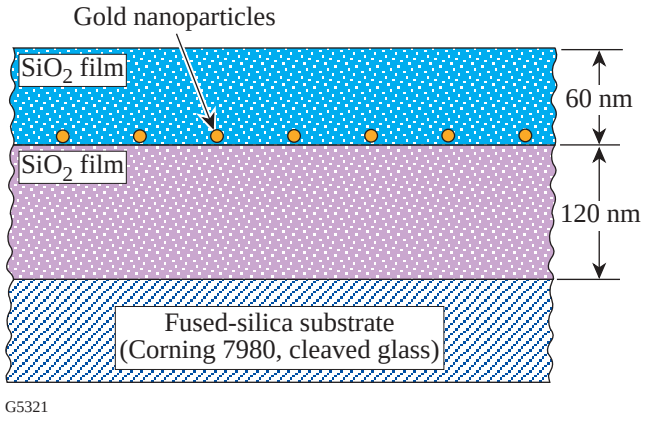

Figure 89.27
Schematic presentation of the SiO_2 sample with embedded gold nanoparticles.

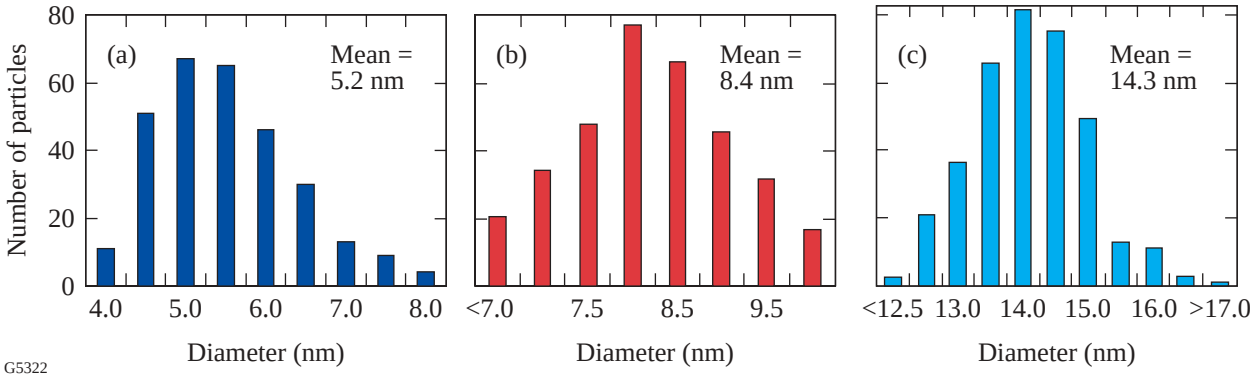

Figure 89.26
Nanoparticle-size distributions provided by the supplier (Ted Pella, Inc.): (a) 5.2-nm, (b) 8.4-nm, and (c) 14.3-nm average diameter.

morphology is represented by submicrometer-scale craters (Fig. 89.28). The laser-beam spot usually covers several mapped sites, which ensures that different damage levels at different mapped sites will be achieved.

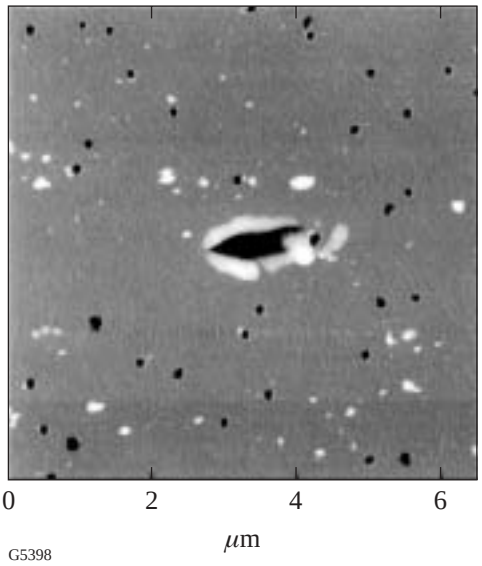

Figure 89.28
The AFM map of a SiO_2 coating containing 8.4-nm gold particles and irradiated by a laser pulse with 4.6-J/cm^2 fluence. The indentation in the center of the map serves as a site identification.

3. AFM Mapping

The very small particle size (up to ~4 nm) limits the maximum AFM scan size during particle mapping. Due to tip-sample convolution effects, a 5-nm-diam particle is typically imaged as a feature with ~20- to 25-nm lateral size. Note that modest convolution does not affect the *vertical* scale, which gives a true particle diameter provided that the pedestal is reasonably flat. Bearing this in mind, 2×2-μm or 3×3-μm AFM scans for 5.2-nm and 8.4-nm particles, correspondingly, were performed. The highest-available, 512×512-pixel image resolution ensures at least five to six data points (pixels) per particle diameter. This requires performing six or seven overlapping, 2×2-μm scans to create a map with a sufficient number of particles for size-effect studies and analyses. The AFM was operated in a tapping mode and employed Si probes with tip radii typically better than 10 nm and apex (last 200 nm) cone angles better than 20°, ensuring ~10-nm lateral resolution. A crater vertical wall slope up to 70° was imaged without convolution along the scan's x axis (along cantilever beam) and up to 80° along the y axis. Typical particle and crater cross-sectional profiles obtained from AFM images are presented in Fig. 89.29.

Results and Discussion

1. Damage Thresholds

The damage-threshold measurement results are summarized in Table 89.I. The introduction of gold nanoparticles causes a dramatic reduction in damage threshold. For the

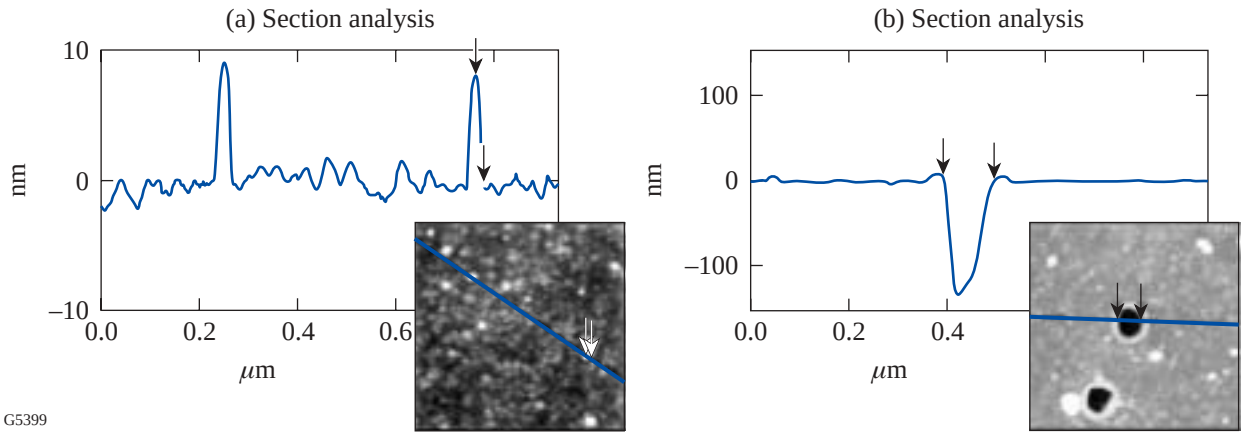

Figure 89.29
Cross-sectional profiles taken through (a) 8.4-nm particles and (b) a typical damage crater.

smallest, 5.2-nm particles, a 4.4-fold reduction, compared to the undoped reference sample, is observed. An even larger threshold drop was found in our previous experiment[5] using the same 5.2-nm particles. It is attributed to particle agglomeration, which is all but eliminated in this work.

The damage-threshold fluence plotted in Fig. 89.30 as a function of the average particle size can be approximated by

$$F_{th} \sim 1/R^t, \quad (1)$$

where R is the particle radius and $t \sim 0.4$ to 1.0.

An extrapolation of this dependence (Fig. 89.30) to the intersection with the threshold value for the undoped reference sample $F_{th} = 27.1$ J/cm^2 allows rough estimates for the absorptivity of the intrinsic absorbing defects. By fitting Eq. (1) to the experimental data with their designated error bars, one finds that the possible range for x intercepts lies between 0.1 nm and 1.4 nm.

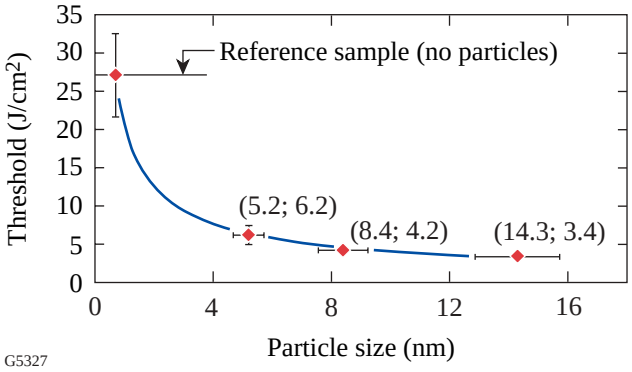

Figure 89.30
Damage threshold as a function of the average particle size. The solid line is the best fit using $F_{th} \sim 1/R^t$ approximation. Numbers in brackets indicate particle size and threshold values, respectively.

It implies that intrinsic defect absorptivity should be similar to the absorptivity of gold particles with a size ≤1.4 nm. Considering Si clusters in SiO_2 film as prime candidates for the intrinsic nanoabsorber role and using Si cluster absorptivity[7] and bandgap/cluster size dependence[8] data, an estimate for the cluster diameter gives values of 1.3 nm ≤ D ≤ 2 nm.

2. Mechanism of Laser-Energy Deposition Inside Thin Film

In all experiments with 5.2-nm and 8.4-nm particles and laser fluences from 2 to 7 J/cm^2, craters were found exclusively at the positions where particles were lodged during deposition (Fig. 89.31). This proves that (1) particles adhere to the SiO_2 film and are not displaced during deposition of the 60-nm capping layer, and (2) absorbing gold defects alone contribute to the damage process at threshold laser fluences.

This one-to-one link between each nanoparticle and the laser-induced local changes in film morphology has a great advantage over other, nonlocal approaches. For instance, energy absorbed by the individual nanoparticle can be compared with energy required to produce a crater at this location. The calculation of energy absorbed by the particle is based on a simple formula:

$$E_{abs} = F\,\sigma_{abs}, \quad (2)$$

where F is the experimentally determined laser-fluence value and σ_{abs} is the Mie[9] absorption cross section.

In the small nanoparticle approximation $2R << \lambda$, fully applicable for particle sizes used in this work, according to the Mie theory,[9] the cross section of this process is dominated by dipolar absorption:

$$\sigma_{abs}(\omega) = 9\frac{\omega}{c}\varepsilon_m^{3/2}V_0\frac{\varepsilon_2(\omega)}{\left[\varepsilon_1(\omega)+2\varepsilon_m\right]^2+\varepsilon_2(\omega)^2}, \quad (3)$$

Table 89.I: Damage thresholds of SiO_2 film containing gold nanoparticles.

Nanoparticle Average Size (nm)	Damage Threshold (J/cm^2)
5.2	6.2±0.2
8.4	4.2±0.1
14.3	3.4±0.2
Reference sample (no particles)	27.1±3.0

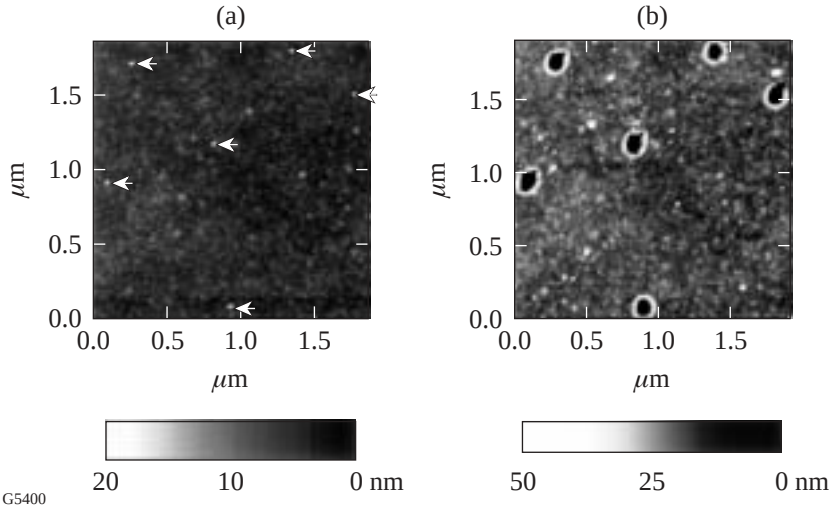

Figure 89.31
AFM images of ~2 × 2-μm surface area containing six nanoparticles: (a) nanoparticle map, (b) same area after 60-nm SiO_2 overcoat and irradiation. The craters are formed at exactly the nanoparticle locations.

where V_0 is the particle volume [$V_0 = (4/3)\,\pi R^3$], ε_m is the dielectric function of the medium (SiO_2), $\varepsilon_1(\omega)$ and $\varepsilon_2(\omega)$ are the real and imaginary parts, respectively, of the particle dielectric function, and ω is the laser frequency. The calculation was done for particle sizes ranging from 4 nm to 12 nm, $\varepsilon_m = 2.19$ for SiO_2, and data for ε_1 and ε_2 are taken from Kreibig *et al.*[6]

The energy required to produce a crater can be estimated by assuming that the material within the crater volume is heated up to the boiling point with subsequent vaporization. The presence of the melting stage is supported by the crater morphology. The glassy, structureless walls and a rim elevated above average surface level [Fig. 89.29(b)] are missing the characteristic granular structure of the surrounding film, which provides clear evidence for melting and resolidification into the glass-type structure during the cooling stage.

Assuming this mechanism, the energy required for crater formation is expressed as

$$E_{\mathrm{cr}} = V_{\mathrm{cr}}\left[C\rho\left(T_b - 293\,\mathrm{K}\right) + H_{\mathrm{fus}} + H_{\mathrm{vap}}\right], \qquad (4)$$

where V_{cr} is the crater volume, C is the silica heat capacity, ρ is the density, T_b is the boiling point, and H_{fus} and H_{vap} are the heat of fusion and heat of vaporization, respectively. Values of the parameters used for the calculation of E_{cr} are $C = 741$ J/kg K, $\rho = 2200$ kg/m^3, $T_b = 2503$ K, $H_{\mathrm{fus}} = 3.12 \times 10^8$ J/m^3, and $H_{\mathrm{vap}} = 7.6 \times 10^9$ J/m^3.

C and ρ are considered independent of temperature for a lack of available high-temperature data (>2000 K). Taking into account that the heat capacity for most glasses increases over the temperature interval of 1 K to 1900 K would result in an ~16% increase in the E_{cr} value calculated from Eq. (4). V_{cr} is derived from AFM data.

The results of calculations for E_{abs} and E_{cr} for eight selected nanoparticles and corresponding craters are presented in Table 89.II, which clearly shows that, considering that the energy absorption process is localized inside the particle, the amount of energy absorbed cannot provide crater formation since $E_{\mathrm{abs}} < E_{\mathrm{cr}}$ for all but one particle (last row).

This conclusion is valid not only for a chosen set of particles and corresponding craters but also for the majority of such pairs from Fig. 89.32 and all particle/crater pairs from Figs. 89.33(b) and 89.33(c). One must also keep in mind that the energy balance considerations, presented above, are simplified. It implies that all of the energy absorbed inside the particle is used to form a crater. It does not take into account the heating of the volume surrounding the crater and particle, as well as radiative losses. The former contribution can be quite significant since the temperatures in the immediate particle vicinity are much higher than at the sample surface.

These additional dissipation channels cause the energy deficit between E_{abs} and E_{cr} to widen, confirming earlier[5] findings that *absorption initiated in the gold nanoparticle spreads out to the surrounding matrix during the laser pulse*. The conversion of the transparent matrix into an absorptive medium involves energy transfer from the particle heated to a high (up to ~10^4 K) temperature.[10] The possible channels include ionization by thermal UV radiation,[10] electron injection through thermionic emission, and thermal ionization via

conductive heat transfer.[11] The modeling of absorbing volume (plasma ball) growth by Feit *at al.*[12] pointed to exponential behavior of this process as a function of laser fluence.

3. Nanoparticle Size/Damage-Crater-Depth Correlations

The next question to be addressed is how damage-crater scale (depth, lateral size) correlates with particle size. Since the crater's lateral size and depth showed qualitatively similar behavior as a function of particle size, the crater depth is used here for illustration purposes. It is useful to mention here that the intuitive expectation that the crater depth should be the well-defined depth (60 nm) at which particles are lodged is not supported by the experimental results. In fact, craters with depths ranging from 10 to 160 nm are produced for 5.2-nm- and 8.4-nm-average-size particles at different laser fluences (see Figs. 89.32 and 89.33). If energy deposited in the absorbing volume is low, only partial evaporation of the material above the particle takes place and shallow craters with depths <<60 nm are formed. In the other limit, with increasing energy, the absorbing volume is also growing and craters with depths exceeding 60 nm can be formed. In the first approximation [Eq. (3)], the absorption cross section for small particles is proportional to the particle volume V_0. Accordingly, one might expect fairly strong crater-size/particle-size dependence. Experimental findings showed two distinctively different cases, represented in Figs. 89.32 and 89.33.

Table 89.II: Energy absorbed by the particle and energy required for crater formation.

Particle Size (nm)	σ_{abs} (cm^2)	F (J/cm^2)	E_{abs} (J)	Crater		
				Depth (nm)	Lateral Size* (nm)	E_{cr} (J)
4.0	2.2×10^{-14}	3.2	7.0×10^{-14}	60	47	4.0×10^{-13}
5.3	4.9×10^{-14}	4.0	2.0×10^{-13}	72	53	6.1×10^{-13}
6.3	7.1×10^{-14}	4.0	2.8×10^{-13}	86	64	1.1×10^{-12}
8.1	1.7×10^{-13}	4.0	6.8×10^{-13}	88	63	1.1×10^{-12}
9.2	2.5×10^{-13}	4.6	1.2×10^{-12}	120	83	2.5×10^{-12}
10.4	3.4×10^{-13}	4.6	1.6×10^{-12}	124	95	3.4×10^{-12}
11.8	5.2×10^{-13}	4.6	2.4×10^{-12}	130	112	4.9×10^{-12}
10.0	3.2×10^{-13}	2.3	7.4×10^{-13}	54	50	4.1×10^{-13}

*The lateral size is measured at the average level of the film surface [see Fig. 89.29(b)].

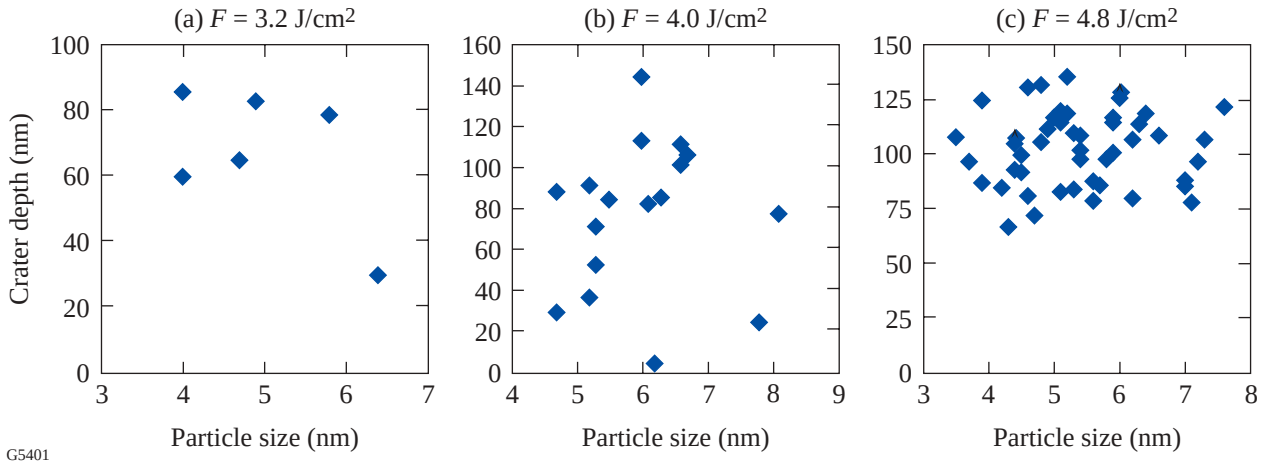

Figure 89.32
Crater depth as a function of the particle size for 5.2-nm-average-size particles and laser fluence (a) 3.2 J/cm^2, (b) 4.0 J/cm^2, and (c) 4.8 J/cm^2.

In the first case, described by laser fluences of less than 70% of the optical damage threshold, almost *no correlation* is found between particle size and crater depth [Figs. 89.32(a), 89.32(b), and 89.33(a)]. Moreover, at these low laser fluences, when a minor fraction of particles gives rise to crater formation, a situation is frequently encountered where small particles form craters but a larger particle located within a distance of ~1 μm does not. At a constant laser fluence for both particles, the strong influence of the inhomogeneous local particle environment inside the SiO_2 film becomes apparent for the laser-energy absorption process and the dissipation channels.

In agreement with a model that considers the effective growth of the absorbing volume caused by particle/matrix interaction during the laser pulse, two factors define the effectiveness of laser-energy deposition:

a. Absorption of laser-pulse energy by the particle itself. In a porous thin-film medium, the nanoparticle's physical contact with the host matrix is not perfect (Fig. 89.34), which results in the effective dielectric function ε_{eff}:

$$\varepsilon_m \geq \varepsilon_{\text{eff}} \geq \varepsilon_{\text{air}} = 1. \quad (5)$$

Taking data from the literature[6] on ε_i (351 nm) for nanoparticles with size $2R$ = 5 nm ($\varepsilon_1 = -0.8$, $\varepsilon_2 = 6.2$) and ε_m (SiO_2) = 2.19, we obtain from Eq. (3)

$$\sigma_{\text{abs}}(\text{SiO}_2)/\sigma_{\text{abs}}(\text{air}) = 2.5.$$

This result reveals the potential for significant variation in the effectiveness of damage initiation depending on the local physical environment of each gold nanoparticle.

b. Absorption by the matrix modified via energy transfer from the heated particle. Energy transfer from a particle heated to a high temperature in the early stages of the laser pulse to the surrounding film matrix is an essential part of the damage process. To achieve absorption in the particle-surrounding matrix, the energy should be transferred in a time scale of laser pulse length. Any air voids between particle and matrix (Fig. 89.34) will dramatically reduce the rate of such processes as either heat transfer by thermal conductivity or injection of electrons through thermionic emission. The same voids of the order of particle radius, due to geometrical factor, will reduce fluence of the UV radiation coming from the heated particle and consequently matrix ionization rate.

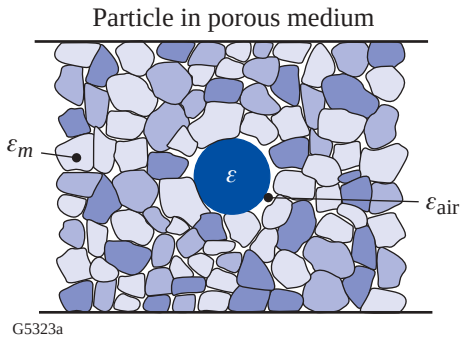

Figure 89.34
Schematic presentation of the particle embedded in the porous medium.

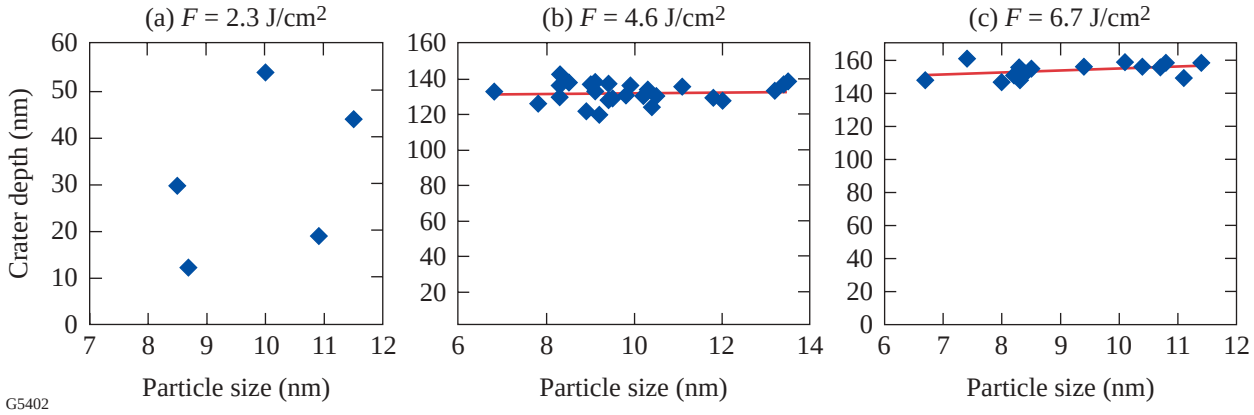

Figure 89.33
Crater depth as a function of the particle size for 8.4-nm-average-size particles and laser fluence (a) 2.3 J/cm^2, (b) 4.6 J/cm^2, and (c) 6.7 J/cm^2.

As a conclusion, effectiveness of the energy transfer from the particle to the surrounding matrix, facilitating growth of the absorbing volume and energy acquisition from the laser pulse, is a strong function of the local particle environment.

In summary, randomness in the local particle environment in the inhomogeneous thin-film medium introduces random variations in crater size and the probability of crater formation. These variations, at laser fluences below optical damage threshold, dominate particle-size effects as long as the size variation is modest, i.e., ±25%. An interesting implication from the above considerations is that porous thin films with large voids might be more damage resistant than dense films, provided that nanoscale absorbers remain the same. High UV damage thresholds of sol-gel–derived coatings,[13] characterized by large free volume, provide additional support for such a hypothesis.

The second case is characterized by very slow linear behavior of crater-depth/particle-size dependence at laser fluences *exceeding* the threshold by 20% to 70% [Figs. 89.33(b) and 89.33(c)]. At these laser-fluence conditions, all gold nanoparticles, mapped by the AFM, give rise to crater formation (100% probability), yet craters show surprisingly narrow depth distributions. Such a trend provides an indication that, with increasing pulse energy, the influence of initial conditions (local environment; particle-size variation) on the final result—crater formation—becomes less important. This can be explained by assuming that the ionized matrix in the particle vicinity starts taking on the dominant absorber role. In this case, the effective absorbing volume of the matrix should be much larger than the particle volume. The radius of this matrix volume should be several times larger than both the particle radius and the average void diameter. Such an increase in effective absorbing volume allows averaging over many local inhomogeneities, resulting in a significant reduction in random variation of the crater depth.

An example of the intermediate case for 5.2-nm particles is presented in Fig. 89.32(c), where crater-depth variation is reduced compared to the low fluence data in Figs. 89.32(a) and 89.32(b), but still significantly larger than for the above-threshold fluence data presented in Figs. 89.33(b) and 89.33(c).

To summarize results on particle/crater correlations: At laser fluences below the optical-damage threshold, effects caused by ±25% variations in particle size are obscured by strong local influence of the inhomogeneous thin-film medium on the crater-formation process. With increasing laser fluence, the probability of crater formation also increases, while the crater-depth variation is reduced due to the averaging effect caused by the larger absorption volume.

4. Crater-Formation Probability and "Nanoscale" Damage Thresholds

The possibility of detecting laser-induced morphological changes in thin film at each mapped nanoparticle location allows one to investigate the probability of crater formation for an ensemble of particles confined to a small area (typically ~6 × 6 μm), within which the laser fluence can be considered constant.

The probability of crater formation can be defined as the ratio of the number of particles giving rise to crater formation to the total number of particles within the mapped area. Taking into account that craters are detected only at particle locations, this is also the ratio of the number of craters to the total number of particles within the area. The probabilities calculated in this way for 5.2-nm- and 8.4-nm-average-diam particles are presented in Fig. 89.35 as a function of laser fluence. An extrapolation of the crater- formation probability curve to zero probability level allows one to define a laser-fluence value at which only localized melting and no vaporization of the material are observed.

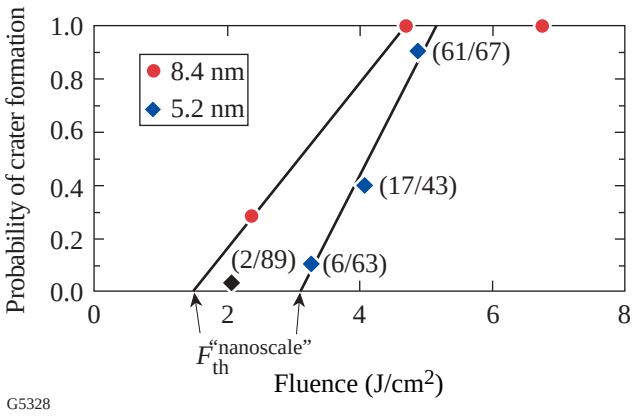

Figure 89.35
Probability of crater formation as a function of laser fluence. Numbers in brackets indicate crater/particle ratio for each mapped site. Nanoscale damage thresholds are derived from an extrapolation to zero probability.

Defined this way, *nanoscale* damage thresholds are derived as ~3.0 J/cm^2 and ~1.5 J/cm^2 for 5.2-nm and 8.4-nm particles, respectively. These are more than a factor of 2 lower than the ones obtained through optical microscopy observation. The introduction of such a threshold establishes a basis for more-meaningful comparison between theory and experiment, since

the majority of theoretical approaches consider damage onset to occur when the film material reaches the melting temperature.

Recent theoretical work by P. Grua and H. Bercegol[14] applied the Mie theory to a similar system of gold nanoparticles embedded in a glass matrix. The gold particle reaching the melting temperature was chosen as a damage criterion for calculating damage threshold. For 3.6-eV photon energy (photon energy of 351-nm radiation = 3.53 eV), 0.5-ns pulses, and particles of $2R$ = 6-nm size, the calculated damage threshold becomes ~0.4 J/cm^2. This value is much lower than ~3-J/cm^2 nanoscale threshold for 5.2-nm-average-size particles obtained in this work and associated with the matrix melting. The difference may be attributed partially to the fact that gold's melting temperature T_{Au} = 1336 K is much lower than silica's melting temperature T_{SiO_2} = 1986 K, which again points to the importance of using similar damage criteria for both theory and experiment. In the work of F. Bonneau *et al*.,[15] the simulations of nanometer-scale-inclusion–driven laser damage of fused silica indicated that damage onset occurred when the SiO_2 matrix reached the melting point. For 10-nm-diam Al nanoparticles and irradiation conditions identical to this work (351 nm, 0.5 ns), the calculated threshold was $F_{th} \sim 2$ J/cm^2. The fact that this article reports nanoscale threshold of 1.5 J/cm^2 for similar-sized, 8.4-nm gold particles unfortunately does not indicate an agreement between theory and experiment. Taking into account the difference in the absorption cross section and other relevant parameters for aluminum and gold results in a significant reduction in the calculated threshold value when substituting Al particles with Au. This points to the necessity for further theoretical and experimental investigation of the damage mechanisms.

Conclusions

- Introduction of gold nanoparticles into an SiO_2 thin film leads to a significant reduction in 351-nm damage thresholds. An extrapolation of damage threshold versus particle size curve to the intersection with undoped sample threshold allows one to estimate the size of intrinsic nanoscale absorbers (presumably Si clusters) as 1.3 to 2 nm.

- AFM mapping shows excellent correspondence between particle and crater location, indicating that absorption by gold particles is solely responsible for the damage initiation.

- Numerical estimates of energy absorbed by gold particles and energy required to melt and evaporate material within the crater volume confirm that laser-energy absorption cannot be confined inside the particle, but rather starts in the particle and then, upon temperature rise, spreads out to the surrounding matrix.

- The particle/crater correlations show peculiarities that can be explained by the influence of thin-film inhomogeneities. At laser fluences below damage threshold, the probability of crater formation and damage extent (crater depth) strongly depends on the local particle environment—effective dielectric constant, void geometry, etc. When laser fluence exceeds the optical damage threshold, the crater-depth/particle-size dependence approaches very slow linear behavior. This is explained by the dominating role of absorption by the defect-surrounding matrix, the volume of which is much larger than both the volume of the particle and characteristic film inhomogeneity.

- The observed strong influence of the thin-film structure on UV-damage initiation indicates that thin-film damage resistance can benefit from higher film porosity.

- Crater formation probability as a function of laser fluence allows one to define conditions when absorption by the particle is causing only limited melting in the surrounding matrix without significant vaporization (crater formation). A laser fluence corresponding to these conditions is introduced as a nanoscale damage threshold, which should facilitate a more-meaningful comparison with theoretical predictions using the onset of the matrix melting as a damage benchmark.

ACKNOWLEDGMENT

This work was supported by the U.S. Department of Energy Office of Inertial Confinement Fusion under Cooperative Agreement No. DE-FC03-92SF19460, the University of Rochester, and the New York State Energy Research and Development Authority. The support of DOE does not constitute an endorsement by DOE of the views expressed in this article.

REFERENCES

1. S. Papernov, A. W. Schmid, J. Anzelotti, D. Smith, and Z. R. Chrzan, in *Laser-Induced Damage in Optical Materials: 1995*, edited by H. E. Bennett *et al.* (SPIE, Bellingham, WA, 1996), Vol. 2714, pp. 384–392.

2. J. Dijon *et al.*, in *Laser-Induced Damage in Optical Materials: 1995*, edited by H. E. Bennett *et al.* (SPIE, Bellingham, WA, 1996), Vol. 2714, pp. 416–419.

3. J. Dijon, T. Poiroux, and C. Desrumaux, in *Laser-Induced Damage in Optical Materials: 1996*, edited by H. E. Bennett *et al.* (SPIE, Bellingham, WA, 1996), Vol. 2966, pp. 315–325.

4. S. Papernov and A. W. Schmid, J. Appl. Phys. **82**, 5422 (1997).

5. S. Papernov, A. W. Schmid, R. Krishnan, and L. Tsybeskov, in *Laser-Induced Damage in Optical Materials: 2000*, edited by G. J. Exarhos *et al.* (SPIE, Bellingham, WA, 2001), Vol. 4347, pp. 146–154.

6. U. Kreibig and M. Vollmer, *Optical Properties of Metal Clusters*, Springer Series in Materials Science, Vol. 25 (Springer-Verlag, Berlin, 1995).

7. K. Kohno *et al.*, Jpn. J. Appl. Phys. 1, Regul. Pap. Short Notes **33**, 6616 (1994).

8. L. Patrone *et al.*, J. Appl. Phys. **87**, 3829 (2000).

9. G. Mie, Ann. Phys. **25**, 377 (1908); C. F. Bohren and D. R. Huffman, *Absorption and Scattering of Light by Small Particles* (Wiley, New York, 1983).

10. Yu. K. Danileiko, A. A. Manenkov, and V. S. Nechitailo, Sov. J. Quantum Electron. **8**, 116 (1978).

11. L. B. Glebov, in *Laser-Induced Damage in Optical Materials: 2000*, edited by G. J. Exarhos *et al.* (SPIE, Bellingham, WA, 2001), Vol. 4347, pp. 343–358.

12. M. D. Feit *et al.*, in *Laser-Induced Damage in Optical Materials: 1997*, edited by G. J. Exarhos *et al.* (SPIE, Bellingham, WA, 1998), Vol. 3244, pp. 350–355.

13. H. A. McInnes *et al.*, in *Laser-Induced Damage in Optical Materials: 2000*, edited by G. J. Exarhos *et al.* (SPIE, Bellingham, WA, 2001), Vol. 4347, pp. 118–126.

14. P. Grua and H. Bercegol, in *Laser-Induced Damage in Optical Materials: 2000*, edited by G. J. Exarhos *et al.* (SPIE, Bellingham, WA, 2001), Vol. 4347, pp. 579–587.

15. F. Bonneau *et al.*, in *Laser-Induced Damage in Optical Materials: 2000*, edited by G. J. Exarhos *et al.* (SPIE, Bellingham, WA, 2001), Vol. 4347, pp. 308–315.

Resistive Switching Dynamics in Current-Biased Y-Ba-Cu-O Microbridges Excited by Nanosecond Electrical Pulses

The response of a superconductor to the injection of current pulses depends directly on the quasiparticle dynamics[1] since the carriers injected from the external circuit are normal (unpaired) electrons that disturb the quasiparticle–Cooper-pair dynamical equilibrium. Most commonly, a current pulse with an amplitude higher than the sample critical current I_c is used (supercritical perturbation), leading to a collapse of the superconducting state and resulting in the resistive response. This phenomenon was first investigated in metallic superconducting thin films by Pals and Wolter[2] and has been recently observed by Jelila *et al.*[3] in superconducting $YBa_2Cu_3O_{7-x}$ (YBCO) microbridges. In both cases, a resistive (voltage) response induced by the supercritical current was reported to have a certain time delay t_d, defined as the delay between the arrival of the input current pulse and the appearance of the voltage signal. The t_d was directly related to t_Δ, the time required to achieve collapse of the superconductor order parameter Δ. Jelila *et al.*[3] successfully interpreted the t_d dependence on the supercritical pulse magnitude, using the theory developed by Tinkham.[1]

The supercritical perturbation in a superconducting bridge can also be achieved by a suitable combination of the excitation-pulse magnitude I_{pulse} and the bias current level I_{dc}. In fact, a two-dimensional space of the supercritical perturbations exists, limited only by the conditions $I_{total} = I_{pulse} + I_{dc} > I_c$ and $I_{dc} < I_c$. Together, the bias current (dc) and the pulsed current (time dependent) represent simultaneous injection of *both* Cooper pairs and quasiparticles into a superconductor, allowing us to study a full range of the quasiparticle–Cooper-pair dynamics from very weak [($I_{pulse} \gtrsim I_c$ and $I_{dc} \neq 0$) or ($I_{pulse} \neq 0$ and $I_{dc} \lesssim I_c$)] to very strong ($I_{pulse} >> I_c$ and $I_{dc} > 0$) perturbations.

The aim of this work is to present our studies on superconducting-to-resistive switching of dc-biased epitaxial YBCO microbridges, subjected to nanosecond electrical pulses in the supercritical perturbation regime. Our studies confirm the existence of a substantial t_d, which depends in a complicated way on both the magnitude of $I_{pulse}(t)$ and the value of I_{dc} biasing the microbridge. Our measurements were interpreted using a modified Geier and Schön (GS) theory,[4] which, contrary to the Tinkham model,[1] allowed for the incorporation of the dc bias of a superconductor and its relation with t_d. We have also demonstrated that for perturbations much longer than the electron–phonon time t_{e-ph}, the dynamics of the current-induced resistive state is limited by the bolometric process and t_Δ reduces to the phonon escape time t_{es}.

When a long strip of a superconductor is subjected to supercritical perturbation, injected quasiparticles destroy the system equilibrium, resulting in the formation of phase-slip centers, which, in turn, lead to the collapse of Δ in a characteristic time t_Δ and the development of a resistive hot spot across the strip's weakest link. At the early, nonequilibrium, or "hot-electron," stage, the quasi-particle relaxation dynamics is governed by inelastic electron–phonon scattering, while the later resistive hot-spot-formation stage is a bolometric process. Thus, t_Δ should initially follow t_{e-ph} and later be limited by t_{es}. The nonequilibrium process is, of course, measurable only if the width of $I_{pulse}(t)$ is of the order of t_{e-ph} or shorter. The t_d, which determines the appearance of a macroscopic resistive state, is related not only to t_Δ but also to the sample reduced temperature T/T_c and to the magnitudes of both I_{pulse} and I_{dc} with respect to I_c.

Even though the earlier YBCO experiments by Jelila *et al.*[3] were successfully interpreted using the Tinkham theory,[1] we choose to use the GS theory[4] since it is the only approach that incorporates the dynamics of both Cooper pairs and quasiparticles. The GS model allows the study of the supercurrent-induced response in both the hot-electron and bolometric regimes. It considers a one-dimensional homogeneous superconducting microbridge in which Cooper pairs coexist with quasiparticles. The Cooper-pair dynamics is described by the time-dependent Ginzburg–Landau equation,[5] while the quasiparticle distribution is given by the Boltzmann equation.[6] The main feature in the GS theory is the equation for the conservation of current between the superfluid (Cooper pair) and normal fractions of electrons, and it allowed us to introduce, in

a natural way, the bias I_{dc} in addition to the quasiparticle perturbation $I_{pulse}(t)$. In our approach to the GS model,[7] the three aforementioned differential equations are first solved for a constant subcritical current (the dc bias), resulting in equilibrium values for the parameters of the system at a time >> t_{es}. Next, those equilibrium parameters are used as initial conditions to solve the GS equations for I_{total} constituted of the same I_{dc} and a varying transient $I_{pulse}(t)$. The t_d is defined as the time needed by the normal current component to rise to 50% of the total current through the bridge.

Figure 89.36 presents our GS model simulations of t_d dependence on the reduced bias current $i_{dc} = I_{dc}/I_c$ and on the reduced current pulse $i_{pulse} = I_{pulse}/I_c$. The t_d dependence on the supercritical perturbation forms a surface, which exponentially diverges to infinity at the $i_{dc} + i_{pulse} = 1$ boundary and very rapidly drops toward zero at $i_{dc} = 1$. This behavior is expected. In the $i_{dc} + i_{pulse} < 1$ range, the perturbation is subcritical and the bridge always remains in the superconductive state (only the kinetic-inductive response is possible), while for $i_{dc} > 1$, the bridge remains in the resistive state irrespective of the value of the i_{pulse} perturbation. What is unexpected is the nonlinear $t_d(i_{dc})$ dependence for a constant i_{pulse}. From our solution of the GS model, shown in Fig. 89.36, it is obvious that i_{dc} is not just a scaling parameter in the $i_{pulse} > 1 - i_{dc}$ switching criterion. The magnitude of the bridge bias plays the critical role in the switching dynamics not only for $i_{pulse} < 1$ but also for supercritical i_{pulse}'s, as i_{dc} approaches 1. Finally, we mention that the white lines, shown on the t_d surface in Fig. 89.36, correspond to our experiments and will be discussed below.

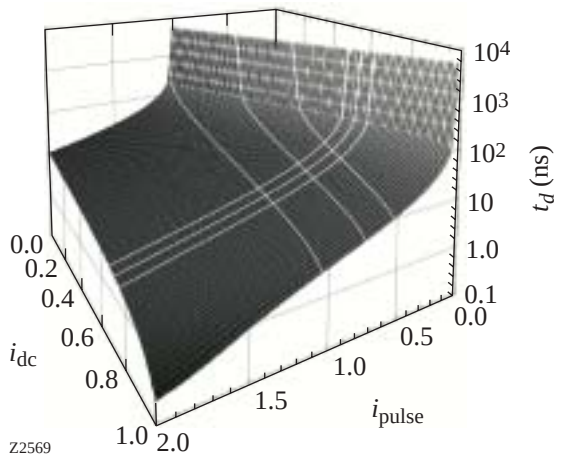

Figure 89.36
The time delay t_d surface as a function of both the reduced bias current i_{dc} and the reduced current pulse i_{pulse}. The t_d dependence on the supercritical perturbation was calculated using a modified GS theory for the parameters (T/T_c = 0.96 and t_D = 17 ns) directly corresponding to our experimental conditions (white lines).

Our experimental samples consisted of 200-nm-thick epitaxial YBCO films deposited on MgO substrates and patterned into 8-mm-long, 150-μm-wide coplanar strips (CPS's) with a single 25-μm-wide by 50-μm-long microbridge, placed across the CPS. The bridges were characterized by a zero-resistance transition temperature T_{c0} = 82.5 K and a critical current density $J_c > 1$ MA/cm^2 at 77 K. For experiments, the samples were mounted on a copper cold finger inside a temperature-controlled nitrogen cryostat. Nanosecond-wide electrical pulses from a commercial current-pulse generator were delivered to the bridge via a high-speed, semirigid coaxial cable wire-bonded directly to the test structure. The dc bias was provided from an independent source and combined with the current pulse through a broadband microwave bias-tee. A 14-GHz-bandwidth sampling oscilloscope was used to monitor the microbridge response. The oscilloscope was connected to the sample via a second semirigid cable wire-bonded to the output contact pads of the CPS.

Figure 89.37 shows a series of waveforms of the time-resolved resistive switching dynamics of our YBCO microbridge subjected to a 20-ns, 130-mA current pulse at different I_{dc} levels. Since the I_c of the microbridge was 125 mA, the I_{pulse} itself was supercritical, which, when superimposed on the dc bias, resulted in I_{total} well above I_c. From the bottom waveform with no biasing to the second waveform from the top with $I_{dc} = 0.76\, I_c$, the resistive response is seen as the onset and growth of the plateau region after the initial kinetic-inductive peak. The time evolution of the voltage response starts with the small inductive peak, as the still-superconducting microbridge appears as an inductive element and differentiates the ~0.5-ns-wide rising edge of the input current pulse.[7] Later, since I_{total} is supercritical, the superconducting state starts to collapse, as discussed earlier, giving rise to the resistive response after the delay time t_d. The top (thick line) waveform in Fig. 89.37 corresponds to $I_{dc} > I_c$ or, alternatively stated, to the YBCO microbridge in the normal state. We note that in this case, the measured output pulse is just the input current pulse, slightly distorted due to resistive loss of the YBCO CPS. A voltage due to the flux-creep effect can be observed before the inductive peak, as the small offset of the waveform, when I_{dc} increases toward I_c. A similar plateau can also be isolated between the inductive and resistive responses, when $t_d > 20$ ns. Plotting the I_{dc}-V curve in both cases permitted us to identify a shift

corresponding to I_{pulse} and, therefore, allowed us to compute the actual amplitude of the input pulse across the microbridge.

From a series of data sets analogous to Fig. 89.37, but collected under different experimental conditions, we extracted the t_d values as the time delay between the onset of the inductive peak (instantaneous with the arrival of the input pulse) and the half-point of the rising edge of the resistive region of the voltage response. Our experimental t_d values along with the GS theory are shown in Fig. 89.38. Figure 89.38(a) presents t_d as a function of i_{dc}, for three different values of i_{pulse} = 0.53, 0.74, and 1.04, while Fig. 89.38(b) shows t_d as a function of i_{pulse}, for i_{dc} = 0.68, 0.72, and 0.76, respectively. The GS simulated curves in Fig. 89.38 are the same as the white lines outlined on the t_d surface in Fig. 89.36. The selected levels of supercritical perturbations were $I_{total}/I_c > 1.2$, corresponding to the excitation range where the GS, Tinkham, and Pals and Wolter theories start to disagree.[7] We note that the t_d data points agree very well with the GS theory. The best fit to all our experimental data was obtained for t_D = 17 ns. This latter value is exactly the same as the t_{es} for our YBCO-on-MgO films,[8] calculated as $t_{es} = (4d)/(Kn)$ = 17 ns, where d = 200 nm is the YBCO film thickness, K = 0.020 is the average phonon transparency of the YBCO/MgO interface,[9] and n = 2.8 km/s is the velocity of sound in YBCO averaged over the three acoustic modes. Thus, we can conclude that for current excitations that are much longer than t_{e-ph}, the resistive transition in YBCO films is governed by the bolometric (equilibrium) process and its time-resolved dynamics is limited by t_{es}. This latter observation agrees very well with both theoretical[9] and experimental[10] studies of the response of YBCO films exposed to optical perturbations. It is also consistent with earlier pulse perturba-

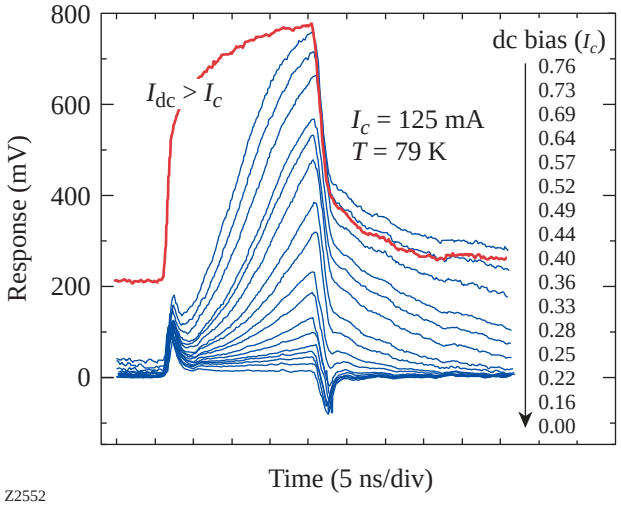

Figure 89.37
Time-resolved YBCO microbridge response to a 20-ns, 130-mA current pulse for the various bridge bias levels at 79 K. T_{c0} = 82.5 K; I_c = 125 mA. For the top (bold) waveform, the bridge was in the normal state ($I_{dc} > I_c$); note the large voltage offset that is representative of the resistive state of the bridge.

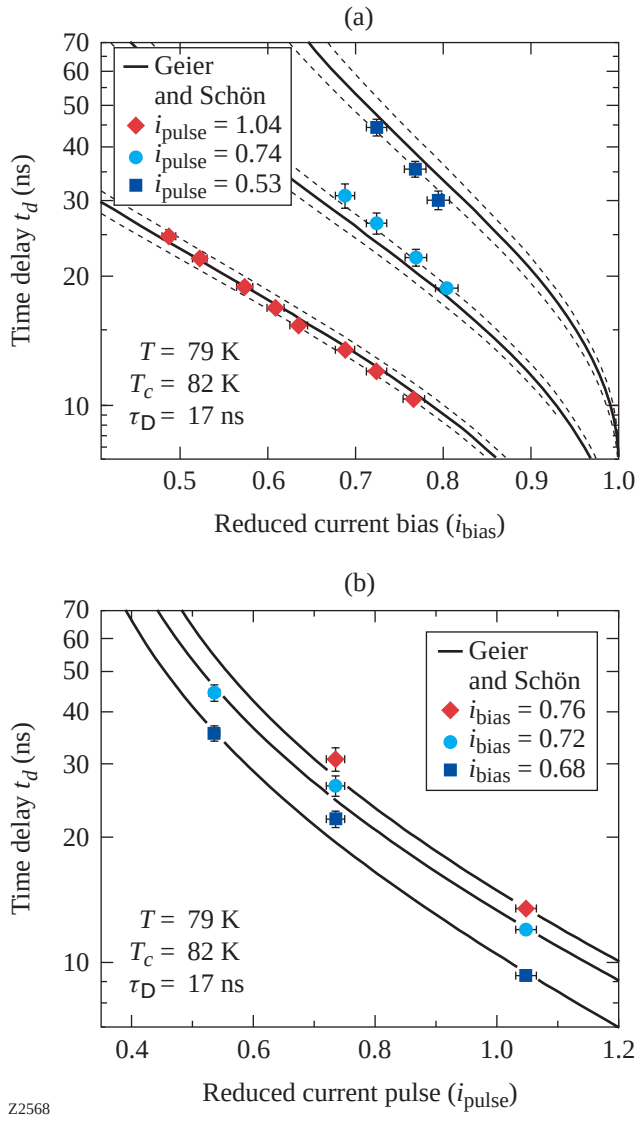

Figure 89.38
The measured t_d as a function of (a) the reduced bias current i_{dc} and (b) the reduced current pulse i_{pulse}. The solid lines represent the GS theory and correspond to the white lines in Fig. 89.36. The dashed lines in (a) define the error range in the amplitude of the current pulse applied the bridge. Note that the t_d scales are logarithmic.

tion experiments, since the literature data[11] seem to show that t_D is proportional to the film thickness and its value is consistent with the experimental determination of t_{es} for YBCO deposited on MgO, which is t_{es} = 0.085 ns/nm.

In conclusion, we have presented a study of dc-biased YBCO microbridges excited by nanosecond-long current pulses, which led to supercritical perturbations and resulted in resistive switching, occurring after a certain delay time t_d. The t_d depends roughly exponentially on both the amplitude of the current pulse and the film dc bias current, in a manner consistent with the GS theory. The duration of the superconducting-to-resistive response is, in our case, governed by the equilibrium dynamics of quasiparticles in the film and is limited by t_{es}, with no need to introduce the special t_D relaxation time. We can also predict that t_d could be shortened by using either thinner YBCO films or better acoustically matched substrates. The resistive response of YBCO bridges exposed to picosecond-long perturbations should be limited by the nonequilibrium $t_{e–ph}$ interaction time.

ACKNOWLEDGMENT

This work was supported by the NSF grant DMR-0073366. Additional funding was provided by the TeraComm Research Inc. The author wishes to thank Prof. Boris Shapiro from the Bar Ilan University for fruitful discussions and acknowledge the grant 2000164 from the US-Israel Binational Science Foundation, Jerusalem, Israel.

REFERENCES

1. M. Tinkham, in *Nonequilibrium Superconductivity, Phonons, and Kapitza Boundaries*, edited by K. E. Gray (Plenum Press, New York, 1981), Chap. 8, pp. 231–262.
2. J. A. Pals and J. Wolter, Phys. Lett. A **70A**, 150 (1979).
3. F. S. Jelila *et al.*, Phys. Rev. Lett. **81**, 1933 (1998).
4. A. Geier and G. Schon, J. Low Temp. Phys. **46**, 151 (1982).
5. See, e.g., M. Tinkham, *Introduction to Superconductivity*, 2nd ed., International Series in Pure and Applied Physics (McGraw-Hill, New York, 1996).
6. A. Schmid and G. Schon, J. Low Temp. Phys. **20**, 207 (1975).
7. G. J. A. Sabouret, "Time Response of High-Temperature Superconducting Microbridge Structures Perturbed by Ultrafast Electrical Current Pulses," M.S. thesis, University of Rochester, 2001.
8. A. V. Sergeev and M. Yu. Reizer, Int. J. Mod. Phys. B **10**, 635 (1996).
9. J.-P. Maneval, K. P. Hong, and F. Chibane, Physica C **235–240**, 3389 (1994).
10. A. D. Semenov, G. N. Gol'tsman, and R. Sobolewski, Supercond. Sci. Technol. **15**, R1 (2002).
11. I. Harrabi, F. Ladan, and J.-P. Maneval, Int. J. Mod. Phys. B **13**, 3516 (1999).

Properties of Amorphous Carbon Films

Introduction

The properties of hydrogenated amorphous carbon (a-C:H) films have been studied over the past decade. A broad spectrum of applications ranging from carbon-based semiconductors, to wear-resistant coatings, to corrosion-resistant surfaces, to coatings on microspheres for inertial confinement targets has been identified. Plasma-based deposition systems use several approaches to decompose the feed gas and grow the carbon films: radio frequencies,[1] direct currents,[2] hot filaments,[3] glow discharges, and saddle fields.[4] In saddle-field plasmas, electrons oscillate between two electrodes to ionize the feed gas. Ions are drawn from the plasma by a gentle axial field and are delivered to a substrate beyond the transparent electrodes. Ions, radicals, and neutrals participate in the film growth process.

The underlying strength of the saddle-field plasma configuration rests in the ability to control several plasma parameters independently over a broad range of operating conditions and to deposit films outside the plasma region. The ion flux and energy, the ratio of the charged particles to neutral particles leaving the plasma, the temperature of the substrate, and the chemical species being deposited on the substrate can be tailored to optimize film properties for specific applications. Adjusting these parameters can alter the film density, the hydrogen content, the intrinsic stress within the films, the porosity, and the surface morphology.

To understand how deposition conditions influence the film properties—stress, density, and growth rate—a series of thin films were grown on flat glass and Pyrex™ plates. The correlation between film stress and deposition condition was measured by coating 0.1-mm-thick glass substrates with a-C:H and measuring the resultant curvature of the bilayer. Density and growth rate were measured by depositing films on thick Pyrex™ plates that were masked with stainless steel covers with an 18.9-mm-diam hole near the center. Subsequently, films were grown on polyalpha-methylstyrene (P*a*MS) and glow discharge polymer (GDP) microspheres using the conditions established for flat plates. One motivation for this work was to establish a protocol for coating microspheres with thick, smooth, high-density hydrogenated amorphous carbon films for the inertial confinement energy program as a precursor to growing tritiated films. This paper summarizes the film properties that were obtained and discusses their dependence on deposition conditions.

Film Properties

The deposition chamber used in this work is a right cylinder. Stainless steel was the construction material of choice. A transparent anode grid divides the deposition chamber in half. Transparent grid cathodes are located 15 cm from the anode at either end of the cylinder. Electrically floated end plates are positioned approximately 7 cm beyond the cathodes. The grid open area is approximately 80%. Substrates to be coated are fixed to the end plates.

Each substrate was cleaned and degreased in an ultrasonic bath using trichloroethylene, acetone, and methanol in sequence. The substrates were then rinsed with de-ionized water, dried, and fixed on the end plate. All depositions were carried out at or near room temperature. Internal components in the vacuum chamber were inspected, removed, and cleaned before each run. Immediately following a deposition, the film thickness and the radius of curvature of the coated thin substrate were measured using a profilometer. The surface morphology was examined under an optical microscope. The films were subsequently stored in air for more detailed examination. Surfaces were inspected daily under the optical microscope for changes. The structure of the film was examined by breaking the coated substrates to view its cross section under a high-resolution scanning electron microscope (SEM). Thickness was measured using both profilometry and SEM. Film density was estimated from profilometry and SEM data.

Surface Condition

The surface smoothness of films bonded to Pyrex™ substrates depended on the deposition conditions but did not change with time once the deposition was completed. In general, particulate deposition increased with increasing methane pressure. The roughest films were produced at 27 Pa, the

smoothest at 1.3 Pa. Film smoothness could be further enhanced with hydrogen dilution of the methane plasma.

Films deposited on P*a*MS microspheres tended to detach from the underlying structure over the course of several days. Figure 89.39 illustrates typical ridges that evolved and stabilized on a P*a*MS shell over 28 days. No deposition conditions for pure methane plasmas could be found to increase the film–substrate bonding to the level that prevented film detachment on P*a*MS shells. Detachment, however, was never observed on GDP microspheres or Pyrex™ substrates even in pure methane plasmas.

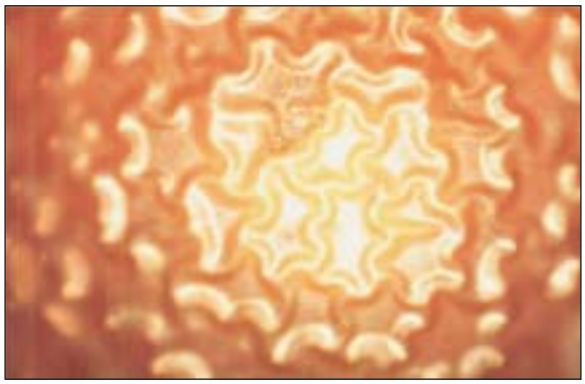

E11444

Figure 89.39
Surface morphology on a P*a*MS microsphere 28 days after deposition; methane pressure: 5.3 Pa, flow rate: 3.5 sccm, anode current: 30 mA, floated substrate.

Film Cross Sections

A typical film cross section using SEM is provided in Fig. 89.40. The film, on the right-hand side of the picture, is intimately bonded to the Pyrex™ substrate. The body of the film is devoid of any microstructure, even at SEM resolutions on the 10-nm scale; these films are amorphous. As the deposition proceeds, the film grows with the agglomeration of matter on the surface coalescing into the uniformly dense and featureless layer seen in this figure. Several types of particles are involved in the growth process: fragmented methane comprising neutrals and radicals with varying CH atom ratios, including C and H atoms; more-complex CH chains that have polymerized in the plasma; and solid particles that have dislodged from chamber surfaces and attached to the film surface. The relative contributions of these components condensing on the surface to the film growth dynamics depend more on hydrogen dilution of the methane plasma than on the operating methane pressure. Films grown in pure methane plasmas exhibit surface roughness and porosity that are unacceptable for microsphere applications. Surface smoothness improves, however, when the methane is diluted with hydrogen, and increasing dilution increases surface smoothness.

Hydrogen dilution has additional effects. Plasma stability improves with dilution. There is a notable lack of carbonaceous deposition on the grids and chamber walls. Undiluted methane plasmas are responsible for particulate agglomeration in the gas phase and particle production that eventually find their way to the film surface.

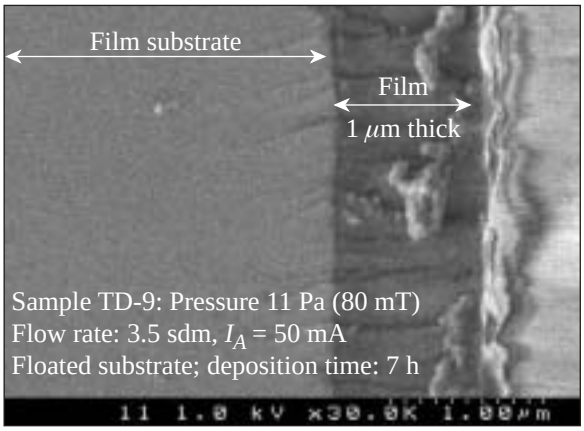

E11373

Figure 89.40
Typical film cross section using SEM; methane pressure: 11 Pa, flow rate: 3.5 sccm, anode current: 50 mA, floated substrate.

Internal Stress

The relative intrinsic stress within the films can be estimated from the radius of curvature of the coated thin wafers.[5,6] The larger the curvature of radius, the lower the relative intrinsic film stress. The relative stress dependence on fill pressure and methane concentration for several films is provided in Figs. 89.41 and 89.42, respectively. All data have been scaled to a uniform film thickness of 1 *m*m for this comparison.

Figure 89.41 indicates that roughly doubling the deposition gas pressure from 2.7 Pa to 5.3 Pa reduces the relative stress approximately fivefold. At an operating pressure of 25 Pa, film stress approaches zero. At the higher operating pressures, plasma particles impinging on the film surface have lower impact energies. They are less likely to embed into the film

bulk. Under these conditions, films grow by particle condensation on the surface rather than by implantation into the bulk. These films can readjust during the growth process to reduce internal stress.

Figure 89.42 illustrates that stress in films increases as the fraction of hydrogen in H_2/CH_4 plasmas decreases and exceeds values for films grown in undiluted methane plasmas. The transition to lower stress values in pure methane plasmas most likely reflects the difference in the plasma composition between diluted and undiluted plasmas.

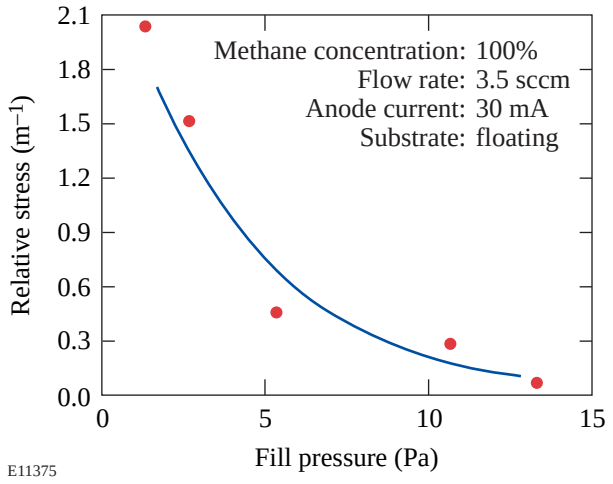

Figure 89.41
Stress in hydrogenated films decreases with increasing methane pressure.

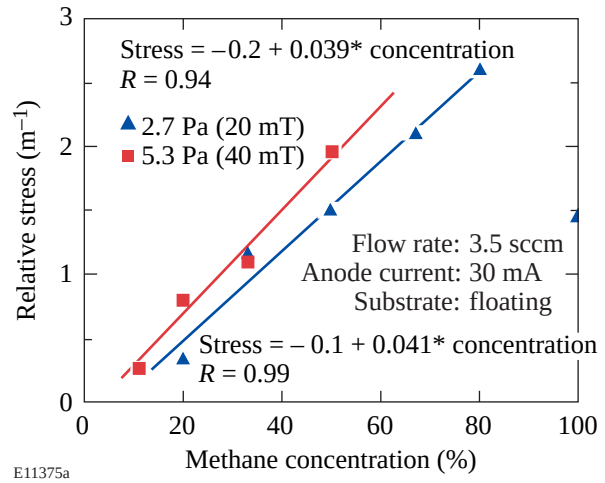

Figure 89.42
Stress in hydrogenated films increases with decreasing dilution of the methane plasma.

Thickness and Density

Densities are derived from the thickness of the film deposited on the substrate through a stainless steel mask and the film weight determined by weighing each substrate before and after deposition. Film thickness has been measured using both profilometry and SEM. A variation in the film thickness across the diameter of the mask resulting from a shadowing effect by the mask has been included in the density calculation. The film thickness along the border of the mask is smaller than in the center of the opening. Thickness and density estimates based on SEM data are considered to be more reliable and consequently used throughout this discussion.

Figure 89.43 illustrates that film density is strongly dependent on pressure, decreasing with increasing neutral pressure. At lower neutral pressures the electron temperature in the plasma is higher. Higher-energy electrons decompose a larger proportion of the feed gas into smaller neutrals, radicals, and ions. When these particles condense on the substrate, they tend to form higher-density, diamond-like films rather than lower-density, polymeric-like films.

Figure 89.44 demonstrates that film density is also weakly dependent on methane concentration in the plasma, in general increasing with decreasing hydrogen dilution. Increasing the methane concentration in the plasma for a fixed neutral pressure increases the carbon flux to the substrate relative to the hydrogen flux and leads to higher-density films. At 20%

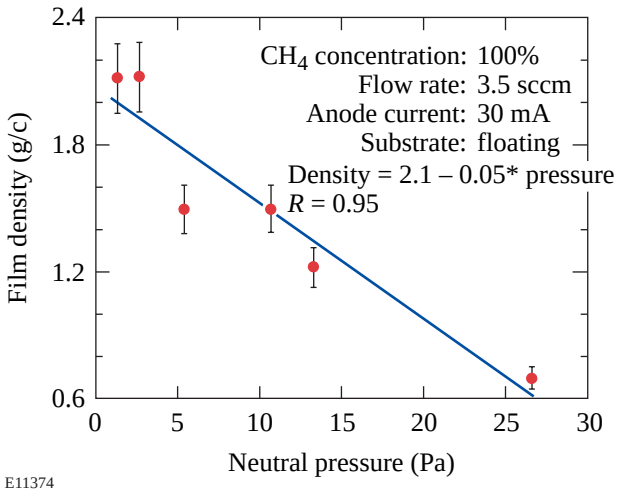

Figure 89.43
Hydrogenated film density decreases with increasing methane pressure in the deposition chamber.

methane, the atom C/H ratio is 8%; at 80% that ratio increases to 22%. The plasma is predominantly a hydrogen plasma with an increasing minority constituent as the methane concentration increases. It is noteworthy that up to 80% methane concentration, film densities for both neutral pressures are similar, suggesting that the plasma properties are similar for the two cases. At 100% the C/H ratio is 25%; however, the lower operating pressure, 2.7 Pa, yields a film with a significantly higher density than for the 5.3-Pa case, suggesting that the plasma properties for that case are very different.

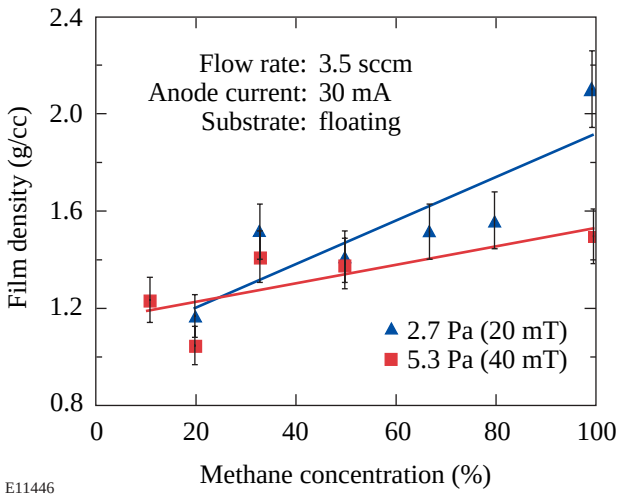

Figure 89.44
Film's density's dependence on hydrogen dilution of the methane.

Growth Rate

Growth rate depends on the operating pressure, as illustrated in Fig. 89.45. It peaks near 5 Pa and decreases at both lower pressures and higher fill pressures. At pressures below 5 Pa, the number of carbon atoms present in the plasma limits the film's growth rate. The extraction rate is fixed by the electric field within the plasma sheath, so the film can grow only at the rate that carbon species enter the sheath from the plasma side. The carbon particle density is determined by the fill pressure. Increasing the fill pressure increases the number of carbon species available for film growth, as the figure illustrates. At pressures above 5 Pa the growth rate is reduced because the extraction field strength is reduced at the higher fill pressures. While the carbon species density in the plasma is high, most of these particles are not available for film growth. The peak near 5 Pa represents the optimum balance between available carbon species in the plasma and their extraction rate for this system.

Figure 89.46 illustrates the film's growth rate dependence on methane concentration at a fixed neutral pressure. Fixing neutral pressure fixes the extraction field. Increasing the carbon species number density within the plasma by increasing the methane concentration also increases the number of particles available for extraction. The extraction rate and consequently the growth rates are seen to increase with methane concentration in this figure as expected.

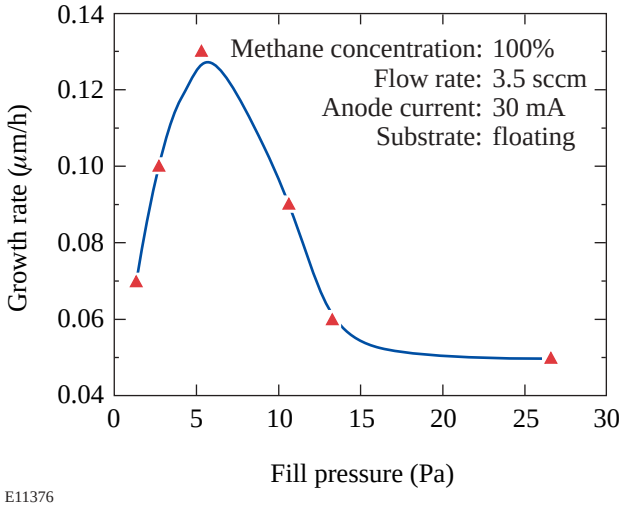

Figure 89.45
Growth rate dependence on neutral pressure.

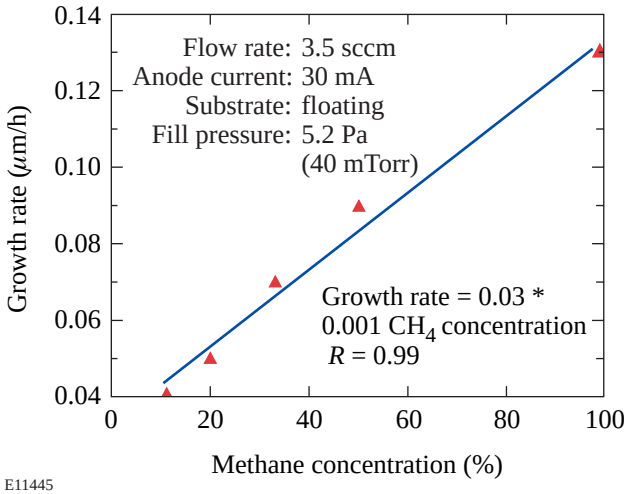

Figure 89.46
Growth rate increases with increasing methane content in the plasma.

Conclusions

The surface morphology of films depends on the operating gas pressure and the hydrogen concentration in the gas mixture. Surface smoothness improves with decreasing gas pressure and increasing hydrogen dilution. Gross features on the surfaces, such as lumps and pits, are attributed to particulate transport from the plasma to the film surface. Film chips detached from the chamber walls are the most likely source of these particles. The presence of hydrogen reduces the production or existence of larger-chained molecules in the plasma. Consequently the deposition of these particles on the films, the grids, and the walls is strongly suppressed. Fine structure on the film surface is attributed to the deposition conditions—the energy of the impacting particles, the ratio of the atom/neutral/radical fluxes, and the magnitude of the carbon flux—and is most likely related to gas phase polymerization within the plasma.

Hydrogen dilution also improves plasma performance. Long-term plasma stability improves because the grids are not progressively coated with carbonaceous material.

The key deposition parameter responsible for residual stress in the film is the pressure of the precursor gas. Decreasing the pressure from 27 Pa to 1.3 Pa increases the residual stress in the films. Increasing the pressure of the precursor gas decreases the anode potential and increases the substrate self-bias, thereby changing the energy distribution of the particle flux involved in the deposition process.

Deposition of films on PaMS microspheres showed that stress generated during the growing process can drastically change the topology of the coated surface over time. In some cases changes began within a few hours of deposition, while in other cases the films were unaltered for several weeks. In addition to these time-dependent manifestations, all films exhibited a granular surface.

Operating pressure also plays an important role in modulating density and growth rate. Film density depends on the gas pressure. Film density increases with decreasing gas pressure to reach a maximum of 2 g/cc at 2.7 Pa in methane plasmas. Diluting the methane with hydrogen decreases the film density.

Growth rates up to 0.13 μm/h have been achieved. These tests provide the deposition conditions for growing tritiated amorphous carbon films.

ACKNOWLEDGMENT

This work was sponsored by the University of California under contract #UC/LLNL-B507012 and by Materials and Manufacturing Ontario.

REFERENCES

1. S. R. P. Silva *et al.*, Diam. Relat. Mater. **4**, 977 (1995).
2. D. S. Whitmell and R. Williamson, Thin Solid Films **35**, 255 (1976).
3. E. N. Farabaugh *et al.*, in *Applications of Diamond Films and Related Materials: Third International Conference*, edited by A. Feldman *et al.* (NIST, Gaithersburg, MD, 1995), Vol. 1, pp. 361–364.
4. F. Gaspari *et al.*, in *Applications of Diamond Films and Related Materials: Third International Conference*, edited by A. Feldman *et al.* (NIST, Gaithersburg, MD, 1995), Vol. 1, pp. 743–746.
5. J. G. Kim and J. Yu, J. Mater. Res. **13**, 3027 (1998).
6. H. Yamada, O. Tsuji, and P. Wood, Thin Solid Films **270**, 220 (1995).